Local reactivity of bimetallic overlayer and cluster systems

Ataollah Roudgar

Technische Universität München
Physik-Department T30
Univ.-Prof. Dr. A. Groß

Local reactivity of bimetallic overlayer and cluster systems

Ataollah Roudgar

Vollständiger Abdruck der von der Fakultät für Physik der Technischen Universität München zur Erlangung des akademischen Grades eines

Doktors der Naturwissenschaften (Dr. rer. nat.)

genehmigten Dissertation.

Vorsitzender:		Univ.-Prof. Dr. U. Stimming
Prüfer der Dissertation:	1.	Univ.-Prof. Dr. A. Groß
	2.	Univ.-Prof. Dr. M. Kleber

Die Dissertation wurde am 29. März 2004 bei der Technischen Universität München eingereicht und durch die Fakultät für Physik am 8. April 2004 angenommen.

Abstract

The adsorption of atomic hydrogen and molecular CO on Pd and Cu overlayers on Au in the presence and absence of water and also Pd clusters supported on the substrates is studied using density functional theory. First it is demonstrated that both surface strain and substrate interaction effects contribute to the modification of the reactivity of the overlayer system. We found a maximum of the binding energies of both H and CO on two Pd overlayers on Au(111) and Au(100). The second part of this thesis is concerned with the adsorption on small Pd clusters supported by Au(111). The adsorption energies on Pd clusters turn out to be less than on corresponding Pd/Au overlayer which is a consequence of the reduced atomic distances in the cluster and the cluster-support interaction. The H and CO adsorption energies on the Pd/Au(111) overlayer in the presence of water are modified by less than 10% by the most stable H_2O bilayer compared to the clean surface. This indicates that theoretical adsorption studies at the solid-vacuum interface might also be relevant for the solid-liquid interface.

Zusammenfassung

Mittels Dichtefunktionaltheorie wird die Adsorption von atomarem H und molekularem CO an dünnen Pd- und Cu-Schichten und Pd-Clustern auf einem Goldsubstrat untersucht. Ebenso wird der Einfluss von Wasser auf die Adsorptionsenergien betrachtet. Sowohl die berflächenverspannung als auch die Substratwechselwirkungseffekte tregen zur Änderung der Reaktivität des Schichtsystems bei. Die Bindungsenergien von H und CO ist maximal für zwei Pd-Schichten auf Au(111) und Au(100). Bei der Adsorption an kleinen Pd-Clustern auf Au(111) stellt sich heraus, da die Adsorptionsenergien geringer sind als auf der entsprechenden Pd/Au-Schicht als Folge verringerter Atomabstnde im Cluster und der Wechselwirkung mit dem Substrat. Die H- und CO-Adsorptionsenergien auf der Pd/Au(111)-Schicht ndern sich um weniger als 10% in Anwesenheit von Wasser. Das weist darauf hin, daß theoretische Studien zur Adsorption an der Festkörper-Vakuum Grenzfläche auch für die fest-flüssig Grenzfläche von Bedeutung sein können

Acknowledgments

First and most importantly, it is a pleasure to thank my supervisor, Prof. Dr. Axel Groß, for offering me the opportunity to work on this interesting and exciting topic and do a doctoral thesis in his group. I am grateful for his support and the chance to present and discuss my results with him and at the number of conferences.

I would also like to thank my colleagues of the T30g group, Markus Lischka and Christian Mosch for answering me a lot of questions regarding the code and running simulations on various platforms. I would also like to thank Christian Bach, Prof. Dr. Wilhelm Brenig, Arezoo Dianat, Sung Sakong for all the interesting discussions we had together. I owe a considerable debt to my ex-colleges from Max-Planck-Institute in Stuttgart, Ari Seitsonen and Daniel Aktah for the helpful discussions. Without Ari I would hardly have managed to get to know such a nice group in Munich. Moreover, I wish to thank Georg Kresse, the main author of VASP, for the assistance with his enormous piece of software.

Part of the computational work was done on the high performance computing facilities of the Leibniz-Rechenzentrum within the t2101 project, and I am indebted to their administrative team for providing such an excellent computational working environment and support. Furthermore, I also would like to acknowledge financial support by Deutsche Forschungsgemeinschaft.

There are always people behind the scenes, whose support is nonetheless indispensable. Most of all, I am grateful for the continual encouragement of my parents, my brother and my sisters. Without naming them individually, I finally thank many friends of mine for their share in recreational activities, which rank highly among the preconditions for creative work of any kind.

München
April 2004

Ataollah Roudgar

Contents

Abstract **iii**

Zusammenfassung **v**

Acknowledgments **vii**

1 Theory **1**
- 1.1 Hamiltonian 1
- 1.2 Density Functional Theory 2
  - 1.2.1 Kohn-sham scheme 3
  - 1.2.2 Exchange correlation energy 5
  - 1.2.3 Generalized gradient approximation 5
- 1.3 Methods 7
  - 1.3.1 Super-cell and Brillouin zone 7
  - 1.3.2 Special k-points 10
  - 1.3.3 Basis set-Plane wave 13
  - 1.3.4 Pseudopotential 16
  - 1.3.5 Fractional occupation numbers 19
- 1.4 Basics concepts 23
  - 1.4.1 Adsorption energy 23
  - 1.4.2 Density of states DOS and LDOS 24
  - 1.4.3 d-band model 24
  - 1.4.4 Induced charge density 27
  - 1.4.5 Blyholder model for adsorption of CO 27

2 Adsorption on Pd overlayer deposited on noble metals **29**
- 2.1 Pd/Au: Computational method and overlayer structure 31
- 2.2 Adsorption energies on Pd/Au overlayers 33
- 2.3 Discussion 34
  - 2.3.1 Electronics structure 34
  - 2.3.2 Lattice strain effects 35
  - 2.3.3 Substrate interaction effects 38

    - 2.3.4 Coverage effects 42
  - 2.4 Pd/Cu and Cu/Pd: Computational method and overlayer structures . . 44
  - 2.5 Pseudomorphic Pd/Cu and Cu/Pd overlayers 45

3 Local reactivity of supported metal clusters: Pd_n **on Au(111) 51**
  - 3.1 Computational setup 52
  - 3.2 Pd_3 and Pd_7 planar clusters 53
  - 3.3 Three-dimensional cluster Pd_{10} 57

4 Local reactivity of a Pd/Au overlayer in the presence of water 65
  - 4.1 Computational method 68
  - 4.2 Water adsorption on Pd/Au overlayer surface 69
    - 4.2.1 Water monomer and dimmer 69
    - 4.2.2 Water adsorption energy for different water coverages 71
  - 4.3 Hydrogen and CO adsorption energies 72

5 Conclusions 77

Bibliography 79

List of Publications 89

List of Figures

1.1 replication of super-cell c along x, y and z direction. 7

1.2 replication of super-cell c along x, y and z direction. (a) The clean surface(111) with 1×1 super-cell, (b) 2×2 super-cell with 1/4 coverage of black atoms. (c) 3× 3 super-cell with coverage 1/9 of black atoms. . 10

1.3 (a) The position of k-points in reciprocal space in surface (100) with $q_1 = q_2 = 3$. (b) Due to the symmetry, all symmetrically equivalent points are shown with the same symbol. (c) The position of the irreducible k-points. 11

1.4 (a) The position of k-points in reciprocal space in surface (100) with $q_1 = q_2 = 4$. (b) All points with the same symbol are identical due to the symmetry. (c) The positions of the irreducible k-points. 12

1.5 (a) The position of k-points in reciprocal space in surface (100) with $q_1 = q_2 = 4$. (b) The symmetry between the positions. All the points with the same symbol are identical due to the symmetry. (c) The position of the irreducible k-points. 12

1.6 The construction of $\mathbf{G}$ vectors in two-dimension. $\mathbf{b}_1$ and $\mathbf{b}_2$ are the reciprocal lattice vectors and all the crossing of the line give a $\mathbf{G}$ vector. The cut-off sphere for the wave functions $\mathbf{G}_{\mathrm{cut,wf}}$ and density $\mathbf{G}_{\mathrm{cut,n}} = 2\mathbf{G}_{\mathrm{cut,wf}}$ as well as for density with dualling $\mathbf{G'}_{\mathrm{cut,n}} < 2\mathbf{G}_{\mathrm{cut,wf}}$ are shown (the latter partially, with a dash line). Please note that $\mathbf{k}$=0 was used for the cut-off sphere of the wave function. 15

1.7 An example for a pseudo potential: A pseudo potential for Pd 17

1.8 An example of a hard Hamann-Schlüter-Chiang and a soft Troullier-Martin pseudo potential for Pd. 19

1.9 An example of the all electron wave function - times radius r - (solid line), pseudo wave function of the Troullier-Martin (dash line) and a Vanderbilt ultra-soft pseudo wave function (dash-dot line) for Pd. . . . 20

1.10 (a) An example of a arbitrary function ϵ(k) (dash-dot line) which exceeded in some points the Fermi level μ. ϵ(k) $\cdot\, \Theta$ (dash line) has been then smooth out by a function f(ϵ, μ) (solid line) where f(ϵ, μ) is given by Eq. 1.68. (b) ϵ(k) $\cdot$ f(ϵ, μ) as a function of number of k-point, $\sigma = 0$ is equivalent to ϵ(k) $\cdot\, \Theta$ 21

1.11 The interaction between H_2 and a metal substrate. (a) Bonding and anti-bonding states of H_2. (b) Interaction of H_2 molecule with sp-state of metal causing a down-shift of H_2 states. (c) The position of d-band center in a metal. $\epsilon_F^{\text{transition}}$ is the position of Fermi energy of the transition metal which is located below the $(\sigma_g - d)^*$. $\epsilon_F^{\text{noble}}$ is the position of Fermi energy of the noble metal. The light-gray shade indicates the broad sp-orbital of metal while dark-gray indicates the d-band orbital of the metal. (d) The hybridization of the adsorbate states due to the interaction with metal d-state 25

1.12 The significant Kohn-Sham single particle states of CO. Right are the Kohn-Sham energy levels of the orbitals from our DFT calculation employing the GGA approximation. 28

1.13 The Blyholder mechanism: The 5σ orbital and the $2\pi^*$ filled in the formation of hybrids with the substrate. Right is the interaction mechanism with the different d like states on the on-top and hollow adsorption sites. 28

2.1 CO and hydrogen adsorption energies as a function of the number of Pd overlayers on Au for different adsorption sites on the (111) **(a)** and the (100) surface **(b)** at a coverage of $\theta = 0.25$. The pure Pd substrates with the lateral lattice constant of Au (a = 4.18 Å) and Pd (a = 3.96 Å) are labeled by Pd@Au and Pd, respectively. 33

2.2 Position of the local center of the *d*-band with respect to the Fermi energy as a function of the number of Pd overlayers on Au(111) and on Au(100) for the surface and the subsurface layer. The results for a pure Pd substrate with the lateral lattice constant of Au (a = 4.18 Å) and Pd (a = 3.96 Å) are labeled by Pd@Au and Pd, respectively. 35

2.3 Schematic sketch of the change of the H adsorbate height upon lattice expansion. (a) bridge site, (b) threefold hollow site. Upon lattice expansion the hydrogen atoms relax towards the surface so that the optimum H-Pd distance *d* is kept constant. 37

2.4 Local density of states (LDOS) of the hydrogen 1*s* state and the Pd *d*-band for atomic hydrogen adsorption on unstrained Pd(111) at the fcc hollow site (a) and the top site (b) and at top site of strained Pd(111) (c). The hydrogen 1s density of state is multiplied by a factor of 5. The energies are given with respect to the Fermi energy ε_F. 38

2.5 Local d-band density of state (LDOS) for one Pd atom adsorbed per 3×3 surface unit cell on Au(111) and Pd(111) as a function of the energy. The vertical lines indicate the position of the d-band centers. On Au(111), the d-band LDOS of the Pd atom is much narrower and higher in energy than on Pd(111). 39
2.6 Local density of states of the hydrogen 1s state and the Pd subsurface d-band for atomic hydrogen adsorption at the top site of two Pd overlayers on Au(111) The hydrogen 1s density of state is multiplied by a factor of 5. 40
2.7 Charge density difference plot for hydrogen adsorption at the on-top position of two Pd overlayers on Au(111), fcc site (a) and top site (b). White contours correspond to charge accumulation while black contours denote charge depletion. 41
2.8 Hydrogen adsorption height as a function of the number of Pd overlayers at the bridge and fourfold hollow site of of the (100) overlayers systems at a coverage of $\theta = 0.25$. 42
2.9 Hydrogen adsorption energy as a function of the number of Pd overlayers on Au for different adsorption sites on the (111)(a) and the (100) surfaces (b) at the coverage of $\theta = 1$. The pure Pd substrates with the lateral lattice constant of Au (a=4.18 Å) and Pd (a=3.96 Å) are labeled by Pd@Au and Pd, respectively. 43
2.10 Hydrogen adsorption energy on four-fold hollow site (100) surface as a function of the number of Pd overlayer on Au for a coverage $\theta = 0.25$ and coverage $\theta = 1$ 44
2.11 Surface energy in eV/atom according to Eq. 2.1 for different surface compositions of PdCu alloys on Cu(111). The energy zero corresponds to a Cu layer on Cu(111), i.e., to a pure Cu(111) surface. 46
2.12 Atomic hydrogen adsorption energy on bimetallic PdCu surfaces for a quarter monolayer hydrogen coverage, namely on pure Cu(111), on a pseudomorphic Pd overlayer on Cu(111) (Pd/Cu), on pure Pd(111) with the lateral Cu lattice constant (Pd@Cu), on pure Pd(111), on a pseudomorphic Cu overlayer on Pd(111) (Cu/Pd), and on pure Cu(111) with the lateral Pd lattice constant (Cu@Pd). 47
2.13 Position of the local d-band center of the topmost layer on bimetallic PdCu surfaces. The considered structures are the same as in Fig. 2.12. 48
2.14 The local d-band density of state for Pd overlayer on Cu and pure Cu. The horizontal lines indicate the center of d-band position. 48

3.1 (a) adsorption of one Pd atom on (3×3) super cell of Au(111), d is the distance between Pd atoms in the neighboring super cells. (b) The variation of Pd-Pd interaction energy as a function of Pd-Pd distance d. 53
3.2 Schematic sketch of Pd planar clusters on Au substrate. (a) Pd_3 bounded by {111}, (b) Pd_7 bounded by {100}. (c) Pd_7 54
3.3 Relaxation process of the Au atom in the second layer of Pd_3 bounded by {100} due to the Pd relaxation. (a) before Pd relaxation, (b) after Pd relaxation 55

3.4 Calculated CO and hydrogen adsorption energies on planar Pd_3 and Pd_7 clusters deposited on Au(111) compared to the corresponding adsorption energies on the Pd/Au(111) overlayer. 56

3.5 The position of d-band center of Pd_3 and Pd_7 are compared with Pd overlayer on Au(111). The hollow circle symbol in Pd_7 indicated the center of d-band of atom in the center of the cluster (see Fig: 3.2(c)) . . 57

3.6 Orbital resolved *d*-band local density of states (LDOS) of the Pd_3/Au(111), Pd_3/Pd(111) and the free Pd_3 clusters. 58

3.7 one additional Pd atom desorption (black sphere) on Au(111), (a) in one layer next to the Pd_7 cluster, (b) on top of the Pd_7 cluster. 59

3.8 three different modes of thin film growing on a substrate. γ_0, γ_i and γ_s are surface tension of overlayer-vacuum interface, the overlayer-substrate interface and the substrate-vacuum interface respectively. 60

3.9 The structural relaxation of (a) Pd_{10} cluster supported by Au(111) substrate. (b) Pd_{10} cluster supported by Pd substrate with lateral lattice constant of Au (Pd_{10}/Pd@Au). (c) Pd_{10} cluster supported by Pd substrate. (d) free Pd_{10} cluster in gas phase. 61

3.10 Calculated H and CO adsorption energies on the Pd_{10}/Au(111) cluster. The numbers in parentheses correspond to the adsorption energies on free Pd_{10} clusters in exactly the same configuration as the supported clusters. 62

3.11 Calculated H and CO adsorption positions and energies on the free Pd_{10} cluster. 63

3.12 Pd overlayer on $(\sqrt{7} \times \sqrt{7})$ Au(111), (a) a $\Delta l = 0.1$ Å displacement has been applied on Pd atoms along the center of the unit cell. (b) relaxed structure geometry of Pd on $(\sqrt{7} \times \sqrt{7})$ Au(111). 64

4.1 H_2O adsorption on Ru{0001} (a) before H dissociation, O atoms lie in two planes separated by 0.96 Å, dashed lines indicate the H bonds. (b) after H dissociation, the higher-lying O atoms move down and H shifted to on-top site. 66

4.2 Relaxation geometry of water monomer (right) and water dimer (left) adsorption on Pd/Au overlayer surface. 70

4.3 Different water structures for coverage θ=2/3 on a Pd/Au(111) overlayer. (a) H-down bilayer, (b) H-up bilayer, (c) half-dissociated bilayer. Solid lines indicate the H-bond with a shorter H-bond length while dash lines indicate the H-bond with a longer H-bond length. 71

4.4 Top-view of the geometrical relaxation of the hydrogen adsorption on Pd/Au(111) overlayer in presence of a water bilayer for, (a) on-top site, (b) fcc(a) site, (c) hcp(a) site. Due to the presence of the water bilayer the fcc sites are energetically different. fcc(a) and hcp(a) are energetically more favorable compare to fcc(b) and hcp(b) respectively. 73

4.5 Top-view of CO adsorption on Pd/Au(111) overlayer in presence of a water bilayer for, (a) on-top site, (b) fcc hollow site with a shifted water bilayer, (c) fcc hollow site with a three-dimensions water bilayer. The carbon atoms are represented as black spheres 74

List of Tables

2.1 Lattice constant, bulk modulus and cohesive energy of Pd and Au . . . 31

2.2 Layer relaxation of the Pd/Au(111) and Pd/Au(100) overlayer. The DFT-GGA relaxations were computed for the pure Au, one, two, three Pd overlayer on Au and pure Pd. The pure Pd substrates with lateral lattice constant of Au (a=4.18 Å) and Pd (a=3.96 Å) are labeled by Pd@Au and Pd respectively. The relative change to the bulk interlayer distance (in %) is given in parentheses. Positive numbers correspond to a surface expansion away from the bulk substrate. 32

2.3 Atomic hydrogen adsorption height h and nearest-neighbor distance d_{Pd-H} between hydrogen and Pd on various high-symmetry adsorption sites on Pd(111) and Pd(100) as a function of the lattice strain. All distances are given in Å. 37

2.4 Hydrogen adsorption height h, first interlayer spacing d_{12} and relaxation displacement Δ of the second layer atom just below the adsorbate at the fourfold hollow position for unstrained and strained pure Pd(100) and one Pd overlayer on Au(100). The geometry is sketched in the figure above the table. All lengths are in Å. 41

2.5 Lattice constant, bulk modulus and cohesive energy of Cu 45

2.6 Layer relaxation of the Pd/Cu(111) as well as Cu/Pd(111) overlayer surface. The DFT-GGA relaxations were computed for the pure Cu, one Pd overlayer on Cu and pure Pd. The pure Pd (Cu) substrate with lateral lattice constant of Cu (Pd) is labeled by Pd@Cu (Cu@Pd). The relative change to the bulk interlayer distance (in %) is given in parentheses. Positive numbers correspond to a surface expansion away from the bulk substrate. 45

2.7 The binding energy of one Pd atom, Cu atom, Pd overlayer and Cu overlayer on Pd and Cu substrates. 46

3.1 Calculated nearest-neighbor Pd-Pd distances in Å. d_1 and d_2 are the Pd-Pd nearest-neighbor along the two basis vectors **a** and **b** (see Fig. 3.2) 55

4.1 The structural properties of a water molecule and water dimer calculated with USP and PAW pseudopotential and a comparison with experimental values. θ_a and θ_b are angles $O_1 - O_2 - H_3$ and $H_1 - O_1 - H_2$ respectively (see the figure above) 69

4.2 The equilibrium volume, sublimation energy and bulk modulus of 32 molecule of water in ice I_h structure calculated with USP and PAW pseudopotentials 69

4.3 The geometries and energies for water monomer, dimer on Pd/Au(111) overlayer. Z_{OO}, Z_{O-Pd_1}, and Z_{O-Pd_2} are the vertical distances between the top and bottom O atoms, the bottom O and Pd, and the top O and Pd respectively. d_{O-H} is the O-H distance which represents a hydrogen bond 71

4.4 H_2O adsorption energies in eV/H_2O as a function of H_2O coverages. The energies were obtained using ultrasoft pseudopotentials. For the notation of the structures at a water coverage of $\theta_{H_2O} = 2/3$, see Fig. 4.3. 71

4.5 Water adsorption energy values on Pd/Au, Pd with lateral lattice constant of Au (Pd@Au) and pure Pd for coverage θ=2/3 and H-down bilayer. 72

4.6 Hydrogen and CO adsorption energy. $E_{ads}[H_2O]_\downarrow$ and $E_{ads}[H_2O]_\uparrow$ indicate the adsorption energy with H-down and H-up bilayer structure of water respectively. E_{ads}[Clean] indicates the adsorption energy of the clean surface. The superscript 2D and 3D indicate the CO adsorption energy on three fold fcc site in presence of a two-dimensions and three-dimensions bilayer respectively (see Fig. 4.5). 73

Chapter 1

Theory

Ab-initio electronic structure calculations - numerical solutions of Schrödinger's equation for a specific system - are distinct from other forms of modeling because they are first-principles in nature. That is, except through the choice of the researcher, the calculations contain no external parameters other than a most basic description of the system. Calculations of this nature enable the speculative study of systems, potentially without reference to experiment. Where a given physical property is physically inaccessible - such as the binding energy of an atom or molecule deeply embedded in a complex host - the availability of reliable qualitative data is a powerful stimulus.

However, the numerical solution of Schrödinger's equation remains a difficult task. Exact solutions of the equation are, in general, only solvable in times scaling exponentially with system size. This scaling precludes exact calculations for all but the smallest and simplest of systems. Approximations may be introduced to reduce the equations to a form that can be solved in polynomial time, but at the penalty of losing some degree of accuracy and predictive power. The treatment of electron-electron interactions is the principle source of difficulty: the physical and chemical properties of a system depend principally on the interaction of the electrons with each other and with the atomic cores. These interactions cannot easily be separated out or treated without approximation.

1.1 Hamiltonian

From the standpoint of microscopic quantum mechanics, a crystal is a system of the nuclei and electrons interacting through Coulomb forces. The nuclear degrees of freedom are usually disentangled from the electronic once through the adiabatic or Born-Oppenheimer approximation [1] which is based on the smallness of the electron mass as compared to the nuclear mass. Within this approximation the nuclei are regarded as fixed charges acting as potential source for the electrons whose behavior is described by the electronic ground state wavefunction.

$$H_{\mathrm{el}}(\{\mathbf{R}\})\Psi(\mathbf{r},\{\mathbf{R}\}) \;=\; E_{\mathrm{el}}(\{\mathbf{R}\})\Psi(\mathbf{r},\{\mathbf{R}\}) \tag{1.1}$$

where $\Psi(\mathbf{r},\{\mathbf{R}\})$ is the electronic wavefunction and H_{el} is the Hamiltonian of the system of electrons.

The ground state electronic energy $E_{\mathrm{el}}(\mathbf{R})$ is a potential energy surface for the nuclei whose dynamics can also be studied as quantum charges.

$$\Big(T_{\mathrm{nucl}} + E_{\mathrm{el}}(\{\mathbf{R}\})\Big)\,\chi(\mathbf{R}) \;=\; E_{\mathrm{nucl}}\,\chi(\mathbf{R}) \tag{1.2}$$

where $\chi(\mathbf{R})$ is a nuclear wave function. For all atoms except for hydrogen and helium the quantum effects of the nuclei are usually negligible. Hence the classical equation of motion for the nuclei is given by

$$M_I \frac{\partial^2}{\partial t^2}\mathbf{R}_I \;=\; -\nabla_{\mathbf{R}_\mathrm{I}} E_{\mathrm{el}}(\{\mathbf{R}\}) \tag{1.3}$$

where the forces on the ions are obtained from the Hellmann-Feynman theorem

$$\mathbf{F}_\mathrm{I} \;=\; -\nabla_{\mathbf{R}_\mathrm{I}} E_{\mathrm{el}}(\{\mathbf{R}\}) \;=\; \langle \Psi(\mathbf{r},\{\mathbf{R}\})|\frac{\partial}{\partial \mathbf{R_I}} H_{\mathrm{el}}(\{\mathbf{R}\})|\Psi(\mathbf{r},\{\mathbf{R}\})\rangle \tag{1.4}$$

The quantum mechanical properties of the system of N interacting electrons in an external nuclear potential are described by the solution of the Schrödinger many body Eq. 1.1 where H_{el} is the Hamiltonian:

$$H_{\mathrm{el}} = -\frac{\hbar^2}{2m}\sum_{i=1}^{N}\nabla_i^2 + \sum_{i=1}^{N} V_{\mathrm{ext}}(\mathbf{r}_\mathrm{i}) + \frac{e^2}{2}\sum_{i\neq j}\frac{1}{|\mathbf{r}_\mathrm{i}-\mathbf{r}_\mathrm{j}|} \tag{1.5}$$

Here $\mathbf{r}_\mathrm{i}$ is the position of the i-th electron, and $V_{\mathrm{ext}}(\mathbf{r}_\mathrm{i})$ is the external potential which act on the electrons depending parametrically upon the nuclear position. Unfortunately, the solution of Eq. 1.5 can not be found in neither analytic nor numerical form, because of the Coulomb term in the Hamiltonian which couples all the electronic degree of freedom, and for this reason it is convenient to shift the interest from the many-body wavefunction which solve Eq. 1.1 to a non-interacting ground state electronic charge density, which has the same physical ground state properties. Indeed, in practical calculation for systems with many atoms Eq. 1.1 is often replaced by the equations derived from Density Functional Theory (DFT). In the next section we will explain briefly the fundamental principles of the theory and the approximations involved in applying it to any physical problem.

1.2 Density Functional Theory

This theory was introduced in 1964 by Hohenberg and Kohn [2] [3]. It is based on two mathematical theories:

1. The external potential acting on the electrons is a unique functional of the density n(r), therefore the ground state density n_0(r) corresponding to an external potential

$\mathrm{V_{ext}}$ can not be reproduced using any other potential V'_0 that differs by more that an additive constant.

2. The correct ground state density $\mathrm{n_0(r)}$ minimizes the total energy functional.

$$E_{tot}[n] = F_{HK} + E_{ext}[n] = E_{kin}[n] + E_{e-e}[n] + E_{ext}[n] \tag{1.6}$$

All we would like to calculate is the minimum total energy of the system $E_{tot}[n]$ which allows us to determine the ground state charge density and most of the other electronic properties or observable of the system.

1.2.1 Kohn-sham scheme

In order to calculate the minimum total energy of the system, we have to solve the following equation.

$$E_{tot} = \min \langle \Psi | H | \Psi \rangle \tag{1.7}$$

where Ψ is the total wavefunction of the system and

$$H = T + V_{e-e} + V_{ext} \tag{1.8}$$

and T is the kinetic energy operator of the interacting system. In Kohn-Sham theory the many body problem of fully interacting particles in an external potential V_{ext} is simply replaced by a system of non-interacting particles in an effective potential V_{eff} giving the same ground state density. Thus the Hamiltonian of Eq. 1.8 is replaced by

$$H_{\mathrm{s}} = T_{\mathrm{s}} + V_{\mathrm{eff}} \tag{1.9}$$

where T_s is the kinetic energy of non-interacting particles. The effective potential V_{eff}, is local and it is the same for all orbitals.

In the framework of one-particle orbitals $\Psi_i(r)$ the total energy equation can be written as:

$$E_{\mathrm{tot}} = E_{\mathrm{kin,s}} + E_{\mathrm{ext}}[n] + G[n] \tag{1.10}$$

where G[n] is further split into the classical Hartree electron-electron interaction term $E_{\mathrm{Hartree}}[n]$ and an additional term $E_{\mathrm{xc}}[n]$.

$$G[n] = E_{\mathrm{Hartree}}[n] + E_{xc}[n] \tag{1.11}$$

where

$$E_{\mathrm{Hartree}}[n] = \frac{1}{2}\int\int \frac{n(\mathbf{r})n(\mathbf{r}')d\mathbf{r}d\mathbf{r}'}{|\mathbf{r}-\mathbf{r}'|} \tag{1.12}$$

and $E_{\mathrm{xc}}[n]$ includes all the energy contribution which were not taking into account in the transition from the interacting system to the non-interacting system, i.e. so-called electron exchange and electron correlation which introduce quantum mechanical many-body electronic effects into the model and a portion of the kinetic energy which is needed to correct $T_{\mathrm{s}}[n]$ to obtain the true kinetic energy of a real system $T[n]$.

By substituting Eq. 1.11 and Eq. 1.10 into Eq. 1.7 and using variational methods with the constraint:

$$\int n(r)dr = N = const. \tag{1.13}$$

the effective potential V_{eff} will be given as:

$$V_{\text{eff}}[n] = V_{\text{Hartree}}[n] + V_{\text{ext}}[n] + V_{\text{xc}}[n] \tag{1.14}$$

where

$$V_{\text{Hartree}}[n] = \int \frac{n(\mathbf{r})d\mathbf{r}}{|\mathbf{r} - \mathbf{r}'|} \tag{1.15}$$

and

$$V_{\text{xc}}[n] = \frac{\delta E_{\text{xc}}[n]}{\delta n} \tag{1.16}$$

with

$$n(r) = \sum_i^N \phi_i^*(r)\phi_i(r) = \sum_i^N |\phi_i(r)|^2 \tag{1.17}$$

The requirement of the minimization of the energy with respect to a change in the wavefunction leads to a set of single-particle equations known as the Kohn-Sham equation [4]:

$$(-\frac{1}{2}\nabla^2 + V_{\text{Hartree}} + V_{\text{xc}} + V_{\text{ext}})\phi_i = \epsilon_i\phi_i \tag{1.18}$$

This corresponds to a partial differential equation with a Hamiltonian:

$$H_{\text{s}} = -\frac{1}{2}\nabla^2 + V_{\text{Hartree}} + V_{\text{xc}} + V_{\text{ext}} \tag{1.19}$$

The effective potential depends on the density, the Kohn-Sham orbitals ϕ_i on the effective potential, and the density of the orbitals due to its definition Eq. 1.17. This set of equations form a loop which has to be solved self consistently since the Hamiltonian is a functional of wavefunctions through Eq. 1.19 and wavefunctions themselves are the solution of the Hamiltonian: one starts i.e. with an approximate density, constructs the effective potential and solves the Kohn-Sham equation to obtain the orbitals which are then used to calculate the new density etc. This procedure is continued until the density, orbitals and hence total energy no longer change from previous iteration.

Note that although the Kohn-Sham equations 1.18 look like one particle Schrödinger equations, they have been obtained by using the Lagrangian method with Lagrangian multipliers ϵ_i which are not necessarily the one-particle energies.

An alternative expression to the Eq. 1.10 for the total energy can be derived by using the one-particle Kohn-Sham Eq. 1.18[5]

$$E_{\mathrm{tot}} = \sum_{i}^{\mathrm{occ}} \epsilon_i - E_{\mathrm{Hartree}} + E_{\mathrm{xc}} - \int n(r) V_{\mathrm{xc}}(r) dr \tag{1.20}$$

1.2.2 Exchange correlation energy

The above DFT is formally exact, but as such it is useless in practical applications because all the difficulties related to the many-body nature of electron wavefunction are still unsolved.

To proceed further it is necessary to find an approximation for the exchange-correlation energy. The most common approach is the local density approximation LDA [6][2] which describe quite well a large number of systems and has been successfully applied in some ab-initio calculation [7].

The idea is to replace the exchange-correlation energy of a nonuniform system with the E_{xc} computed as if locally the interacting electron gas had the same exchange-correlation energy of a uniform interacting electron gas with the same density. The expression for exchange and correlation energies of homogeneous electron gas [8].

$$\mathrm{E_{xc}[n]} = \int_{\mathrm{V}} \epsilon_{\mathrm{ex}}(\mathrm{n})\mathrm{n}(\mathbf{r})\mathrm{d}\mathbf{r} \tag{1.21}$$

The function $\epsilon_{\mathrm{xc}}(n)$ are based on Monte Carlo calculations of the energy of homogeneous electron gases [9] and it depends locally upon the density at the point r. LDA is exact for a uniform system and is expected to be valid for systems with slowly varying electron density. This approximation has been shown capable of dealing on the same ground with atoms, molecules, clusters, surfaces, interfaces and in many cases also with dynamical (phonon dispersion) and electronic properties which have been successfully reproduced.

Nevertheless, besides these successes there are also some drawbacks of the approximation. For instance, the cohesive energies of solids are systematically overestimates, while lattice constants are systematically underestimated [10][5]. Errors in the structural properties are usually small for crystals with covalent or metallic bonds, but it is well known that the hydrogen bond cannot be described accurately within LDA [11]. In the field of metals, the ground state structure of crystalline iron is predicted to be paramagnetic fcc, instead of a ferromagnetic bcc [12]. Various approximations have been introduced in the course of the years to improve LDA. The generalized gradient approximation (GGA) is one of those approximations which is more or less commonly accepted to be an improvement over LDA.

1.2.3 Generalized gradient approximation

The most obvious way to extend the local density approximation to inhomogeneous systems is to include also the changes or gradient of the density. The easiest way to do that is to try a first order Taylor expansion around the constant density and hope that the inhomogeneities to be small or slowly varying, so that the higher orders of the Taylor expansion will be negligible.

This approach is called Gradient Expansion Approximation (GEA) [3]. Due to rotational invariance of the coefficients of the odd powers of the gradient of density about r, ∇_n vanish. Thus the lowest-order gradient expansion approximation for the exchange reads as [13] [14]:

$$\mathrm{E_x^{GEA}(n, \nabla_n) = E_x^{(0)} + E_x^{(2)} = d_0 \int_r n^{\frac{4}{3}} dr + d_2 \int_r \frac{|\nabla_n|^2}{n^{\frac{4}{3}}} dr} \tag{1.22}$$

where

$$\mathrm{d_0} = -\frac{3}{4}(\frac{3}{\pi})^{\frac{1}{3}}, \qquad \mathrm{d_2} = -\frac{7}{432}(3\pi^5)^{-\frac{1}{3}} \tag{1.23}$$

The zeroth order term is the LDA as expected.

Unfortunately practical tests with the gradient expansion approximation have shown that many properties are less accurately produced than in the LDA. For example the correlation energy in helium and neon atoms has even a wrong sign [15]. Adding second and third order of the Taylor expansion cause a divergence of the exchange potential in atoms both at large and small radii [16].

A different way to include the gradient of the density is to construct a functional which still depends only on the local density n(r) and the magnitude of the gradient $|\nabla_n(r)|$ but whose functional form is no longer chosen to be the one of the exact gradient expansion. Therefore this approach is called the Generalized Gradient Approximation (GGA) - Generalized because of the increased freedom in the choice of the form and approximation because the chosen function usually does not follow the exact lowest-order properties of the electron gas. On the contrary the gradient expansion approximation can be called a gradient correction although the correction terms do not necessarily improve the results.

The choice of the functional form for the GGA is not unique and many different functionals have been proposed. Among the many types of functionals, in this work we used Perdew-Wang 1991 functional (PW91) [17]. In exchange part of this functional, an enhancement factor F over the local density approximation energy is used, while in the correlation the gradient-dependent part is an additive to the correlation of homogeneous density distribution,

$$\mathrm{E_x^{PW}[n, \nabla n]} = \int \mathrm{d^3r\ n(r)}\ \epsilon_{\mathrm{x}}(\mathrm{r_s}, 0)\ \mathrm{F(s)} \tag{1.24}$$

where:

$$\epsilon_x = \frac{-3\mathrm{K_f}}{4\pi}, \qquad \mathrm{K_f} = \frac{1.919}{\mathrm{r_s}} \tag{1.25}$$

and:

$$\mathrm{F(S)} = \frac{1 + 0.1964\mathrm{S}\ \sinh^{-1}(7.795\mathrm{S}) + (0.2743 - 0.1508\mathrm{e}^{-100\mathrm{S}^2})}{1 + 0.1964\mathrm{S}\ \sinh^{-1}(7.795\mathrm{S}) + 0.004\mathrm{S}^2} \tag{1.26}$$

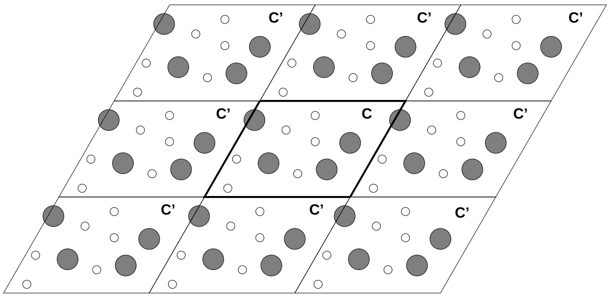

Figure 1.1: replication of super-cell c along x, y and z direction.

where:

$$S = \frac{|\nabla n|}{2K_f\ n} \tag{1.27}$$

The PW-91 correlation energy is

$$E_c^{PW}[n_\uparrow, n_\downarrow] = \int d^3r\ (\epsilon_c^{LDA}(n) + H(t, r_s, \xi))\ n \tag{1.28}$$

where $H = H_0 + H_1$ and

$$H_0 = g^3 \frac{\beta^2}{2\alpha}\ \ln\big[1 + \frac{2\alpha}{\beta} \frac{t^2 + At^4}{1 + At^2 + A^2t^4}\big] \tag{1.29}$$

with $\alpha = 0.09$ and $\beta = 0.0042\ C_c(0)$ and

$$A = \frac{2\alpha}{\beta} \frac{1}{e^{-2\alpha\epsilon_c(r_s,\xi)/g^3\beta^2} - 1}, \tag{1.30}$$

$$g = \frac{(1+\xi)^{1/3} + (1-\xi)^{2/3}}{2}, \tag{1.31}$$

where $t = \frac{|\nabla n|}{2gK_s n}$ and $K_s = (\frac{4K_f}{\pi})^{1/2}$

The second part of function H, H_1 is written as

$$H_1 = \nu\ \big[C_c(r_s) - C_c(0) - \frac{3}{7}C_x\big]\ g^3t^2\ e^{-100g^4t^2K_s^2/K_f^2} \tag{1.32}$$

Accurate analytic representations are available for $\epsilon_c(r_s, \xi)$ and $C_c(r_s)$ in ref. [18][19]

1.3 Methods

1.3.1 Super-cell and Brillouin zone

The one-particle Kohn-Sham Eq. 1.18 can be solved for an isolated system with maximum few hundred number of particles. In a crystal however we are dealing with a order of 10^{23} number of atoms. Simulating such an amount of particles is a impossible task. Therefore a simplification needs to be done. If the system is fully periodic a appropriate choice would be to use periodic boundary conditions. This can be done by using the definition of a Bravais lattice. A Bravais lattice is a fundamental concept in the description of any crystalline solid, which specifies the periodic array in which the repeated units of crystal are arranged. A Bravais lattice is an infinite array of discrete points with an arrangement and orientation that appears exactly the same on all Bravais lattice points. It consist of all points with position vectors $\mathbf{R}$ of the form

$$\mathbf{R} = \mathrm{n}_1\mathbf{a_1} + \mathrm{n}_2\mathbf{a_2} + \mathrm{n}_3\mathbf{a_3} \tag{1.33}$$

where $\mathbf{a_1}$, $\mathbf{a_2}$ and $\mathbf{a_3}$ are any three vectors not all in the same plane and n_1, n_2 and n_3 are all integer values. Therefore if there is an atom or a specific electronic structure at position $\mathbf{r_I}$ the same atom or structure is repeated along three basis vectors $\mathbf{a_{1,2,3}}$ (see Fig 1.1). The calculation saving comes since only the atoms and electrons inside the unit cell of the calculation - called super-cell and shown in the Fig 1.1 with thick solid lines - needs to be explicitly considered.

If non-homogeneities are introduced to the system the periodicity might be lost: this is the case e.g. for point defects in crystals, line defects etc. One approach which has been widely used to deal with such systems is the super-cell approach where the periodic boundary conditions are still preserved but the super-cell is chosen to be so large that the defects do not interact. One example of the super-cell scheme is slab geometry which is used in most of the calculations of surfaces nowadays (see Fig. 1.2(a)). The system is treated periodically in all the three directions but perpendicular to the surface the replicas of the slab are isolated with a large enough region of vacuum in between them. The distance between the slabs has to be carefully chosen to prevent artificial interactions between the two surfaces. In Fig 1.2(b), (c) a bigger super-cell has been chosen due to an additional atom on top of the slab which causes a symmetry breaking along x-direction. The bigger the super-cell is the more computational time is needed to consider all atoms inside the super-cell.

The reciprocal lattice of the Bravais lattice which is also a Bravais lattice consists of the points which satisfy the following equation:

$$\mathrm{e}^{\mathrm{i}\mathbf{G}\cdot\mathbf{R}_\mathrm{I}} = 1 \tag{1.34}$$

where $\mathbf{R}_\mathrm{I}$ is given by Eq. 1.33 and

$$\mathbf{G} = \mathrm{n}_1\mathbf{b_1} + \mathrm{n}_2\mathbf{b_2} + \mathrm{n}_3\mathbf{b_3} \tag{1.35}$$

and $\mathbf{b_{1\ldots3}}$ are reciprocal lattice vectors

$$\begin{aligned}
\mathbf{b_1} &= 2\pi\frac{\mathbf{a_2}\times\mathbf{a_3}}{\mathbf{a_1}\cdot(\mathbf{a_2}\times\mathbf{a_3})}\\
\mathbf{b_2} &= 2\pi\frac{\mathbf{a_3}\times\mathbf{a_1}}{\mathbf{a_1}\cdot(\mathbf{a_2}\times\mathbf{a_3})}\\
\mathbf{b_3} &= 2\pi\frac{\mathbf{a_1}\times\mathbf{a_2}}{\mathbf{a_1}\cdot(\mathbf{a_2}\times\mathbf{a_3})}
\end{aligned} \tag{1.36}$$

Due to the periodicity of the potential energy of our crystal $\mathrm{U}(\mathbf{r})$, the eigenstates Ψ of the one-electron Hamiltonian

$$\mathrm{H} = -\frac{\hbar^2}{2\mathrm{m}}\nabla^2 + \mathrm{U}(\mathbf{r}) \tag{1.37}$$

where $\mathrm{U}(\mathbf{r}+\mathbf{R}) = \mathrm{U}(\mathbf{r})$ for all $\mathbf{R}$ in a Bravais lattice can be chosen to be of the form of a plane wave times a function with the periodicity of the Bravais lattice (Bloch's theorem) [20].

$$\Psi_{\mathrm{nk}}(\mathbf{r}) = \mathrm{e}^{\mathbf{ik\cdot r}}\mathrm{u}_{\mathrm{nk}}(\mathbf{r}) \tag{1.38}$$

where i is the band index and $\mathbf{k}$ is a point in the first Brillouin zone. It follows that

$$\Psi_{\mathrm{nk}}(\mathbf{r}+\mathbf{R}) = \mathrm{e}^{\mathbf{ik\cdot R}}\Psi_{\mathrm{nk}}(\mathbf{r}) \tag{1.39}$$

which indicates that the transformation by a multiple of a lattice vector introduce a modulation of a phase of a wave function with the periodicity of the real space lattice. Thus:

$$\left|\Psi_{\mathrm{nk}}(\mathbf{r}+\mathbf{R})\right|^2 = \left|\Psi_{\mathrm{nk}}(\mathbf{r})\right|^2 \tag{1.40}$$

With this new notation of the wave function, the single-particle Kohn-Sham Eq. 1.18 is given by:

$$(-\frac{1}{2}\nabla_r^2 + V_{\mathrm{Hartree}} + V_{\mathrm{xc}} + V_{\mathrm{ext}})\Phi_{ik} = \epsilon_{ik}\Phi_{ik} \tag{1.41}$$

The problem of considering a infinite number of electrons in a crystal is now transformed into a - still infinite - set of wave function of a plane wave times a periodic function. Therefore the quantities like electronic kinetic energy or charge density which contain the full set of wave function are transformed into integrals over the k-points in the first Brillouin zone.

$$\mathrm{E}_{\mathrm{kin}}[\{\Psi\}] = \sum_{\mathrm{i}}\int_{\mathbf{k}\in 1^{\mathrm{st}}\mathrm{BZ}} \mathrm{d}\mathbf{k}\int_{\mathbf{r}}\Psi^*_{\mathrm{ik}}(\mathbf{r})\big(-\frac{1}{2}\nabla^2\big)\Psi_{\mathrm{ik}}(\mathbf{r})\mathrm{d}\mathbf{r} \tag{1.42}$$

$$\mathrm{n}[\{\Psi\}](\mathrm{r}) = \sum_{\mathrm{i}}\int_{\mathbf{k}\in 1^{\mathrm{st}}\mathrm{BZ}} \mathrm{d}\mathbf{k}\int_{\mathbf{r}}\Psi^*_{\mathrm{ik}}(\mathbf{r})\Psi_{\mathrm{ik}}(\mathbf{r})\mathrm{d}\mathbf{r} \tag{1.43}$$

The advantage of such a transformation comes when we notice that the integrals can be transformed into sums over a finite set of k-points in the first Brillouin zone and converge with just few but special number of k-points which will be discussed in the next section.

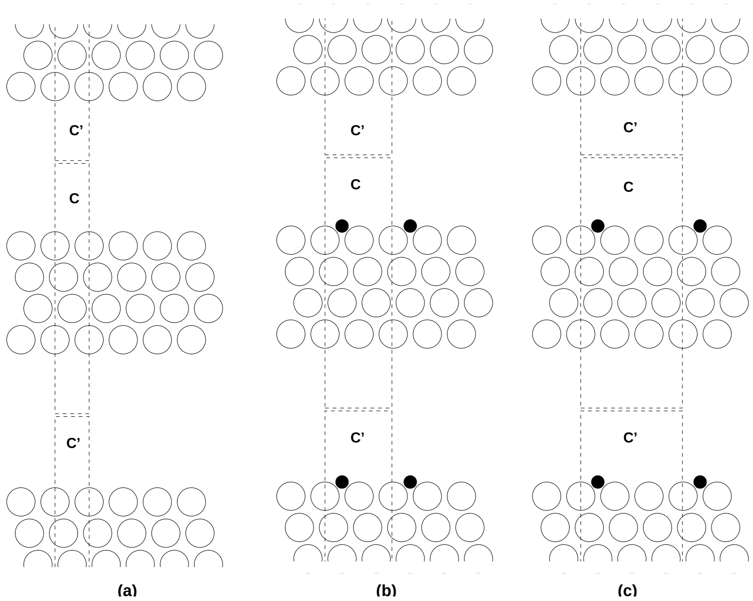

Figure 1.2: replication of super-cell c along x, y and z direction. (a) The clean surface(111) with 1×1 super-cell, (b) 2×2 super-cell with 1/4 coverage of black atoms. (c) 3× 3 super-cell with coverage 1/9 of black atoms.

1.3.2 Special k-points

In order to calculate equations such as the Eq. 1.42 and Eq. 1.43 numerically we need to approximate the integral over the first Brillouin zone by a sum. the integral is replaced with a finite weighted sum over a set of discrete points.

$$\frac{1}{(2\pi)^3}\int_{\mathbf{k}} \mathrm{f}(\mathbf{k})\mathrm{d}\mathbf{k} \rightarrow \frac{1}{\Omega}\sum_{\mathbf{k}_\mathrm{i}} \omega_{\mathbf{k}_\mathrm{i}} \mathrm{f}(\mathbf{k}_\mathrm{i}) \tag{1.44}$$

where Ω the size of the super-cell, $\mathbf{k}_\mathrm{i}$ form the set of k-points and $\omega_{\mathbf{k}_\mathrm{i}}$ are corresponding weights chosen to weight the contribution from the different k-points correctly. Choosing a sufficiently dense mesh of integration points is crucial for the convergence of the results, and is therefore one of the major objectives when performing convergence tests.

The k-points have to be chosen to span only the irreducible part of the Brillouin zone, defined as the smallest wedge of the first Brillouin zone which can not be reduced any further with symmetry operations.

Please note that for surfaces in one direction the electron system does not interact over the periodicity and therefore in this direction there cannot be any hybridization of the wave functions and thus no dispersion. Hence the Brillouin zone reduces to a single point in the direction perpendicular to the surface. Therefore for an atom or molecule the $\mathbf{\Gamma}$ point (0,0,0) alone is enough for the summation over the Brillouin zone. In the case of surface the Brillouin zone is indeed a surface and has two dimensions.

Here we shall describe the method of Monkhorst and Pack [21] to generate the k-points in the first Brillouin zone. We used this method in our entire calculations.

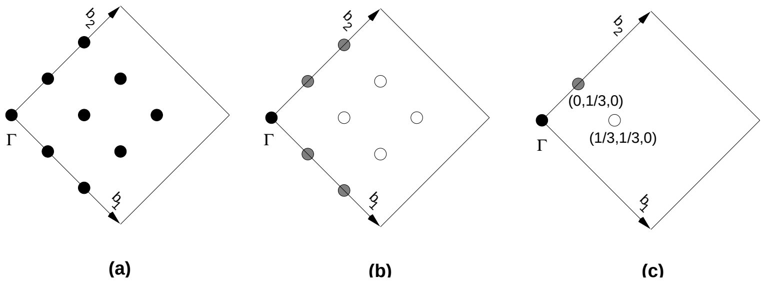

Figure 1.3: (a) The position of k-points in reciprocal space in surface (100) with $q_1 = q_2 = 3$. (b) Due to the symmetry, all symmetrically equivalent points are shown with the same symbol. (c) The position of the irreducible k-points.

The method is simply based on linear combination of reciprocal lattice vectors $\mathbf{b}_1$, $\mathbf{b}_2$ and $\mathbf{b}_3$:

$$\mathbf{k} = n_1\mathbf{b}_1 + n_2\mathbf{b}_2 + n_3\mathbf{b}_3 \tag{1.45}$$

The coefficient n_1, n_2 and n_3 are given by

$$n_i = \frac{2r_i - q_i - 1}{2q_i} \qquad (r_i = 1, 2, 3, ..., q_i) \tag{1.46}$$

where q_i is an integer that determines the number of special points for each direction in the set. The total number of k-points generated by this method are as many as $q_1 \times q_2 \times q_3$. In the case of a surface, the number of k-points is given by $q_1 \times q_2$ due to the two-dimensional Brillouin zone. Fig. 1.3(a) indicates a k-point set with $q_1 = q_2 = 3$ for the reciprocal lattice of a (100) surface. Due to the symmetry operations identity, inversion, a mirror plane and a four-fold rotation (see Fig. 1.3(b)) the number of k-points reduced to a so-called irreducible k-point set containing 3 k-points. The positions of the irreducible k-points are shown in Fig. 1.3(c).

Please note that the $\mathbf{\Gamma}$ point (0,0,0) is contained in the $\mathbf{k}$ point set only if all q_i are odd because $\mathbf{b}_1$, $\mathbf{b}_2$ and $\mathbf{b}_3$ are linearly independent and therefore n_1, n_2 and n_3 must all simultaneously be equal to zero. However it is demonstrated in Fig. 1.4 that a reciprocal space with even number of q_i with $q_1 = q_2 = q_3 = 4$ does not include the $\mathbf{\Gamma}$ point. In order to include the $\mathbf{\Gamma}$ point a shift of the k-point set has to be done (see Fig. 1.5). This shift causes a mirror symmetry breaking which leads to a increase in the number of k-points from 3 to 6 (see Fig. 1.5(b)).

Please note that for a point at Γ in Fig. 1.3 there is no any symmetrically equivalent points in that super-cell. Therefore the weight of the point at Γ is $\omega = 1$, but for a point at position $(0, \frac{1}{3}, 0)$ there are 4 symmetrically equivalent points in the super-cell. Therefor the weight of that point is $\omega = 4$.

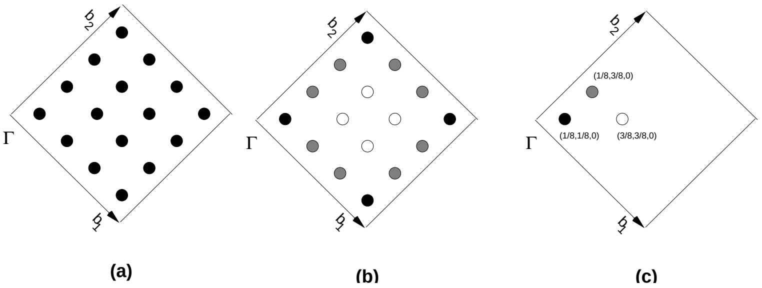
b_2
Γ
b_1
b_2
Γ
b_1
b_2
(1/8,3/8,0)
Γ
(1/8,1/8,0)
(3/8,3/8,0)
b_1

(a) (b) (c)

Figure 1.4: (a) The position of k-points in reciprocal space in surface (100) with $q_1 = q_2 = 4$. (b) All points with the same symbol are identical due to the symmetry. (c) The positions of the irreducible k-points.

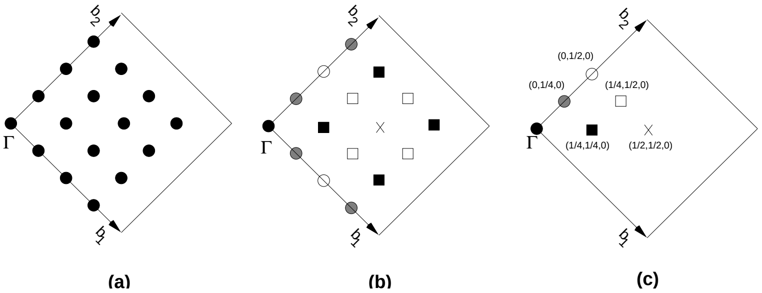
b_2
Γ
b_1
b_2
Γ
b_1
b_2
(0,1/2,0)
(0,1/4,0)
(1/4,1/2,0)
Γ
(1/4,1/4,0)
(1/2,1/2,0)
b_1

(a) (b) (c)

Figure 1.5: (a) The position of k-points in reciprocal space in surface (100) with $q_1 = q_2 = 4$. (b) The symmetry between the positions. All the points with the same symbol are identical due to the symmetry. (c) The position of the irreducible k-points.

1.3.3 Basis set-Plane wave

In order to solve the Kohn-Sham Eq. 1.41 for every state i and k-point **k** numerically, we need to expand the wave function $\Psi_{\mathrm{ik}}(\mathrm{r})$ in a basis set:

$$\Psi_{\mathrm{ik}}(\mathrm{r}) = \sum_{\mathrm{n=1}}^{\mathrm{N_{basis}}} \mathrm{C_{ik,n}}\ \chi_{\mathrm{n}}(\mathrm{r}) \tag{1.47}$$

where n goes through the basis function $\chi_{\mathrm{n}}(\mathrm{r})$ up to a finite count $\mathrm{N_{basis}}$ and $\mathrm{C_{ik}(n)}$ are the expansion coefficients. The idea is to look for $\chi_{\mathrm{n}}(\mathrm{r})$ which solve the Kohn-Sham equations, thus a straightforward implementation leads to the equations:

$$\sum_{\mathrm{n}} \mathrm{C_{ik,n}}\ \mathrm{H}\ \chi_{\mathrm{n}}(\mathrm{r}) = \epsilon_{\mathrm{i}} \sum_{\mathrm{n}} \mathrm{C_{ik,n}}\ \chi_{\mathrm{n}}(\mathrm{r}) \tag{1.48}$$

Multiplying with χ^*_{m} from the left and integrating over the space these equations become:

$$\sum_{\mathrm{n}} \mathrm{C_{ik,n}}\ \mathrm{H_{mn}} = \epsilon_{\mathrm{i}} \sum_{\mathrm{n}} \mathrm{C_{ik,n}} \mathrm{O_{mn}} \tag{1.49}$$

where $\mathrm{H_{mn}} = \langle \chi_{\mathrm{m}} | \mathrm{H} | \chi_{\mathrm{n}} \rangle$ and $\mathrm{O_{mn}} = \langle \chi_{\mathrm{m}} | \chi_{\mathrm{n}} \rangle$.

These equations can be expressed in a matrix form, noting that the k-points are independent. Eq. 1.49 is a general equation for an arbitrary basis. The matrix eigenvalue problem can be solved by a direct diagonalization of the matrix **H**. However the diagonalization scales in the third power and the storage needed in the square power of the matrix size. In this case the matrix size is given by the number of basis functions $\mathrm{N_{basis}}$ which in most cases leads to a huge number of matrix element. Therefore an interactive method to avoid the direct diagonalization will become advantageous.

One of the widely used basis set is the plane wave basis due to the simplicity and high efficiency. The wave function in this basis is given by

$$\Psi_{\mathbf{ik}}(\mathbf{r}) = \sum_{\mathbf{G}}^{\mathbf{G}\mathrm{max}} \mathrm{C}_{\mathbf{ik}}(\mathbf{G}) \mathrm{e}^{\mathrm{i}(\mathbf{G}+\mathbf{k})\cdot\mathbf{r}} \tag{1.50}$$

where

$$\mathbf{G} = \mathrm{i}\mathbf{b}_1 + \mathrm{j}\mathbf{b}_2 + \mathrm{k}\mathbf{b}_3 \tag{1.51}$$

with **b**'s the reciprocal lattice vectors and i,j,k integer values.

Among the many types of basis sets the plane wave basis set has the following advantages:

- They are orthogonal

  $$< \mathrm{g}|\mathrm{g}' >= \int_{\mathrm{r}} \mathrm{e}^{-\mathrm{ig.r}} \mathrm{e}^{\mathrm{ig'.r}} \mathrm{dr} = \delta_{\mathrm{gg'}} \tag{1.52}$$

  therefore the overlap matrix O in Eq. 1.49 becomes a diagonal unit matrix and vanishes from our eigenvalue problem.

- Some terms of Kohn-Sham arrays and potential are diagonal in reciprocal space, one example is the electronics kinetic energy

$$\mathrm{E_{kin}} = \sum_{\mathbf{ik}} \mathrm{f_{\mathbf{ik}}} \omega_{\mathbf{k}} \int_{\mathbf{r}} \Psi^*_{\mathbf{ik}}(\mathbf{r})(-\frac{1}{2}\nabla^2_{\mathbf{r}})\Psi_{\mathbf{ik}}(\mathbf{r})\mathrm{d}\mathbf{r} = \\ \sum_{\mathbf{ik}} \mathrm{f_{\mathbf{ik}}} \omega_{\mathbf{k}} \sum_{\mathbf{G}}^{\mathrm{N_G}} |\mathbf{k}+\mathbf{G}|^2 |\mathrm{C}_{\mathbf{ik}}(\mathbf{G})|^2 \tag{1.53}$$

  In our calculation we need to transfer a large number of functions from reciprocal space to the real space and vise versa in every self consistence iteration. This can be done very efficiently using the Fast Fourier Transform FFT technique [22].

- Plane wave basis does not depend on the positions of the atoms, therefore there will be no pullay forces in our calculation.

The disadvantage of using the plane wave basis set is that we need a large number of plane waves to get a precise convergence of the total energy as a function of the number of plane wave. The numbers of plane waves are characterized by the so-called cut-off energy $\mathrm{E_{cut}}$. It is defined as the kinetic energy of the largest frequency or longest $\mathbf{G}$ vector in the expansion at each $\mathbf{k}$.

$$\frac{1}{2}|\mathbf{k}+\mathbf{G}|^2 \leq \mathrm{E_{cut}} \tag{1.54}$$

According to Eq. 1.54 all the points inside a sphere with a radius $\mathbf{G}_{\mathrm{cut,wf}} = \sqrt{2\mathrm{E_{cut}}}$ are allowed to contribute to the wave function expansion Eq. 1.50. In Fig. 1.6 a specific two-dimensional reciprocal lattice space is shown. The number of G vectors corresponds to all points inside the sphere with radius $\mathbf{G}_{\mathrm{cut,wf}}$. Please note that the bigger the super-cell is, the shorter the G length are and therefore a larger number of G vectors has to be considered. $\mathrm{E_{cut}}$ is a quantity which has to be set in a region where the total energy versus $\mathrm{E_{cut}}$ is converged. Unfortunately in the basis set plane wave, this quantity is large and therefore a large number of plane wave is needed. One reason is that the kinetic energy of the wave function close to the nucleus is large thus higher Fourier coefficient in the wave function expansion Eq. 1.50 are needed and therefore we need a higher $\mathrm{E_{cut}}$ to reach the convergence. Although in section 1.3.4 we will try to replace the real wave function with a smooth pseudo wave function without loosing any physical or chemical properties of the system, the number of plane wave is still so large that we can not simulate a system containing more than a few hundred number of atoms.

The density from the Kohn-sham orbitals is easily calculated in real space, and it is diagonal in the reciprocal space

$$\mathrm{n}(\mathbf{r}) = \sum_{\mathrm{i},\mathbf{k}} \mathrm{f}_{\mathbf{k}} \omega_{\mathbf{k}} |\Psi_{\mathbf{ik}}(\mathbf{r})|^2 \tag{1.55}$$

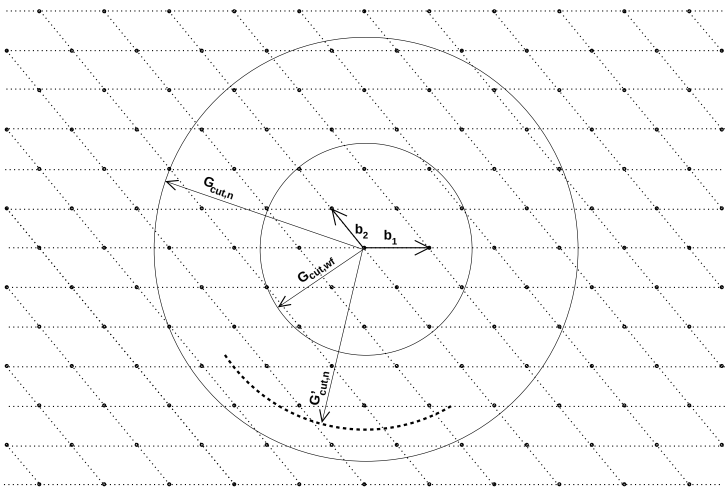

Figure 1.6: The construction of $\mathbf{G}$ vectors in two-dimension. $\mathbf{b}_1$ and $\mathbf{b}_2$ are the reciprocal lattice vectors and all the crossing of the line give a $\mathbf{G}$ vector. The cut-off sphere for the wave functions $\mathbf{G}_{\text{cut,wf}}$ and density $\mathbf{G}_{\text{cut,n}} = 2\mathbf{G}_{\text{cut,wf}}$ as well as for density with dualling $\mathbf{G'}_{\text{cut,n}} < 2\mathbf{G}_{\text{cut,wf}}$ are shown (the latter partially, with a dash line). Please note that $\mathbf{k}$=0 was used for the cut-off sphere of the wave function.

where $\text{f}_\mathbf{k}$ are the occupation factors for each k-point k and index band i. Due to the fact that the density is not a function of the k-points, the Fourier transform of the density contains only reciprocal vectors G, but for constructing such a charge density we need two times larger wave vectors G. The reason can be easily demonstrated by investigating the square of the function cos(x) + sin(x):

$$(\cos(\text{x}) + \sin(\text{x}))^2 = 1 + \sin(2\text{x})$$

i.e. the oscillation of the square of a function can contain frequencies twice higher than the function itself. In general it can be shown that a convolution $f_r = f_r^1 f_r^2$ of two function f_r^1 with Fourier components up to G_1 and f_r^2 with Fourier components up to G_2 contains Fourier component up to $G_1 + G_2$. Similarly to the density all the potential terms except for the non-local part of the pseudopotential (see section 1.3.4) contain wave vectors up to $\text{G}_{\text{cut,n}} = 2\text{G}_{\text{cut,wf}}$ and thus $\text{E}_{\text{cut,n}} = 4\text{E}_{\text{cut,wf}}$. The factor 4 can usually be reduced from its ideal value to about 2.5 ... 3 - a trick to save some computer time called dualling [23] and depicted in the Fig. 1.6 - when employing the local density approximation but should not be reduced at least as much when using more complicated exchange-correlation functional like e.g. the generalized gradient approximation because these require a higher precision due to their higher non-linearity.

One very useful benefit from working with reciprocal space is that the calculation of atom-centered properties becomes very efficient and continuous with respect to a translation of the atoms. This is because if a function f depends on the position $\mathbf{R}_\text{I}$:

$$\begin{aligned}\mathrm{F}[f(\mathbf{r}-\mathbf{R}_\mathrm{I})](\mathbf{G}) &= \int_{\mathbf{r}} f(\mathbf{r}-\mathbf{R}_I)e^{i\mathbf{G}\cdot\mathbf{r}}d\mathbf{r} = \int_{\mathbf{r}'} f(\mathbf{r}')e^{i\mathbf{G}\cdot(\mathbf{r}'-\mathbf{R}_\mathrm{I})}d\mathbf{r}' \\ &= \mathrm{e}^{\mathrm{i}\mathbf{G}\cdot(\mathbf{R}_\mathrm{I})}\int_{\mathbf{r}'} f(\mathbf{r}')e^{i\mathbf{G}.\mathbf{r}'}d\mathbf{r}' = e^{i\mathbf{G}\cdot\mathbf{R}_I}\mathrm{F}[f(\mathbf{r})]\end{aligned} \tag{1.56}$$

i.e. the atomic position enters only as a phase factor while in the real space an interpolation to the grid points would be necessary. Also the gradients with respect to **r** and ionic positions $\mathbf{R}_I$ are trivial

$$\frac{\partial}{\partial\mathbf{r}}f(\mathbf{r}) = \sum_{\mathbf{G}} i\mathbf{G}f(\mathbf{G})e^{i\mathbf{G}\cdot\mathbf{r}} = \mathrm{F}^{-1}[\mathrm{i}\mathbf{G}f(\mathbf{r})] \tag{1.57}$$

$$\frac{\partial}{\partial\mathbf{R}_\mathrm{I}}f(\mathbf{r}-\mathbf{R}_I) = \sum_{\mathbf{G}} i\mathbf{G}e^{i\mathbf{G}\cdot\mathbf{R}_I}f(\mathbf{G})e^{i\mathbf{G}\cdot\mathbf{R}_I} = \mathrm{F}^{-1}[\mathrm{i}\mathbf{G}\mathrm{e}^{\mathrm{i}\mathbf{G}\cdot\mathbf{R}_\mathrm{I}}f(\mathbf{G})] \tag{1.58}$$

The latter equation guarantees also a very convenient way of calculating the forces acting on the ions. The evaluation of the forces is extremely trivial since the basis set does not depend on the atomic position and is complete, therefore the Hellmann-Feynman theorem states that

$$\mathbf{F}_I = \frac{\partial E_{KS}}{\partial\mathbf{R}_I} \tag{1.59}$$

i.e. it does not contain any Pulay corrections [24], which are often difficult to calculate.

1.3.4 Pseudopotential

The potential energy in the core region - the region close to the nucleus - in a atom or solid is more negative than in the valence region - the region far enough from the nucleus - therefore the electronic kinetic energy of the valence electrons in this region must be high enough to compensate the potential energy and produce a relatively low energy compared to the core atoms. Therefore the valence orbitals in the core region have fast oscillations. Orthogonality of valence orbitals in the core region where there are lots of core orbitals is another reason why the valence orbitals oscillate fast in the core region.

Unfortunately plane waves cannot be straightforwardly used with Eq. 1.50 because of the fast oscillation of the orbitals in the neighborhoods of the nuclei, which would require an enormous basis size to be described with acceptable resolution.

However, the energies associated with the core wave functions are orders of magnitude higher than the energies associated with the valence wave functions and it is well known that the properties of chemical bonds are determined by the valence charge density quite far from the nuclei, while the core electrons remains almost inert, frozen in their atomic configuration. Hence in the first step it is possible to simplify the single-orbital Kohn-Sham Eq. 1.18 by eliminating all the degree of freedom associated with those electrons which are so tightly bound to the nuclei that their energy does

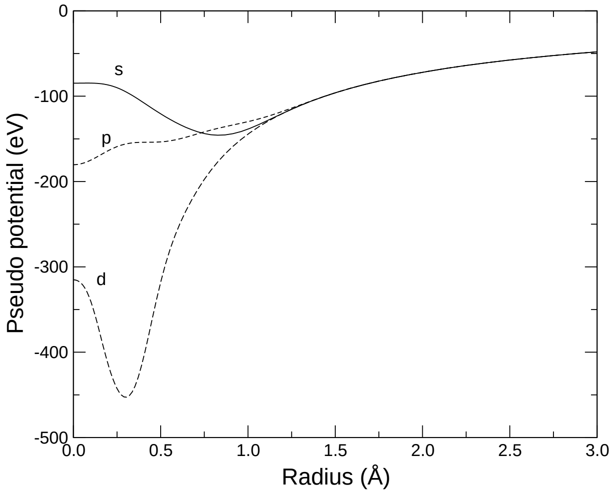

Figure 1.7: An example for a pseudo potential: A pseudo potential for Pd

not change when the atoms form a solid. It is then possible to map the all-electron frozen-core problem onto an equivalent problem involving valence electrons only.

Due to the fact that all the chemical properties of the system can be described only by the wave functions in the valence region, it is then possible in the second step to smooth out the wave function of the valence electron in the region close to the nuclei. The orbitals associated with those electrons can then be described by a reasonable number of plane waves. This smoothed wave function is called pseudo wave function and the potential which can produce such a pseudo wave function is called pseudo potential. The formal transformation of the Hamiltonian is the substitution of the nuclear potential with a new pseudo potential whose lowest energies coincide with the valence all-electron energies and whose wave function coincide with the all-electron wave function in the region $\mathrm{r} > \mathrm{r_c}$ where $\mathrm{r_c}$ is the core radius [25]. An example of a pseudo potential is shown in the Fig. 1.7. It shows a pseudo potential for a palladium atom, whose valence configuration is $5\mathrm{s}^1 4\mathrm{d}^9$. The ionic pseudo potential consist of a Coulomb attractive term, whose charge is given by the atomic valence, plus a short-range part, which must be able to correctly represent the effect of the orthogonalization of the valence eigenfunction to the core ones, the effect of the integration of the valence electron with the electrostatic potential of the core charge and the effect of the exchange-correlation between valence and core eigenfunctions.

Pseudo potentials whose norm of the corresponding wave functions

$$4\pi \int_{\mathrm{r}=0}^{\mathrm{r_c}} |\phi(\mathrm{r})|^2 \mathrm{r}^2 \mathrm{dr} \tag{1.60}$$

is the same for the pseudo and all-electron orbital inside the core radius $\mathrm{r_c}$ are called norm conserving pseudo potential [26]. This norm conservation guarantees that the electrostatic potential felt by the pseudo valence function out-side the core radius is identical to the all-electron one. The norm conservation further ensures that the logarithmic derivative of the pseudo and all-electron wave function and their first energy derivatives agree out-side the core radius. This is important for scattering properties of the electrons and thus for the over-all transferability of the pseudopotential from the isolated atom (where the pseudopotential is generated) to the solid. The price to be paid for norm-conservation is non-locality i.e. the ionic pseudo potential depends upon the angular momentum l.

$$\mathrm{V}_{\mathrm{ext}}^{\mathrm{ps}}(\mathrm{r}) = \mathrm{V}_{\mathrm{local}}(\mathrm{r}) + \sum_{lm} \mathrm{V}_{\mathrm{nl}}(\mathrm{r})\ |lm\rangle\langle lm| \tag{1.61}$$

where $\mathrm{V}_{\mathrm{nl}}(\mathrm{r})$ is the non-local part of the pseudo potential and $|lm\rangle$ is the spherical harmonic of angular momentum l. In this way the internal potential becomes a semi local operator. Then the matrix elements become

$$\langle\chi_1|\mathrm{V}_{\mathrm{ext}}^{\mathrm{ps}}(\mathrm{r})|\chi_2\rangle = \langle\chi_1|\mathrm{V}_{\mathrm{local}}(\mathrm{r})|\chi_2\rangle + \sum_{lm} \mathrm{V}_{\mathrm{nl}}(\mathrm{r})\langle\chi_1|lm\rangle\langle lm|\chi_2\rangle \tag{1.62}$$

where χ_1 and χ_2 are basic set functions. The following kind of construction was proposed by Kleinman-Bylander [27] and is in use in most of the pseudo potential calculations. The pseudo potential term of Kleinman-Bylander reads as:

$$\mathrm{V}_{\mathrm{ext}}^{\mathrm{ps}}(\mathrm{r}) = \mathrm{V}_{\mathrm{local}}(\mathrm{r}) + \sum_{lm} |\Delta\mathrm{V}_{\mathrm{ps}}^{l}(\mathrm{r})\phi_l(\mathrm{r})|lm\rangle\ \mathrm{E}_{\mathrm{KB}}^{l}\ \langle lm|\Delta\mathrm{V}_{\mathrm{ps}}^{l}(\mathrm{r})\phi_l(\mathrm{r})| \tag{1.63}$$

where

$$\mathrm{E}_{\mathrm{KB}}^{l} = \frac{1}{\langle\phi_l(\mathrm{r})|\ \Delta\mathrm{V}_{\mathrm{ps}}^{l}(\mathrm{r})\ |\phi_l(\mathrm{r})\rangle} \tag{1.64}$$

and $\Delta\mathrm{V}_{\mathrm{ps}}^{l}(\mathrm{r}) = \mathrm{V}_{\mathrm{nl}}^{l}(\mathrm{r}) - \mathrm{V}_{\mathrm{local}}(\mathrm{r})$. The Kleinman-Bylander transformation indeed converts a double integral to a single integral and therefore it helps to save computer time and reduce storage requirement.

One of the first non-local pseudo potentials has been generated by the concept of Hamann, Schlüter and Chiang. The pseudo potentials generated have the unpleasant feature that they are often very hard. That means they require higher basis sets in the calculation for the solid, especially for a plane wave basis. Fig. 1.7 shows this kind of pseudo potential for Palladium. The hard pseudo potentials occur mostly for the right-most second row and transition metal elements, where the 2p and 3d, 4d or 5d orbitals are very localized, especially the 2p and 3d where there is no orbital lower in energy with the same angular momentum to against which the orbital should be orthogonal and thus the orbital can remain more localized. To overcome the problem with too hard pseudo potentials, new schemes were devised: Kerker [28], Vanderbilt [29] , Rappe [30] and Troullier and Martin [31] are examples. Fig. 1.8 shows also the 4d pseudo orbital of the Palladium generated with the scheme of Troullier and Martin, and the dip in the Hamann, Schlüter, Chiang is smoothed away. The smoother, softer pseudo potential are achieved by selecting a larger core radius, thus allowing for large freedom in the generation by choosing a form which leads to a softer potential. The results of having a larger core radius is a large reduction in the plane wave basis set

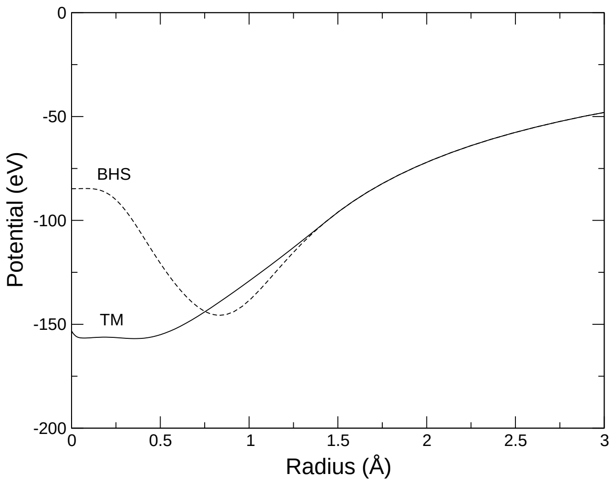

Figure 1.8: An example of a hard Hamann-Schlüter-Chiang and a soft Troullier-Martin pseudo potential for Pd.

but usually the transferability of the pseudo potentials generated according to Hamann, Schlüter and Chiang is better due to the smaller core radius used.

A more radical approach to increase the smoothness was invented by Vanderbilt [32] and first implemented by Kari Laasonen [11] . This kind of pseudo potential is not norm-conserving in the sense that the pseudo wave function does not have to have the same norm inside the core radius as all-electron wave function as seen in the Fig. 1.9. The pseudo wave function may thus avoid the peak in the orbital (in this case the 4d orbital) and therefore a much softer pseudo wave function results. The charge missing from the square of the wave function is later augmented with the missing charge. The complications arising from the charge augmentation partially diminished the advantage gained from the lower basis set size needed. In this work ultra soft pseudopotentials (USP) are used.

1.3.5 Fractional occupation numbers

One of the main tasks in DFT calculation is to determine the total energy of the system. In order to do that it is necessary to calculate the band structure term

$$\sum_{\mathrm{i}} \frac{1}{\Omega_{\mathrm{BZ}}} \int_{\Omega_{\mathrm{BZ}}} \epsilon_{\mathrm{ik}}\ \Theta(\epsilon_{\mathrm{ik}} - \mu)\ \mathrm{d}\mathbf{k} \tag{1.65}$$

where Ω_{BZ} is the volume of the first Brillouin zone, ϵ_{ik} is the energy for each band i and k-point $\mathbf{k}$ and $\Theta(\epsilon_{\mathrm{ik}} - \mu)$ is the Dirac step function and it can be either 1 for those energies which are below the Fermi energy or zero for energies above the Fermi energy. Due to the finite computer resources this integral has to be evaluated using a discrete set of k-points

$$\frac{1}{\Omega_{\mathrm{BZ}}} \int_{\Omega_{\mathrm{BZ}}} \rightarrow \sum_{\mathrm{k}} \omega_{\mathrm{k}} \tag{1.66}$$

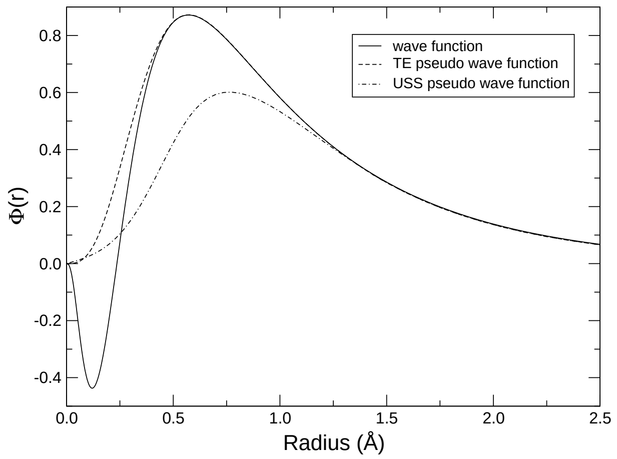

Figure 1.9: An example of the all electron wave function - times radius r - (solid line), pseudo wave function of the Troullier-Martin (dash line) and a Vanderbilt ultra-soft pseudo wave function (dash-dot line) for Pd.

where the sum is over all special k-points (see section 1.3.2). Substituting Eq. 1.66 into Eq. 1.65 we get:

$$\sum_{\mathrm{i}}\sum_{\mathrm{k}}\omega_{\mathrm{k}}\ \epsilon_{\mathrm{ik}}\ \Theta(\epsilon_{\mathrm{ik}}-\mu) \tag{1.67}$$

Since the energy of states above Fermi energy do not enter in the total energy calculation, therefore for semiconductors or isolators the Dirac step function is simply replaced with one for each band in each k-point because there is a gap between the highest occupied band and the lowest unoccupied bands. Hence the integral can be calculated accurately using a few number of k-points.

For metals where some occupied states cross the Fermi energy, the Dirac step function can not be replaced with Θ=1 but rather jump from 1 to 0 at the Fermi energy μ. This jump causes the convergence exceedingly slow with the number of the k-points included. Fig. 1.10 shows the total energy as a function of k-points for a arbitrary function for ϵ_{ik}. The function exceeds the Fermi energy in some points. As it has been shown in Fig. 1.10(b) the total energy convergence has not been reached even for large number of k-points. The trick is now to replace the step function $\Theta(\epsilon_{\mathrm{ik}}-\mu)$ by a smooth function $\mathrm{f}(\{\epsilon_{\mathrm{ik}}\})$ resulting in a much faster convergence without destroying the accuracy of the sum.

Several functional forms has been proposed for the $\mathrm{f}(\{\epsilon_{\mathrm{ik}}\})$, linear tetrahedron method [33] and finite-temperature [34] are examples in this approach. Since in this work we have used exclusively finite-temperature or what is called smearing method, here we focus on this method and try to explain its basics concepts.

Within this method the step function is simply replaced by a smoothly varying function, for example the integral over the Gaussian

$$\mathrm{f}(\frac{\epsilon_{\mathrm{n}}-\mu}{\sigma})=\frac{1}{2}\Big(1-\mathrm{erf}(\frac{\epsilon_{\mathrm{n}}-\mu}{\sigma})\Big) \tag{1.68}$$

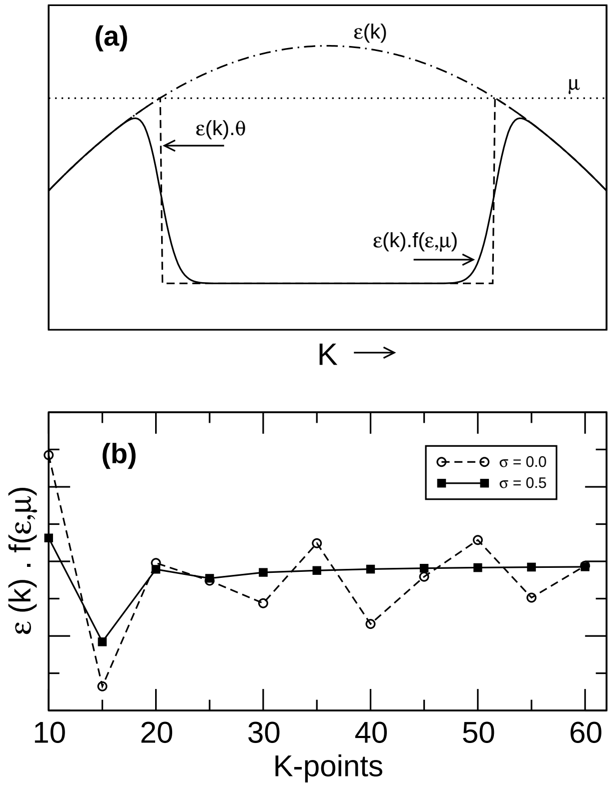

Figure 1.10: (a) An example of a arbitrary function ϵ(k) (dash-dot line) which exceeded in some points the Fermi level μ. ϵ(k) $\cdot\, \Theta$ (dash line) has been then smooth out by a function f(ϵ, μ) (solid line) where f(ϵ, μ) is given by Eq. 1.68. (b) ϵ(k) $\cdot$ f(ϵ, μ) as a function of number of k-point, $\sigma = 0$ is equivalent to ϵ(k) $\cdot\, \Theta$

The Gaussian has been used first by Fu and Ho [35]. It turns out that the total energy is no longer minimal with respect to variations of $\mathrm{f_n}$ at the electronic ground state unless we replace the total energy E by a generalized free energy F [36][37],

$$\mathrm{F} = \mathrm{E} - \sum_{\mathrm{n}} \sigma \mathrm{S}(\mathrm{f_n}) \tag{1.69}$$

with the appropriate form for the entropy term $\mathrm{S(f_n)}$. For this Gaussian smearing the entropy is defined as [38]

$$\mathrm{S}(\frac{\epsilon_{\mathrm{n}} - \mu}{\sigma}) = \frac{1}{2\sqrt{\pi}} \ \mathrm{e}^{(-\frac{\epsilon_{\mathrm{n}}-\mu}{\sigma})^2} \tag{1.70}$$

It is not possible to express S as a function of f, because no analytical inversion of the error function exist, but in practice we are still able to calculate the entropy term from Eq. 1.70 since the eigenvalues ϵ_{n} are always available.

For the continuous density of states at the Fermi-level it can be shown that the free energy deviates quadratically with σ from $\mathrm{E}_{\sigma=0}$

$$\mathrm{F}(\sigma) \simeq \mathrm{E}_{\sigma=0} + \gamma\sigma^2 \tag{1.71}$$

Using $\mathrm{S}(\sigma) = -\frac{\mathrm{dF}(\sigma)}{\mathrm{d}\sigma}$ it is possible to obtain for the entropy S the equation

$$\mathrm{E}(\sigma) = \mathrm{F}(\sigma) + \sigma\mathrm{S}(\sigma) \ \simeq \ \mathrm{E}_{\sigma=0} - \gamma\sigma^2 \tag{1.72}$$

Then it is easy to show that

$$\mathrm{E}_{\sigma=0} \simeq \bar{\mathrm{E}}(\sigma) = \frac{1}{2}(\mathrm{F}(\sigma) + \mathrm{E}(\sigma)) \tag{1.73}$$

This method has two distinct shortcoming:

- Forces are usually defined as the derivatives of the variational quantity i.e. the free electronic energy F, therefore the forces cannot be used to obtain the equilibrium zero temperature or ground-state corresponding to an energy-minimum of $\bar{\mathrm{E}}(\sigma)$.
- The parameter σ has to be chosen with a great care. If σ is too large the energy $\bar{\mathrm{E}}(\sigma)$ will converge to the wrong value even for a infinite k-point mesh, and if σ is too small the convergence with the number of k-points will deteriorate.

These problems can be solved by adopting a slightly deferent functional form for $\mathrm{f}(\{\epsilon_{\mathrm{ik}}\})$, which was first proposed by Methfessel and Paxton (MP)[39] . Within this approach the integral of the Gaussian is only the first approximation (N=0) of the step function, further successive approximations (N=1,2,...) can be obtained easily.

In this method $\mathrm{S_n}$ is given by:

$$\mathrm{S_N(x)} = \frac{1}{2}\mathrm{A_N H_{2N}(x) e^{-x^2}} \tag{1.74}$$

and the partial occupancies are given by

$$\mathrm{f_0(x)} = \frac{1}{2}(1 - \mathrm{erf(x)}) \tag{1.75}$$

$$\mathrm{f_N(x) = f_0(x) + \sum_{m=1}^{N} A_m H_{2m-1}(x)\ e^{-x^2}} \tag{1.76}$$

with $\mathrm{x} = \frac{\epsilon-\mu}{\sigma}$. $\mathrm{H_m}$ is the Hermite polynomial of degree m, and explicit formulas for $\mathrm{A_m}$ can be found in ref [39].

In contrast to the Gaussian method the entropy term $\sum_{\mathrm{n}} \sigma \mathrm{S_N}((\epsilon_{\mathrm{n}} - \mu)/\sigma)$ will be very small for a reasonable choice of σ. Extrapolation to zero σ is usually not necessary, but in principal it might be done using

$$\mathrm{E}_{\sigma=0} \ \simeq \ \bar{\mathrm{E}}(\sigma) = \frac{1}{\mathrm{N}+2}\Big[(\mathrm{N}+1)\mathrm{F}(\sigma) + \mathrm{E}(\sigma)\Big] \tag{1.77}$$

where N is the order of the Methfessel and Paxton method.

1.4 Basics concepts

1.4.1 Adsorption energy

The adsorption energy per adsorbed atoms or molecule is defined as the difference of the total energy of the adsorbate system and the total energy of the separated clean substrate and the adsorbate atom or molecule. In the case of molecular adsorption i.e. CO adsorption, the adsorption energy $\mathrm{E_{ads}}$ is given by the following equation.

$$\mathrm{E_{ads} = E(M/S) - [E(S) + E(M)]} \tag{1.78}$$

where M stands for the molecular adsorbate and S the substrate and E is the total energy of the system. Please note that the negative value indicates an energy gain upon adsorption and positive values correspond to repulsion.

In the case of atomic adsorption i.e. hydrogen adsorption we usually refer the values to the free hydrogen molecule, therefore for the hydrogen adsorption there are two stages: At the first stage the hydrogen molecule dissociate with the following dissociation energy,

$$\mathrm{E_{diss} = 2E(H) - E(H_2)} \tag{1.79}$$

where E(H) is the energy of a single hydrogen atom in the gas phase and $\mathrm{E(H_2)}$ is the total energy of $\mathrm{H_2}$ molecule, thus $\mathrm{E_{diss}} > 0$ which means that this stage takes some energy from the system. The dissociated hydrogen atoms are then adsorbed by the substrate, which leads to the following gaining energy,

$$\mathrm{\Delta E = 2(E(H/S) - E(H))} \tag{1.80}$$

The adsorption energy per adsorbate is defined as the sum of dissociation and gain energies,

$$\mathrm{E_{ads} = \frac{\Delta E + E_{diss}}{n}} \tag{1.81}$$

where n = 2 is the number of adsorbate atoms. Substituting Eq. 1.79 and Eq. 1.80 into Eq. 1.81, we find the atomic adsorption energy with respect to the total energy of the free hydrogen molecule.

$$\mathrm{E_{ads} = E(H/S) - \left[E(S) + \frac{1}{2}E(H_2)\right]} \tag{1.82}$$

1.4.2 Density of states DOS and LDOS

The density of states (DOS), or total density of states, describes how many electronics states are located within an infinitesimally energy interval $d\epsilon$ around a given energy ϵ. This information is useful for a better understanding of the interaction between an adsorbate and a substrate. The DOS is defined as [40][41][42]:

$$\mathrm{g}(\epsilon) = \sum_{\mathrm{i}} \int_{\mathrm{k} \in 1^{\mathrm{st}}\mathrm{BZ}} \delta(\mathrm{E} - \epsilon_{\mathrm{ik}}) \tag{1.83}$$

In practice this is usually calculated from Kohn-Sham eigenvalues ϵ_{ik} from the weighted sum

$$\mathrm{g}(\epsilon) = \sum_{\mathrm{k}} \omega_{\mathrm{k}} \sum_{\mathrm{i}} \beta(\epsilon - \epsilon_{\mathrm{ik}}) \tag{1.84}$$

where β is a broadening function necessary due to the discreteness of the eigenvalues. In this work we have used a Methfessel-Paxton broadening to get a continuous distribution appropriate for a bulk material.

In a bond breaking or bond formation process, however, we are typically interested in what happens to the electronic orbitals of the directly involved orbitals of the molecule, therefore it is helpful to project the DOS into the orbital of interest atom. This local density of states (LDOS) or projected density of stated (PDOS) is then defined by [43]

$$\mathrm{g}_{l\mathrm{m,I}}(\epsilon) = \sum_{\mathrm{k}} \omega_{\mathrm{k}} \sum_{\mathrm{i}} \left| \left\langle \mathrm{Y}_{l\mathrm{m}}(\mathbf{r} - \mathbf{R}_{\mathrm{I}}) | \psi_{\mathrm{ik}}(\mathbf{r}) \right\rangle \right|^2 \beta(\epsilon - \epsilon_{\mathrm{ik}}) \tag{1.85}$$

where index l and i indicate the projected orbital and atom number respectively. The radial function needs to be cut off at a distance since its extent is very large and would otherwise over-lap the neighboring atoms, leading to artificial contribution to the density of states. The analysis of the local density of states is similar to the total density of states but it is now decomposed at each atom and to the angular momentum channels l and m.

1.4.3 d-band model

In order to analyze and understand chemical trends in adsorption, we utilize the d-band model as proposed by Hammer and Nørskov [44]. In this model, the interaction between an adsorbate and a transition metal is formally split into a contribution arising from the s and p states of the metal and a second contribution coming from the d-band.

The d-band $n_{l=2,m,I}(\epsilon)$ is defined as the density of states (DOS) projected onto one of the 5 localized d-orbital $(Y_{l=2,m=-2,-1,0,1,2})$ at site I at position R_I in Eq. 1.85. In a simplified expression, the whole d-band is assumed to act as a single electronic level located at ϵ_d which is chosen to be the center of the d-band and is given by[45]:

$$\epsilon_{d,I} = \frac{\sum_m \int_{-\infty}^{+\infty} \epsilon \; n_{l=2,m,I}(\epsilon) d\epsilon}{\sum_m \int_{-\infty}^{+\infty} \; n_{l=2,m,I}(\epsilon) d\epsilon} \tag{1.86}$$

where the sum extends over all d-band components of the metal substrate.

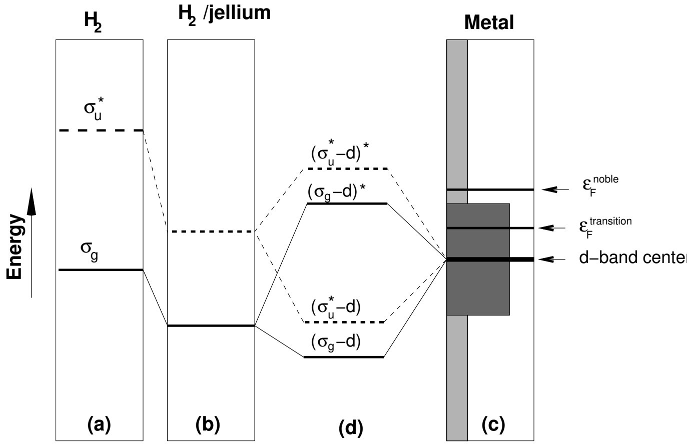

Figure 1.11: The interaction between H_2 and a metal substrate. (a) Bonding and anti-bonding states of H_2. (b) Interaction of H_2 molecule with sp-state of metal causing a down-shift of H_2 states. (c) The position of d-band center in a metal. $\epsilon_F^{transition}$ is the position of Fermi energy of the transition metal which is located below the $(\sigma_g - d)^*$. ϵ_F^{noble} is the position of Fermi energy of the noble metal. The light-gray shade indicates the broad sp-orbital of metal while dark-gray indicates the d-band orbital of the metal. (d) The hybridization of the adsorbate states due to the interaction with metal d-state

The interaction of the adsorbate with the sp-orbitals is assumed to lead to an down-shift of the adsorbate energy levels or the so-called renormalization at the adsorbate energy levels. The renormalized bonding and anti-bonding states for H_2 are shown in Fig. 1.11(b). This interaction gives rise to the a shift in the H_2 bonding (σ_g) and anti-bonding (σ_u^*) states. This first step thus yields a net energy gain. The renormalized adsorbate states are then coupled to the metals d-states. The interaction between the renormalized adsorbate states and the metal d-bands gives rise to a splitting in an bonding and antibonding contribution as it has been illustrated in Fig. 1.11(b)(c)(d). For both transition and noble metals the interaction between σ_g^* and d-state is always attractive since the anti-bonding $(\sigma_u^* - d)^*$ state will always be above the Fermi level as it has been shown in Fig. 1.11(c)(d). For transition metals, the Fermi level is located above the $(\sigma_g - d)^*$ state, therefore the σ_g interaction is also attractive in addition to the σ_u^*. For noble metals however the antibonding $(\sigma_g - d)^*$ resonance is shifted below the Fermi energy and becomes occupied leading to a repulsive interaction arising from the orthogonalization of the overlapping molecular and metal states. If the coupling to the metal sp sites can be considered to be similar for a group of surfaces, trends in adsorption energies will depend primarily on the coupling to the metal d-states, which then depends mainly on three factors: (i) the center ϵ_d of the d-bands, (ii) the degree of valence d-orbital filling f_d and (iii) the coupling matrix element V between the adsorbate states and the metal d-state. If the coupling is weak ($|\mathrm{V}| \ll |\epsilon_\mathrm{d} - \epsilon_\mathrm{a}|$) where ϵ_a is the adsorbate level, Hammer and Nørskov [44] suggested that the interaction energy ΔE due to the adsorbate interaction with the d-band of the metal can be estimated as:

$$\Delta\mathrm{E} = -2\frac{\mathrm{V}^2}{\epsilon_{\sigma_\mathrm{u}^*} - \epsilon_\mathrm{d}} - 2(1-f)\frac{\mathrm{V}^2}{\epsilon_\mathrm{d} - \epsilon_{\sigma_\mathrm{g}}} + \alpha\mathrm{V}^2 \tag{1.87}$$

Here the first term describes the energy gain due to the hybridization between the σ_u^* and the d-states. The second term is the corresponding $(\sigma_\mathrm{g} - \mathrm{d})$ interaction. The factor (1-f) describes the empty states in the d-orbital and the last term is the repulsive term due to the orthogonalization of both σ_u^* and σ_g states to the metal d-states. V is the d-band coupling matrix element between adsorbate and the surface metal atom and it is related to the distance between adsorbate and surface atoms as follows [46][47].

$$\mathrm{V}^2 \propto \sum_\mathrm{i} \frac{1}{|\mathbf{r} - \mathbf{R}_\mathrm{i}|^6} \tag{1.88}$$

where r is the position of the adsorbate and $\mathrm{R_I}$ is the position of the i-th metal atom.

In the case of hydrogen atomic adsorption on metal, since there is no anti-bonding σ_u^* state, the first term of Eq. 1.87 vanishes and $\epsilon_{\sigma_\mathrm{g}}$ is replaced by ϵ_H, the renormalized adsorbate resonance. The chemisorption energy difference $\Delta\mathrm{E}_\mathrm{chem}$ for one H due to the coupling to the d-bands is given by [44]:

$$\Delta\mathrm{E}_\mathrm{chem} = -2(1-f)\frac{\mathrm{V}^2}{\epsilon_\mathrm{d} - \epsilon_\mathrm{H}} + \alpha_\mathrm{chem}\mathrm{V}^2 \tag{1.89}$$

This equation shows that for noble metals where the d-orbital is fully filled the first term of Eq. 1.89 vanishes and only the repulsive term will remain, therefore the interaction between atomic hydrogen and noble metal d-states is repulsive [48]. Please note that the interaction between adsorbate and sp-states of the metal is attractive and it can overcompensates the repulsive term of Eq. 1.89 and therefore the net interaction between adsorbate and a noble metal can be attractive.

Later on the Eq. 1.87 was modified by Pallassana *et.al* [49]. They showed that small shifts in the position of the d-band center of the metal $\delta\epsilon_\mathrm{d}$ are linearly correlated to changes in the chemisorption energies.

$$\Delta\mathrm{E}_\mathrm{chem} = \frac{\mathrm{V}^2}{(\Delta\epsilon)^2}\,\delta\epsilon_\mathrm{d} \tag{1.90}$$

Where $\Delta\epsilon = |\epsilon_d - \epsilon_a|$, ϵ_d and ϵ_a are the location of the *d*-band center and the H 1s orbital state respectively. $\Delta\epsilon_d$ is the shift of the position of the *d*-band center and V is the *d*-band coupling matrix element between adsorbate and the surface metal atom defined by Eq. 1.88.

1.4.4 Induced charge density

The charge transfer in a system upon a change in the atomic configuration can be described using charge density differences. The charge here comprises extraction or inclusion of atoms or molecules. The positions of the corresponding atoms in different calculation have to be the same, i.e. once we calculate the charge density of slab with the adsorbate, the position of the slab atoms and the adsorbate alone in the further charge density calculation must be the same. Generally the system we are interested in is an adsorbate on a surface, thus the charge difference is given by the charge density of the interacting minus the charge density of the non-interacting system at the same position.

$$\Delta \mathrm{n} = \mathrm{n}^{\mathrm{A/S}}(\mathrm{A/S}) - \mathrm{n}^{\mathrm{A/S}}(\mathrm{S}) - \mathrm{n}^{\mathrm{A/S}}(\mathrm{A}) \tag{1.91}$$

where

- $\mathrm{n}^{\mathrm{A/S}}(\mathrm{A/S})$ is the system with the adsorbate A on the substrate S, and the atoms have been relaxed.
- $\mathrm{n}^{\mathrm{A/S}}(\mathrm{S})$ is the system with only the substrate S, but the coordinates of the substrate atoms have been taken from the calculation with the adsorbate: thus the super-script A/S.
- $\mathrm{n}^{\mathrm{A/S}}(\mathrm{A})$ is the system with only the adsorbate A, but the coordinates of the adsorbate atoms have been taken from the calculation with the adsorbate on the surface: thus the super-script A/S.

The charge density difference plot is perhaps the most directly available quantity for any analysis of the chemical interactions. The formation of bonding and anti bonding levels will be directly reflected in the electron density as an accumulation or depletion of electrons. As an example Fig. 1.12 shows a distinct charge accumulation between carbon and oxygen in the CO molecule due to the interaction between σ and π orbitals of carbon and oxygen.

1.4.5 Blyholder model for adsorption of CO

In 1964 George Blyholder [50] introduced a model according to which the bonding of CO onto surfaces happens via the emptying of the 5σ orbital and filling of the $2\pi^*$ orbitals as shown in Fig. 1.13. Please note that the highest occupied and lowest unoccupied molecular orbitals of CO are 5σ and $2\pi^*$ respectively. Fig. 1.12 shows the position of the molecular orbitals of CO. The interaction of CO with s and p orbitals of a metal is weak, therefore we expect that the CO is only weakly bound on the surfaces of i.e. aluminum or noble metals with their filled d-bands. The interaction of CO with transition metals is however strong due to its interaction with the open shell d-band of the transition metal. The adsorption site for CO depends on the nature of the d hybrids. On-top the 5σ orbital overlaps with the $\mathrm{d}_{\mathrm{z}^2}$ like states and the back-bonding occurs via the $\mathrm{d}_{\mathrm{xz,yz}}$ orbitals, whereas on the three-fold and bridge site, this is vice

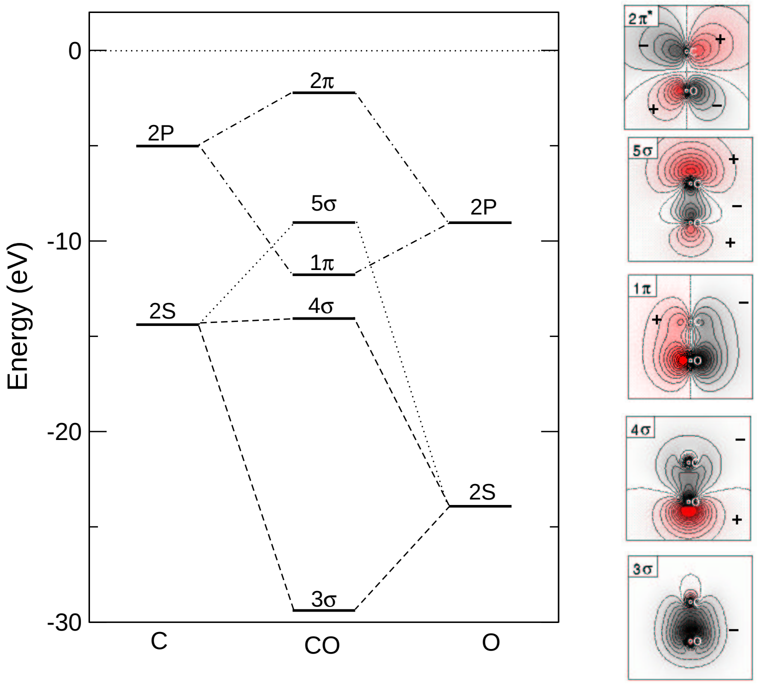

Figure 1.12: The significant Kohn-Sham single particle states of CO. Right are the Kohn-Sham energy levels of the orbitals from our DFT calculation employing the GGA approximation.

versa. In Fig. 1.13 the interaction mechanism of CO with a metal surface is illustrated. There is a charge transfer from 5σ of CO to d_{z^2} (blue) and from $d_{xz,yz}$ to 1π of CO molecule (red). We found that the Kohn-Sham energy level of the orbital with mainly 5σ character moves below the level of the 1π orbital, thus making the 5σ no longer the highest occupied "molecular" orbital, however the 1π does not take part in the bonding as its overlap is small with the substrate states. The main features of the CO adsorption are still described well by the Blyholder model.

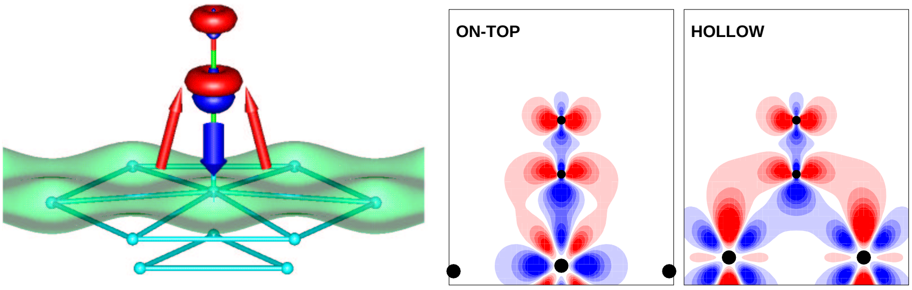

Figure 1.13: The Blyholder mechanism: The 5σ orbital and the 2π^* filled in the formation of hybrids with the substrate. Right is the interaction mechanism with the different d like states on the on-top and hollow adsorption sites.

Chapter 2

Adsorption on Pd overlayer deposited on noble metals

The catalytic properties of thin metal overlayers deposited on a foreign substrate can be significantly modified with respect to those of the bulk metal [51]. Therefore a detailed understanding of the underlying microscopic mechanisms responsible for the modification of the reactivity in bimetallic systems is highly desirable. It might lead to the design of better catalysts in both heterogeneous and electro-catalysis [52, 53], in particular since bimetallic systems might offer the possibility to tailor the reactivity by preparing specific surface compositions and structures.

In electrochemistry, Pd overlayers deposited on Au single crystal surfaces have been studied in detail as a well-defined model system [54–56]. One of the first experimental study of ultrathin film of Pd on Au(111) and Au(100) has been done by Paffett *et.al.* [57]. They found that in vacuum the growth mode of ultrathin films of Pd on Au(111) depends strongly on the substrate deposition temperature. The growth mode of vapor-deposited Pd films on Au(111) at 150 K is described well by an epitaxial layer-by-layer mechanism for the first few layers. Kibler *et.al.* [58] and Kondo *et.al.* [59] have shown that in electrochemical conditions the growth mode including possible alloy formation apparently depends on the preparation conditions. The difference in the growth modes between electrochemical and vacuum conditions has been related to the surface structure of the Au(111) surface [54]. In vacuum, Au(111) shows a complex $(23 \times \sqrt{3})$ herringbone reconstruction [60] and Au(100) shows a hexagonally close-packed structure [61]. These reconstructions are lifted under electrochemical conditions at the positive potentials at which Pd deposition occurs [58]. In another experimental study, Kolb *et.al.* [62] and Liu *et.al.* [63] found out that due to the relatively small lattice mismatch between Pd and Au of 5%, Pd overlayers with thickness up to at least 5 monolayers grows pseudomorphically on Au(100) and up to four Pd layers on Au(111) under electrochemical conditions. They used in-situ STM and cyclic voltammetry to investigate the electrochemical desorption of Pd onto Au(111) from chloride-containing solutions. They found out that the deposition of the first Pd monolayer onto Au(111) starts at underpotentials. The Pd desorption starts by forming a pseudomorphic layer in the underpotential region, followed by the formation of the second Pd monolayer of overpotentials. The first two layers grow layer by layer, the second starting when first has been completed.

Another experiment on Pd films vapor deposited on Au(111) has been done by A. Sellidj and B. Koel [64]. They used Ultraviolet Photoemission Spectroscopy (UPS) to determine the electric and CO chemisorption properties of ultrathin Pd films on Au(111). They found out that the Pd density of states sharpens and shifts closer to the Fermi level. Baldauf and Kolb [65] used formic acid oxidation on Pd overlayers on Au(hkl) to estimate the catalytic reactivity. They have shown that the electrocatalytic properties of the Pd overlayers depend markedly on their thickness and on their crystallographic orientation. The similar results have been obtained by Naohara *et.al.* [66].

In order to understand the catalytic activity of overlayer systems, two effects have to be taken into account. In addition to the direct electronic interaction of the pseudomorphic overlayers with the metal substrate, geometric strain effects due to the lattice mismatch can change the reactivity of thin films [67–70]. Although there has been a significant progress in the detailed experimental characterization of electrode surfaces and reactions at electrochemical interfaces [71], still it is not trivial to disentangle these effects in the experiment. In such a case, total energy calculations based on first-principles electronic structure theory can be very helpful. In recent years they have become an efficient and reliable tool to obtain qualitative and often even quantitative insights into the structure and chemistry of surfaces [72–75].

The outline of this chapter is as following. In section 2.1 we have performed periodic density functional theory (DFT) calculations of thin pseudomorphic Pd overlayers on the Au(111) and Au(100) single crystal surfaces in order to contribute to the understanding of the modified reactivity of overlayer systems. In section 2.2 we have calculated the adsorption energies of the atomic hydrogen and CO on the various adsorption sites as a microscopic probe of the local reactivity. Although it has been found that the H adsorption process is strongly influenced by the anion of the supporting electrolyte [76], as a first step we have addressed the interaction of hydrogen and CO with Pd overlayers of Au in the absence of any electrolyte. This is the usual approach in the *ab initio* treatment of molecule-surface interactions of electrochemical interest [77] due to the difficulties of realistically incorporating any electrolyte in electronic structure calculations. Despite this, in chapter 3 we have also performed calculations for the hydrogen adsorption on one Pd overlayer on Au under the presence of a thin film of water [78]. These calculations indicate that the presence of water weakens the interaction between the metal and the adsorbate, but only by less than 100 meV. Similar results have already been obtained in a DFT study of the deprotonation of acetic acid over Pd(111) in the presence of water molecules [79]. The strain effects on pure Pd and the substrate interaction effects will be discussed in section 2.3.2. The hydrogen coverage effects for $\theta = 1$ and $\theta = 0.5$ will be discussed in section 2.3.4. In section 2.4 we have replaced the substrate Au with Cu and performed a total energy calculation on Pd overlayer on Cu(111) in order to understand more about strain and substrate interaction effects. The lattice constant of Cu is smaller than the lattice constant of the Pd. In contrast to the Pd-Au interaction, these calculations show that the Pd-Cu interaction is higher than the Pd-Pd. Therefore both, compressed lattice constant and substrate interaction lead to a lower surface adsorption energy. In order to have a completed reference, the reactivity of Cu/Pd(111) has been also studied in section 2.4.

2.1 Pd/Au: Computational method and overlayer structure

Self-consistent periodic DFT calculation has been performed using the Vienna ab initio simulation package (VASP) [80–82]. The exchange-correlation energy effects have been described within the generalized gradient approximation (GGA) using Perdew-Wang (PW-91) functional (see section 1.2.2). The ionic cores are represented by ultrasoft pseudopotentials (see section 1.3.4). As outline in chapter 1, the Kohn-Sham one-electron valence states are expanded in a basis of plane waves with the cutoff energy of 200 eV for hydrogen adsorption and 400 eV for CO adsorption. These values are sufficient in order to obtain converged results. A Methfessel-Paxton smearing (see section 1.3.5) of σ=0.2 eV has been used in order to get a faster convergence of the electronic structure calculations. The first step of any surface calculation is to determine the structural properties of the bulk crystal self-consistently i.e. the equilibrium lattice constant. The structural properties of the bulk Pd and Au were determined by fitting the Murnaghan equation of state [83][84] to the computed total energies per primitive unit cell and it has been listed in Table 2.1. The calculated equilibrium lattice constants for bulk Pd and Au are a=3.96 Å and a=4.18 Å, respectively, which are in good agreement with the experiment (3.88 and 4.08 Å [85], respectively).

	Pd			Au		
	lattice const.(Å)	B_0 (GPa)	E_{cohen} (eV)	lattice const.(Å)	B_0 (GPa)	E_{cohen} (eV)
Theory	3.96	161	5.19	4.18	133	3.20
Exp.	3.88	181	3.89	4.08	270	3.81

Table 2.1: Lattice constant, bulk modulus and cohesive energy of Pd and Au

The Pd/Au overlayer structures are modeled by a slab of five layers of Au on which up to three Pd overlayers have been deposited. All layer structures are separated by 14 Å of vacuum. The three bottom layers of the slabs have been kept fixed at their corresponding bulk positions, while all upper layers including the overlayers have been fully relaxed. The surface Brillouin zone is sampled by a Monkhorst-Pack **k**-point set (please see section 1.3.2) of 7×7×1 (17×17×1) for a 2×2 (1×1) surface unit cell, corresponding to 8 (45) **k**-point in the irreducible Brillouin zone. For the analysis of the electronic structure of the (2×2) surface unit cell, we used a finer mesh of 11×11×1 **k**-points, corresponding to 16 **k**-points in the irreducible Brillouin zone. In Table 2.2 the calculated layer relaxations are shown for up to three Pd overlayer on Au(111) and Au(100). For pure Au and Pd the relaxation is less than 0.5% while for Pd overlayer

interlayer	surface(111)					
distance	Au	Pd/Au	2Pd/Au	3Pd/Au	Pd@Au	Pd
d_{12} [Å]	2.44(1)	2.26(-6)	2.19(-9)	2.18(-9)	2.16(-10)	2.30(0)
d_{23} [Å]	2.40(0)	2.41(0)	2.26(-6)	2.17(-10)	2.13(-12)	2.28(0)
d_{34} [Å]	2.41(0)	2.40(0)	2.42(0)	2.28(-6)	2.41(0)	2.29(0)
interlayer	surface(100)					
distance	Au	Pd/Au	2Pd/Au	3Pd/Au	Pd@Au	Pd
d_{12} [Å]	2.07(-1)	1.90(-10)	1.80(-14)	1.78(-15)	1.77(-15)	1.95(-2)
d_{23} [Å]	2.10(0)	2.07(-1)	1.94(-7)	1.81(-13)	1.76(-16)	1.98(0)
d_{34} [Å]	2.10(0)	2.08(0)	2.09(0)	1.94(-7)	2.10(0)	1.98(0)

Table 2.2: Layer relaxation of the Pd/Au(111) and Pd/Au(100) overlayer. The DFT-GGA relaxations were computed for the pure Au, one, two, three Pd overlayer on Au and pure Pd. The pure Pd substrates with lateral lattice constant of Au (a=4.18 Å) and Pd (a=3.96 Å) are labeled by Pd@Au and Pd respectively. The relative change to the bulk interlayer distance (in %) is given in parentheses. Positive numbers correspond to a surface expansion away from the bulk substrate.

due to the larger lateral lattice constant, the relaxation for Pd atoms are up to -15%. Table 2.1 also shows a higher layer relaxation for (100) surface due to the fact that (100) surface is less densely packed. Furthermore, we have done a slab calculation on pure Pd slabs where the lateral lattice constant have been kept fixed to the bulk Au lattice constant. The results obtained for the pure Pd surface expanded to the Au lattice constant are denoted by Pd@Au. They correspond to the hypothetical system of infinitely many Pd overlayers grown pseudomorphically on Au.

In our electronic structure calculations, we cannot treat the herringbone reconstruction of Au(111) due to computational constraints. Still we have tried to address the growth mode of Pd/Au by calculating the adsorption energy of a Pd atom on Pd(111) and unreconstructed Au(111) in a (3×3) surface unit cell corresponding to a coverage of 1/9 in order to avoid any interaction between the adatoms. We found that the Pd adatom is by 0.103 eV less strongly bound to Au than to Pd. Hence the Pd-Pd interaction is stronger than the Pd-Au interaction which explains the fact that Pd films grow in a rough fashion on Au(111) in vacuum. These finding are in fact at variance with the experimental observation at a Pd underpotential deposition (ups) layers on Au. However, the difference of 0.1 eV in the interaction energies is relatively small compared to the cohesive energies of Pd (3.89 eV/atom) and Au (3.81 eV/atom)reported in Table 2.1. It is therefore reasonable to assume that the Pd-Au interaction is modified to a certain extent by the presence of the electrolyte or the adsorption of anions which could reverse the order of the interaction strength. This suggests that it is not the lifting of the Au(111) reconstruction under electrochemical conditions that leads to the layer-by-layer growth of the Pd films but rather the modified Pd-Au interaction strength. It should be further noted that Takahasi *et al.* [54] and Naohara *et al.* [66] do not report any underpotential deposition of Pd on Au.

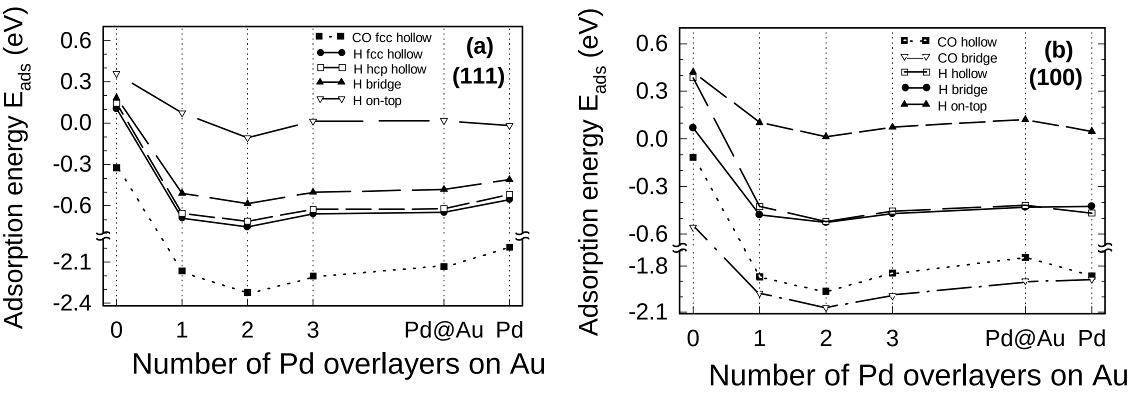

Figure 2.1: CO and hydrogen adsorption energies as a function of the number of Pd overlayers on Au for different adsorption sites on the (111) **(a)** and the (100) surface **(b)** at a coverage of $\theta = 0.25$. The pure Pd substrates with the lateral lattice constant of Au ($a = 4.18$ Å) and Pd ($a = 3.96$ Å) are labeled by Pd@Au and Pd, respectively.

2.2 Adsorption energies on Pd/Au overlayers

In Fig. 2.1 we have plotted the calculated adsorption energies of atomic hydrogen and CO on the high-symmetry adsorption sites as a function of the number of Pd overlayers on Au(111) and Au(100). The hydrogen and CO adsorption energies were calculated via Eq. 1.82 and Eq. 1.78 respectively. The binding energies of hydrogen and CO in the gas phase were calculated to be 4.55 eV and 11.43 eV respectively. A (2×2) super cell was chosen with coverage θ=0.25 which is sufficiently small in order to avoid any significant interaction between the adsorbates. We have also calculated the hydrogen and CO adsorption energies for the fcc site on one Pd monolayer on a Au(111) ($\sqrt{3}\times\sqrt{3}$) super cell and compared them with those in a (2×2) super cell. The difference in the adsorption energies is 3 meV(0.4%) and 0.143 eV (6.5%) for hydrogen and CO respectively. Hence in order to minimize the CO-CO interaction, choosing a (2×2) super cell is necessary. The results obtained for the pure Pd surface expanded to the Au lattice constant are denoted by Pd@Au. By comparing the results of Pd@Au with those for a finite number of Pd overlayers and those for a pure Pd slab with the intrinsic Pd lattice constant, geometrical strain effects can be discriminated from electronic interaction effects with the substrate. Note that the identification of adsorption energies with the reactivity should be done with caution. High catalytic activity usually is the consequence of a compromise between a sufficiently strong interaction in order to lead to, e.g., lower dissociation barriers than in the gas phase with a relatively modest binding strength of the products so that they can desorb again. Still, the interaction strength of molecules with surfaces is often closely correlated with the reactivity for a large class of catalytic reactions, for example via a Brønsted-Evans-Polanyi-type relation [86].

The first striking result evident in Fig. 2.1 is that CO and H show the same trends in the adsorption energies as a function of the number of Pd overlayers and of the lattice strain despite their different electronic structure and bonding mechanism. The binding energies of both adsorbates on thin Pd/Au overlayers are larger by up to 0.2–0.3 eV than on pure Pd substrates and show their maximum on two Pd overlayers at all considered adsorption sites. At the most densely packed (111) surface, the adsorption energies on three Pd overlayers hardly differ from those on the pure expanded Pd slabs. This means that the electronic effects of the underlying Au substrate only contribute significantly to the reactivity of the first two overlayers. The modified reactivity of the third layer is almost entirely dominated by the geometric effect due to the lattice expansion. For the less densely packed (100) surface, there is still some influence of the Au support up to the third Pd overlayer. This can be understood from the fact that the (100) layers have a smaller spacing than the (111) layers. According to Table 2.2 the intermediate distances in (111) surface is 2.41 Å while in (100) surface is 2.10 Å. Furthermore a relatively larger Pd relaxation on the first layer of (100) surface along the surface normal and toward the bulk due to the lattice expansion can also contribute to a smaller spacing.

As far as the pure strain effects are concerned, we do not find an unique trend. On the Pd(111) surface the binding energies increase upon lattice expansion at the higher-coordinated sites while the top site shows the opposite trend. On the Pd(100) surface, on the other hand, both the fourfold hollow as well as the top site exhibit a weaker binding upon lattice expansion whereas at the bridge site there is a slight increase in the binding strength.

In Fig. 2.1, we have also calculated the CO and H adsorption energies on Au(111) and Au(100). Note that we did not consider the surface reconstructions of neither Au(111) nor Au(100). Our results confirm the inertness of the Au substrate, i.e. all binding energies are greatly reduced on Au compared to clean Pd and the Pd/Au overlayers.

2.3 Discussion

2.3.1 Electronics structure

According to Eq. 1.90, an upshift of the *d*-band center is associated with a stronger interaction. A lattice expansion or a reduced coordination leads to a smaller *d*-bandwidth and, if the *d*-band is more than half-filled, to an upshift of the *d*-band due to charge conservation (see section 1.4.3) [69, 87]. This effect explains for example the higher reactivity of step edge atoms [45, 88–91] or expanded surfaces [69].

In Fig. 2.2 the position of the *d*-band center is plotted as a function of the number of Pd overlayers on Au(111) and Au(100) for the uppermost and the subsurface layer. In general, the (111) and (100) surfaces show rather similar trends. Comparing the data for pure Pd and Pd@Au, it is obvious that expanding the Pd substrate to the Au lattice constant leads to an upshift of the local *d*-band center at the surface, which is as expected. Interestingly enough, on Pd(100) the *d*-band center of the subsurface layer shifts down in energy upon lattice expansion. This is a consequence of the relaxation along the surface normal. Upon lateral expansion, the interlayer spacing decreases, and consequently, the coupling between the layers becomes stronger. For the more open (100) surface this effect even overcompensates the weaker intra-layer coupling. This

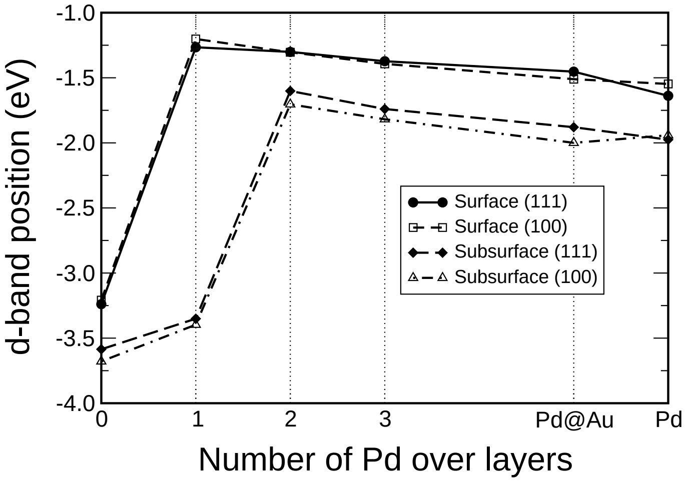

Figure 2.2: Position of the local center of the *d*-band with respect to the Fermi energy as a function of the number of Pd overlayers on Au(111) and on Au(100) for the surface and the subsurface layer. The results for a pure Pd substrate with the lateral lattice constant of Au ($a = 4.18$ Å) and Pd ($a = 3.96$ Å) are labeled by Pd@Au and Pd, respectively.

effect is less pronounced in (111) surface where the Pd relaxation is less and it can only partially compensative the *d*-band effect (see Table 2.2). However, in addition to these geometric effects, the electronic interaction of Pd with the underlying Au substrate leads to a further upshift of the Pd *d*-band. In the following, we will first address the effects induced by pure lattice strain, then focus on the substrate interaction and finally discuss coverage effects.

2.3.2 Lattice strain effects

Since CO and hydrogen show the same trends in the adsorption energies, we will mainly concentrate on hydrogen adsorption in our analysis of the electronic factors determining the reactivity in the following. The interaction of hydrogen with Pd is well-studied, in particular under vacuum conditions [92–96]. For the unstrained pure Pd surfaces, our results are in agreement with previous calculations, both with respect to hydrogen adsorption [97–99] as well as to CO adsorption [100, 101]. Nørskov and *et al.*[69] have performed a DFT calculation on O and CO adsorption on Ru(0001). They found an adsorption energy increasing with lattice expansion for O and CO adsorption energies and a decreasing on CO dissociation barrier which is in agreement with experiment [67, 68]. However in our calculation we do not obtain a unique trend of the adsorption energies as a function of the lattice expansion. The bonding energies increase at the threefold hollow and the bridge position on the Pd(111) but, they decrease at the top position of both the (100) and (111) surface and at the fourfold hollow position of Pd(100). This non-uniform behavior is at variance with the statements of the *d*-band model, which would predict an increase in the adsorption energies at all sites due to the *d*-band center upshift upon lattice expansion.

For the fourfold hollow site of the (100) surface, this unexpected behavior could be due to extension of the adsorbate-substrate bond upon lattice expansion which would lead to a weaker interaction. In Table 2.3 we have listed the adsorption heights and distances to the nearest Pd atoms for all considered hydrogen adsorption site at the unstrained and strained surfaces. Upon expanding the lateral lattice constant of the Pd(111) surface by 5%, the hydrogen adsorption height at the bridge site is reduced from 0.97 Å to 0.86 Å and from 0.81 Å to 0.61 Å at the three-fold fcc hollow position. This process is illustrated in Fig. 2.3. d and $d^{'}$ are the bond length before and after the expansion, respectively. The downward relaxation of the hydrogen atoms occurs in such a way that the H-Pd distances to the nearest neighbors are kept constant within ±0.01 Å. We have found the same effect for CO adsorption on Pd(111), where the adsorption height at the fcc hollow position is reduced from 1.30 Å to 1.19 Å, thus keeping the C-Pd distances to the nearest neighbors of d=2.08 Å constant.

This mechanism can not work any longer at the fourfold hollow position of the (100) surface. There the hydrogen atom sits already rather deep in the first Pd surface layer only 0.32 Å higher than the Pd atoms. Hence it is also directly interacting with the subsurface layer so that it becomes effectively fivefold coordinated. Although the hydrogen atom reduces its height to 0.14 Å upon the lattice expansion and the neighboring Pd atoms also relax towards the hydrogen atom, still the H-Pd bond length increases from 1.99 Å to 2.06 Å. The reduced H-Pd interaction and the energetic cost of the Pd atom relaxations overcompensate the increase in the reactivity of the expanded surface due to the d-band center upshift. As a result, the fourfold hollow and the bridge site become energetically degenerate.

In the case of CO adsorption at the hollow site, we see a qualitatively similar behavior: upon lattice expansion, CO distance to the subsurface Pd atom reduces from 3.10 Å to 2.92 Å. Our LDOS confirms that there is a direct interaction with subsurface atom which is increased upon lattice expansion. This effectively higher coordination is energetically unfavorable for CO resulting in a weaker binding. Furthermore in order to keep the CO distance with Pd in the subsurface as far as possible upon the expansion a contraction of 4 the nearest Pd atoms to CO atoms along x and y direction has been seen. This contraction is increased from 0.05 Å to 0.15 Å upon lattice expansion and it is energetically unfavorable.

The hydrogen adsorption energies on the on-top positions of Pd(100) and Pd(111) also show the opposite trend upon lattice expansion than expected from the d-band shift. However, here the adsorption height which at this site is the same as the nearest-neighbor distance to the adjacent Pd atom remains basically unchanged upon lattice expansion: d=1.56 Å and d=1.88 Å for hydrogen and CO respectively. Hence bond length effects can not be the source for the unexpected trend in the adsorption energies as a function of lattice strain.

It is important to note that at the top site the hydrogen atom is mainly interacting with the Pd atom directly beneath. Furthermore, the hydrogen 1s state only couples to the Pd $d_{3z^2-r^2}$ orbital since all other d orbitals are not rotationally symmetric with respect to the Pd-H bond along the z-axis. This means that the H atom at the top site is much more strongly interacting with the single Pd $d_{3z^2-r^2}$ orbital compared to the interaction of the H atom with the Pd d orbitals at the higher coordinated site. Fig. 2.4(a) and (b) show the H-adsorption induced LDOS at the fcc and on-top sites

	Pd(111)						
lattice	fcc hollow		hcp hollow		bridge		top
constant	h	$d_{\mathrm{Pd-H}}$	h	$d_{\mathrm{Pd-H}}$	h	$d_{\mathrm{Pd-H}}$	$h = d_{\mathrm{Pd-H}}$
3.96	0.81	1.83	0.73	1.82	0.97	1.73	1.56
4.18	0.61	1.83	0.58	1.83	0.86	1.73	1.56
	Pd(100)						
			fourfold hollow		bridge		top
			h	$d_{\mathrm{Pd-H}}$	h	$d_{\mathrm{Pd-H}}$	$h = d_{\mathrm{Pd-H}}$
3.96			0.32	1.99	0.99	1.72	1.56
4.18			0.14	2.06	0.88	1.72	1.55

Table 2.3: Atomic hydrogen adsorption height h and nearest-neighbor distance d_{Pd-H} between hydrogen and Pd on various high-symmetry adsorption sites on Pd(111) and Pd(100) as a function of the lattice strain. All distances are given in Å.

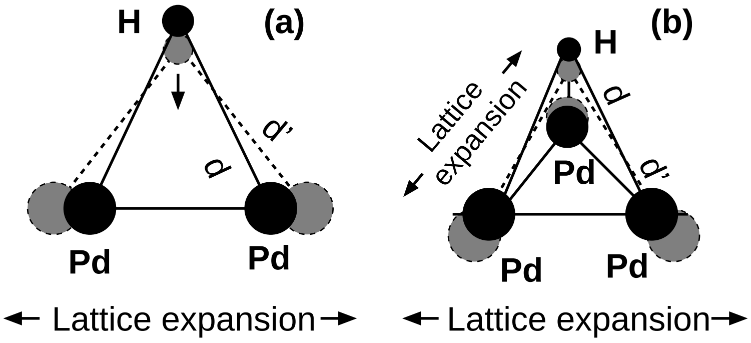

Figure 2.3: Schematic sketch of the change of the H adsorbate height upon lattice expansion. (a) bridge site, (b) threefold hollow site. Upon lattice expansion the hydrogen atoms relax towards the surface so that the optimum H-Pd distance d is kept constant.

respectively. While at the fcc site the Pd d-band LDOS is hardly changed by the presence of the adsorbed hydrogen atom, at the top site there is strong hybridization between the H 1s-derived state and the Pd $d_{3z^2-r^2}$ orbital. For unstrained Pd, the hydrogen induced downshift of the Pd d-band center are 0.19 eV and 0.66 eV for fcc hollow site and a top site respectively.

Fig. 2.4c shows the LDOS for hydrogen adsorption on the top site of the *expanded* Pd(111) surface. As far as clean Pd(111) is concerned, it is obvious that the local d-band is narrower and its center higher than on the unstrained surface which should make it more reactive according to the d-band model. The upshift of clean Pd d-band center due to the strain effect is 0.17 eV. However, the hydrogen induced downshift of the Pd d-band at the strained surface is 0.56 eV which is larger by 0.10 eV compared to the expanded surface, as can already be inferred from a careful inspection of Fig. 2.4b and c. The larger hydrogen induced d-band downshift at the unstrained surface overcompensates the effect of the higher d-band center at the expanded surface and thus stabilizes the adsorption at the unstrained surface. This analysis shows that the d-band model is only appropriate if the interaction between adsorbate and sub-

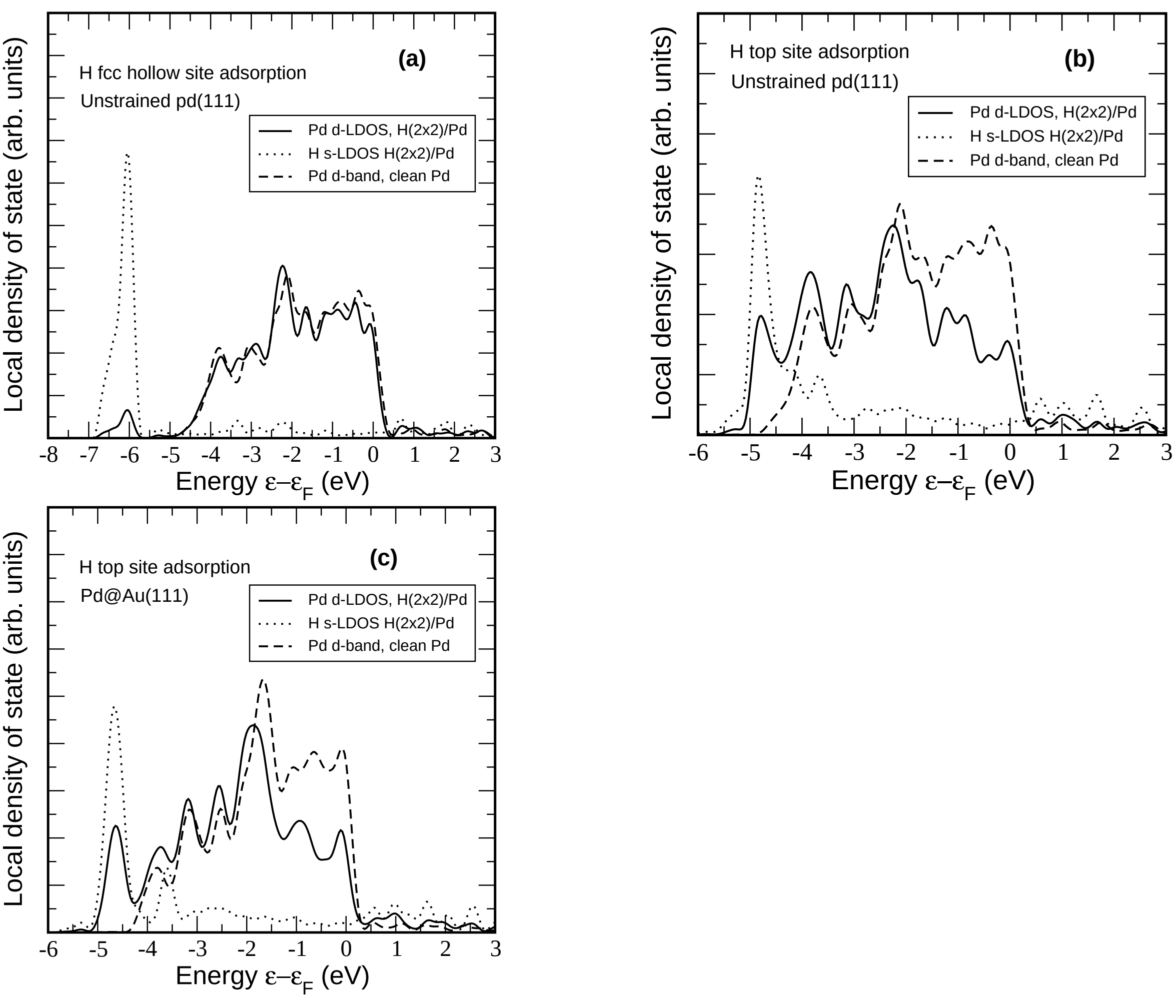

Figure 2.4: Local density of states (LDOS) of the hydrogen 1*s* state and the Pd *d*-band for atomic hydrogen adsorption on unstrained Pd(111) at the fcc hollow site (a) and the top site (b) and at top site of strained Pd(111) (c). The hydrogen 1s density of state is multiplied by a factor of 5. The energies are given with respect to the Fermi energy ε_F.

strate is not too strong [102]. If there is a strong coupling, then the response of the local *d*-band to the presence of the adsorbate has to be taken into account in addition to the d-band position in order to understand the reactivity. An equivalent behavior has also been observed in the hydrogen adsorption energy on pure Cu(111) [103] (see also section 2.5).

2.3.3 Substrate interaction effects

The interaction of Pd with the Au substrate leads to a further upshift of the local *d*-band center of the Pd overlayers in both (111) and (100) surfaces, as shown in Fig. 2.2. In order to understand the reasons for the upshift, we have plotted in Fig. 2.5 the local *d*-band density of state for one Pd atom adsorbed per 3×3 surface unit cell on Au(111). As already mentioned, Pd atoms are by 0.103 eV less strongly bound to Au than to

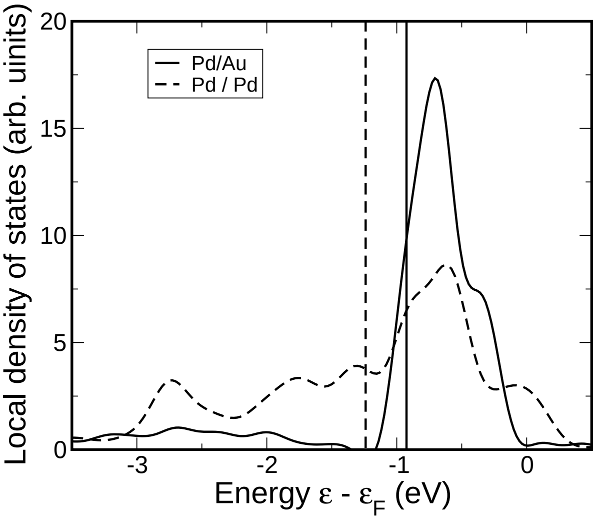

Figure 2.5: Local d-band density of state (LDOS) for one Pd atom adsorbed per 3×3 surface unit cell on Au(111) and Pd(111) as a function of the energy. The vertical lines indicate the position of the d-band centers. On Au(111), the d-band LDOS of the Pd atom is much narrower and higher in energy than on Pd(111).

Pd. This difference is not too large with respect to the cohesive energies of Pd and Au. However, the difference in the local d-band density of state of the Pd atom adsorbed on both surfaces is quite significant.

Au has a deep-lying filled d-band which makes it to an inert noble metal [48]. The d-band center of Au(111) is d=-3.42 eV, much lower than the pure Pd(111) result d=-1.87 eV And indeed, on Au(111) the d-band LDOS of the Pd atom is much narrower and higher in energy than on Pd(111), as Fig. 2.5 shows. This reflects that there is only a weak coupling between the Pd and the Au d electrons. Thus, the attraction between Pd and Au is mainly mediated by the sp electrons. It also explains the further upshift of the d-band center for the Pd overlayers on Au (see Fig. 2.2) which contributes to the higher reactivity of the overlayer systems. The d-band center of Pd atom on Au substrate is d=-0.93 eV while on Pd substrate is d=-1.24 eV. This shift as it has been shown in Fig. 2.2 contributes also to the higher reactivity of the overlayer systems.

On the basis of our findings we thus propose that depositing a reactive metal on an inert metal with a larger lattice constant and weaker metal-metal binding bond should in general lead to a higher reactivity of the overlayer since both substrate interaction and strain effects increase the reactivity. Exactly the opposite trend we expect for an overlayer of a less reactive metal deposited on a more reactive metal with a smaller lattice constant, such as, e.g., Pt on Ru [104]. This has in fact been verified in both experiment and theory [70, 105]. In section 2.4 we have done an ab-initio calculation on Pd overlayer on Cu. The Cu lattice constant is smaller than the one of Pd by 8% and Cu-Pd binding is stronger than Pd-Pd. These two effects represent exactly the opposite trend to Pd/Au, and both lead to a lower reactivity of Pd overlayer on Cu compared to pure Pd. Shubina and Koper have calculated CO adsorption energies on

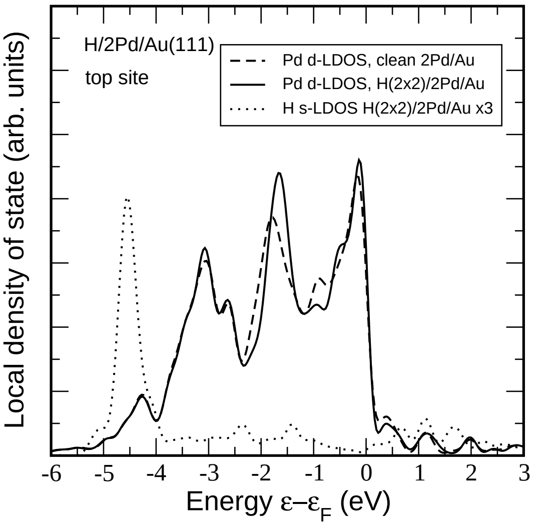

Figure 2.6: Local density of states of the hydrogen 1*s* state and the Pd subsurface *d*-band for atomic hydrogen adsorption at the top site of two Pd overlayers on Au(111) The hydrogen 1s density of state is multiplied by a factor of 5.

a Pt monolayer deposited on a number of different *d* band metals [70]. Their results also fully confirm our general model proposed above.

However, according to our analysis of the *d*-band center shifts, one Pd overlayer on Au should show the strongest binding since it has the highest *d*-band center; nevertheless, the binding energies show a maximum on two Pd overlayers on Au (see Fig. 2.1). Note that the difference in the hydrogen adsorption energies between the fcc and the hcp positions on Pd(111) is $\Delta E_{ads} = 0.036$ eV. This indicates that the second layer plays an important role for the adsorption because the fcc and hcp sites only differ in the second-nearest neighbors in the subsurface layer. We have therefore analyzed the modification of the electronic structure of the subsurface layer upon hydrogen adsorption. As Fig. 2.6 shows we find that the *d*-band LDOS of the subsurface layer is still perturbed by the presence of the atomic hydrogen on the surface, even for hydrogen adsorption at the on-top or fcc positions where the adsorbate distance is so far from the atom. However we see no hybridization of the LDOS at the position of the hydrogen 1s adsorbate resonance neither in the fcc hollow site nor in the on-top site. This indicates that there is no direct interaction between the adsorbed hydrogen and the second-layer atoms; the interaction is rather mediated indirectly via the modification of the electronic structure of the first-layer atoms. Furthermore in Fig. 2.7(a) and (b) we have also analyzed the charge density difference induced upon hydrogen adsorption at the on-top and fcc three fold positions of two Pd overlayers on Au(111) respectively. It is obvious that there is a sizable charge arrangement at the second layer atom which, however, is caused indirectly by the adsorbate through the strong perturbation of the electron distribution at the first layer atom.

Having established that there is an significant interaction of the adsorbates with the subsurface layer, we can understand the origin of the maximum in the binding energies

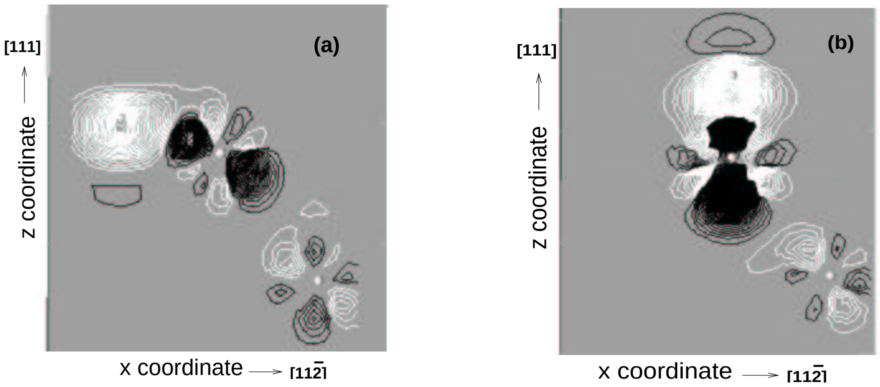

Figure 2.7: Charge density difference plot for hydrogen adsorption at the on-top position of two Pd overlayers on Au(111), fcc site (a) and top site (b). White contours correspond to charge accumulation while black contours denote charge depletion.

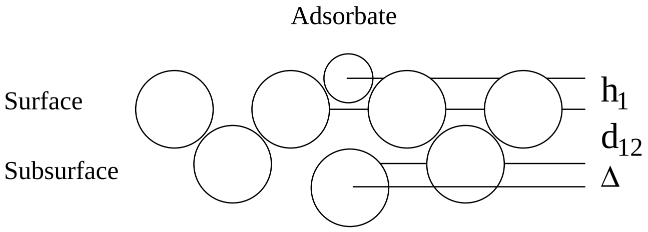

	Pd	Pd@Au	Pd on Au
h	0.32	0.14	0.40
d_{12}	1.98	1.85	1.93
Δ	0.02	0.04	0.13

Table 2.4: Hydrogen adsorption height h, first interlayer spacing d_{12} and relaxation displacement Δ of the second layer atom just below the adsorbate at the fourfold hollow position for unstrained and strained pure Pd(100) and one Pd overlayer on Au(100). The geometry is sketched in the figure above the table. All lengths are in Å.

for two Pd overlayers. Although the first Pd overlayer should be the most reactive according to the *d*-band model, there is an indirect coupling to the subsurface layer which consists of gold. Gold as a noble metal is rather unreactive which is reflected by the deep-lying *d*-band (see Fig. 2.5). Thus the high reactivity of the first Pd overlayer is overcompensated by the inertness of the Au subsurface layer. For two Pd overlayers, the subsurface layer (which is Pd) is more reactive leading to the maximum in the binding energies.

With respect to the substrate interaction, the fourfold hollow site of the surface(100) shows an exceptional behavior in the hydrogen adsorption energies. While for two Pd overlayers the hollow and the bridge site are energetically almost degenerate, on one Pd overlayer the twofold coordinated bridge site becomes favored by 50 meV compared to the fourfold hollow site.

In order to find out the reason for the significant decrease in the binding strength at

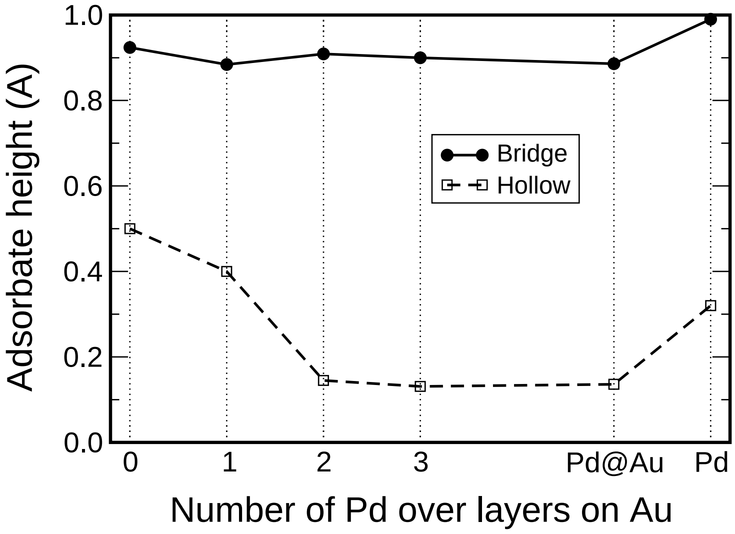

Figure 2.8: Hydrogen adsorption height as a function of the number of Pd overlayers at the bridge and fourfold hollow site of of the (100) overlayers systems at a coverage of $\theta = 0.25$.

the fourfold hollow position, it is instructive to analyze the hydrogen adsorption height at both the hollow and the bridge site (Fig. 2.8). Upon expanding the surface, the adsorption height is reduced both at the bridge and at the hollow position. However, whereas the adsorption height at the bridge site is more or less independent of the number of Pd overlayers on Au, at the hollow site there is a significant increase in the adsorption height when the number of Pd overlayers is reduced from two to one. Recall that at the fourfold hollow position the hydrogen atom is very close to the surface layer so that it is effectively fivefold coordinated. The increase in the adsorption height for one Pd overlayer then indicates that the hydrogen atom is repelled from the subsurface Au atom.

This conclusion is confirmed by an analysis of the electronic structure which reveals that at the hollow site the adsorbed hydrogen atom is in fact *directly* interacting with the $d_{3z^2-r^2}$ orbital of the Au atom directly beneath in the second layer. Since the d-band of Au is completely filled, this interaction is strongly repulsive. In Table 2.4 we have collected the relevant distances at this adsorption site. The repulsion between the H and the Au atom is so strong that the Au atom even relaxes downward towards the bulk away from the adsorbed H atom.

2.3.4 Coverage effects

In order to study coverage effects in the hydrogen adsorption we have calculated the hydrogen adsorption energy as a function of number of Pd overlayer on Au at a hydrogen coverage of $\theta = 1$. The results are shown in Fig. 2.9a and Fig. 2.9b for the (111) and (100) surface orientation, respectively. For the (111) orientation, we find basically the same trends in the adsorption energies as a function of strain and the number of Pd overlayers compared to the lower coverage. However, the bindings energies at all sites are smaller by 0.04-0.2 eV with respect to the corresponding values at the coverage of

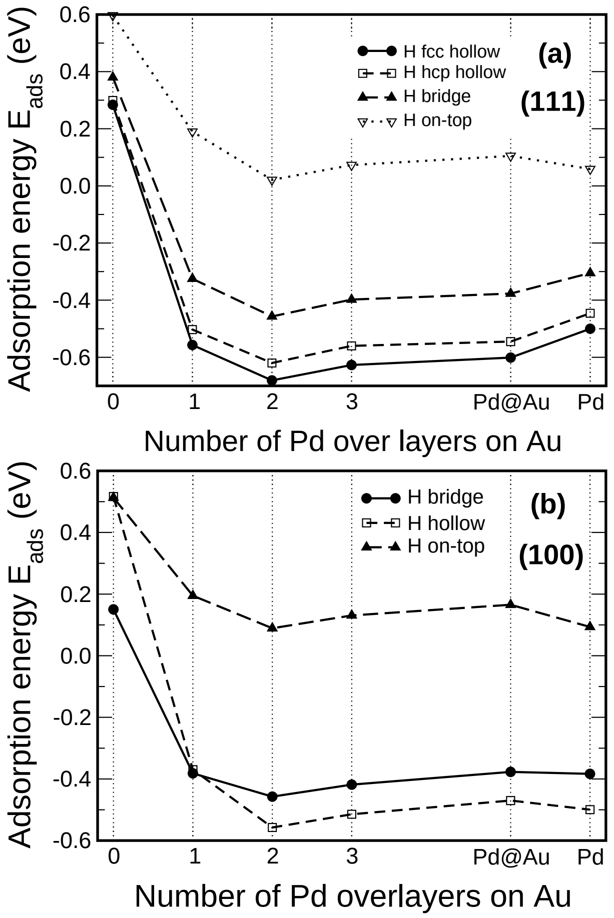

Figure 2.9: Hydrogen adsorption energy as a function of the number of Pd overlayers on Au for different adsorption sites on the (111)(a) and the (100) surfaces (b) at the coverage of $\theta = 1$. The pure Pd substrates with the lateral lattice constant of Au (a=4.18 Å) and Pd (a=3.96 Å) are labeled by Pd@Au and Pd, respectively.

$\theta = 0.25$.

At the (100) surface, the hydrogen binding energies at a coverage of $\theta = 1$ are also lowered with respect to the coverage $\theta = 0.25$, but to a smaller extent of only 0.06-0.1 eV. However, as Fig. 2.10 shows the fourfold hollow site again exhibits an exceptional behavior insofar as the binding on pure Pd and on more than one Pd overlayer on Au is in fact slightly *increased* compared to the lower coverage.

These findings can be traced back to an electrostatic interaction between the adsorbates. Adsorption of atomic hydrogen on Pd is associated with an increase in the work function by about 140 to 390 meV [99, 106], depending on the adsorption site. This indicates that there is a charge transfer from the substrate to the adsorbate, creating a dipole layer. The lateral interaction of these dipoles is repulsive. This explains the decrease in the binding energies for higher coverages. It also explains why the effect is slightly larger on the close-packed (111) surface because there the concentration of H atoms is larger. For a coverage $\theta = 1$ (100) surface.

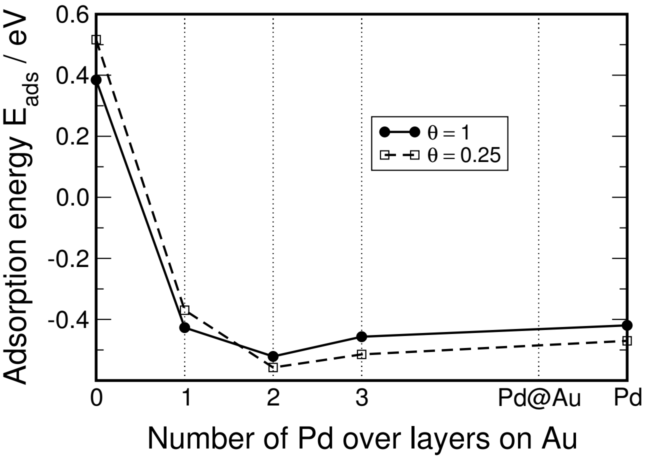

Figure 2.10: Hydrogen adsorption energy on four-fold hollow site (100) surface as a function of the number of Pd overlayer on Au for a coverage $\theta = 0.25$ and coverage $\theta = 1$

On the fourfold hollow site, however, the hydrogen atoms are located so deep within the first Pd layer that the electrostatic dipole-dipole repulsion between adjacent hydrogen atoms is effectively screened so that a small net attraction between the hydrogen atoms remains [97, 106]. On Au(100) and one Pd overlayer, the H minimum energy adsorption position is further away from the surface (see Fig. 2.8). Hence, there the direct dipole-dipole interaction is operative leading to the net repulsion.

2.4 Pd/Cu and Cu/Pd: Computational method and overlayer structures

In order to generalize our results for Pd overlayer on Au, here we have replaced the substrate Au with Cu. Cu is also a noble metal but with a smaller lattice constant compare to Pd. If the interaction between Pd and Cu is also lower than Pd-Pd, regarding to our model described in section 2.3.1, there will be a competition between substrate interaction effects and lattice strain effects. Our model will be then qualified by comparing the reactivity of Pd/Cu overlayer to the reactivity of Pd/Cu.

We have performed a self-consistent DFT calculation for Pd overlayer on Cu. In order to be able to compare our results with results from Pd/Au, most of the computational setup parameters has been chosen as for Pd/Au. The Kohn-Sham one-electron valence states are expanded in a basis of plane waves with the cutoff energy of 235 eV. The structural properties of bulk Cu were determined by fitting the Murnaghan equation of state to the computed total energies per primitive unit cell and it has been listed in Table 2.5.

The overlayer structure has been modeled by a slab of four layers of the Cu substrate. All layers structures are separated by at least 10.5 Å of vacuum. The two bottom layers of the slabs have been fixed at their corresponding bulk positions, while all upper layers including the Pd overlayer have been fully relaxed. Due to the lower

	lattice const.(Å)	B_0 (GPa)	E_{cohen} (eV)
Theory	3.64	146	3.757
Exp.	3.61	140	3.50

Table 2.5: Lattice constant, bulk modulus and cohesive energy of Cu

interlayer distance	Cu	Pd/Cu	Pd@Cu	Cu@Pd	Cu/Pd	Pd
d_{12} [Å]	2.08(-1)	2.23(6)	2.30(10)	1.92(-16)	2.07(-9)	2.30(0)
d_{23} [Å]	2.09(0)	2.10(0)	2.28(9)	1.95(-15)	2.32(-2)	2.28(0)
d_{34} [Å]	2.10(0)	2.10 (0)	2.29(9)	2.28 (0)	2.29(0)	2.29(0)

Table 2.6: Layer relaxation of the Pd/Cu(111) as well as Cu/Pd(111) overlayer surface. The DFT-GGA relaxations were computed for the pure Cu, one Pd overlayer on Cu and pure Pd. The pure Pd (Cu) substrate with lateral lattice constant of Cu (Pd) is labeled by Pd@Cu (Cu@Pd). The relative change to the bulk interlayer distance (in %) is given in parentheses. Positive numbers correspond to a surface expansion away from the bulk substrate.

density of state at Fermi level of Cu we need more k-points set to get the convergence of total energy with respect to number of **k**-points. Hence, the surface Brillouin zone is sampled by a Monkhorst-Pack **k**-point set of 11 × 11 × 1 for a (2 × 2) unit cell, corresponding to 16 **k**-point in the irreducible Brillouin zone.

Table 2.6 shows the calculated layer relaxation for one Pd overlayer on Cu as well as one Cu overlayer on Pd. The pure Pd(Cu) substrate with lateral lattice constant of Cu (Pd) is labeled by Pd@Cu (Cu@Pd). There is no significant relaxation neither for pure Cu nor for pure Pd while for Pd/Cu and Cu/Pd, the relaxation are 6-9% due to the lattice mismatch between Pd and Cu.

2.5 Pseudomorphic Pd/Cu and Cu/Pd overlayers

Due to the fact that pseudomorphic Pd overlayer are strongly compressed by 8% on Cu substrate, they are not stable. They rather form a alloy. Pd/Cu surface alloy formation has been reported in many references [107]. De Siervo [108] for example performed a X-ray photoelectron diffraction in combination with LEED to determine the structure of ultra-thin epitaxial Pd film (1ML) evaporated on Cu(111) single crystal surface. The analyzed data show that Pd has formed a random substitutional alloy with Cu. The analyzed data also show a diffusion of Pd into second and third layers. The Pd concentration are 20%, 70% and 20% for first, second and third layer respectively. As Fig. 2.11 shows our DFT calculation on Pd/Cu surface alloy also confirms a energetically more stable Pd_2Cu_1/Cu surface alloy. Here the surface alloy formation energy

$$E_{surf} = \frac{(E^{slab}_{Pd_xCu_y/Cu} - E^{slab}_{Cu} - yE^{coh}_{Cu} - xE^{coh}_{Pd})}{N_{sa}} \tag{2.1}$$

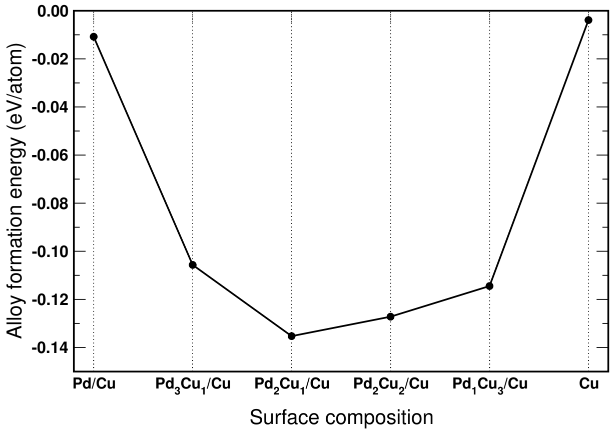

Figure 2.11: Surface energy in eV/atom according to Eq. 2.1 for different surface compositions of PdCu alloys on Cu(111). The energy zero corresponds to a Cu layer on Cu(111), i.e., to a pure Cu(111) surface.

is plotted for an number of different $\mathrm{Pd}_x\mathrm{Cu}_y$ surface compositions. N_{sa} is the number of surface atoms per surface unit cell, i.e., $N_{sa} = x + y$. E^{coh}_{Pd} and E^{coh}_{Cu} are the cohesive energies of Pd and Cu, which have been taken from Table 2.1 and Table 2.5 respectively. This means that we have assumed that both Cu and Pd are in equilibrium with their corresponding bulk reservoirs. For a pure Cu surface, E_{surf} according to Eq. 2.1 is zero, i.e. the energies plotted in Fig. 2.11 are defined with respect to the pure Cu surface. The fact that the value for Cu in Fig. 2.11 is not exactly zero is due to the finite thickness of the Cu slab in the calculations. As Fig. 2.11 demonstrates, among the ordered surface alloys considered by us the $\mathrm{Pd}_2\mathrm{Cu}_1$ alloy is the most stable. Note that the surface alloy calculation has been performed only for the first upper layer. The fact that Pd and Cu form alloy indicates that there is a strong attraction interaction between Pd and Cu. In Table 2.7 we have calculated the Cu-Pd binding energy in the case of atomic and overlayer desorption. One Pd atom desorbed on Cu(2×2) unit cell shows a binding energy E=-3.011 eV while one Cu atom on the Cu substrate shows a lower binding energy E=-2.704 eV. In the case of Pd-Cu overlayer, we also find that one Pd overlayer on Cu substrate is more strongly bounded than on Pd substrate with lateral Cu lattice constant (Pd@Cu).

system	Binding energy (eV/atom)
Pd atom / Cu slab	-3.011
Cu atom / Cu slab	-2.704
Cu atom / Pd slab	-2.950
Pd atom / Pd slab	-2.766
Pd overlayer / Cu	-4.447
Pd overlayer / Pd@Cu	-3.446

Table 2.7: The binding energy of one Pd atom, Cu atom, Pd overlayer and Cu overlayer on Pd and Cu substrates.

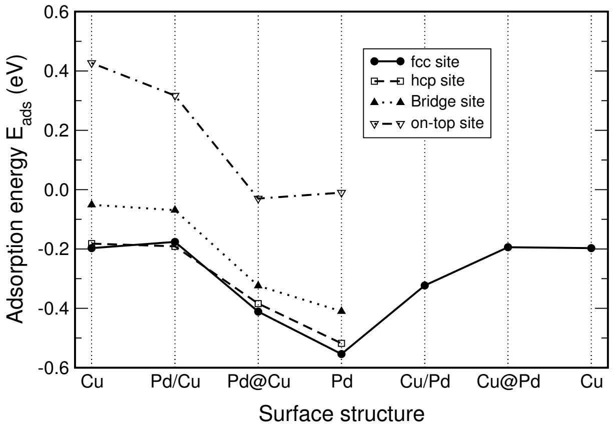

Figure 2.12: Atomic hydrogen adsorption energy on bimetallic PdCu surfaces for a quarter monolayer hydrogen coverage, namely on pure Cu(111), on a pseudomorphic Pd overlayer on Cu(111) (Pd/Cu), on pure Pd(111) with the lateral Cu lattice constant (Pd@Cu), on pure Pd(111), on a pseudomorphic Cu overlayer on Pd(111) (Cu/Pd), and on pure Cu(111) with the lateral Pd lattice constant (Cu@Pd).

Although PdCu surface alloys are more stable than a pure Pd/Cu overlayer, we have still determined the hydrogen adsorption energies on the pseudomorphic overlayer system in order to compare the results with those for the Pd/Au overlayers. Furthermore, small domains of a Pd/Cu overlayer may exist in the submonolayer coverage regime [107]. In Fig. 2.12, we have summarized the calculated results for the atomic hydrogen adsorption energies on the different high-symmetry sites on pure Cu(111), on a pseudomorphic Pd overlayer on Cu(111) (Pd/Cu), on pure Pd(111) with the lateral Cu lattice constant (Pd@Cu), on pure Pd(111), on a pseudomorphic Cu overlayer on Pd(111) (Cu/Pd) and on pure Cu(111) with lateral Pd lattice constant (Cu@Pd).

In order to explain the adsorption energy trend within the d-band model, in Fig. 2.13, we have plotted the local *d*-band center for the different surface structure of Fig. 2.12. First we note that the lateral compression of the Pd overlayer by 8% cause a down-shift of *d*-band from -1.81 eV to -2.33 eV. This leads to a reduction of the hydrogen binding energy for the higher coordinated adsorption sites which can be well-understood in terms of the *d*-band model [69, 87]. Note that the hydrogen adsorption energy on the on-top site again shows the opposite trend as the higher-coordinated sites. This trend has already been obtained for strained copper [103] and strained Pd surfaces (See section 2.3.2). The lateral lattice expansion of the pure Cu by 8% (Cu@Pd) cause a up-shift of *d*-band from -2.39 eV to -2.26 eV. No significant change has been seen on the hydrogen binding energy. This still can be understood in term of the *d*-band model since the Cu d-band is fully filled and hence the factor f in Eq. 1.87 which describes the number of occupied states in the d-orbital is f=1.

In contrast to the Pd/Au system, however, the interaction of Pd with the Cu substrate leads to a further down-shift of the Pd *d*-band center which is reflected in the lower hydrogen binding energies on the Pd/Cu(111) overlayer compared to the pure compressed Pd surface. In fact, the hydrogen adsorption energies on the Pd/Cu(111)

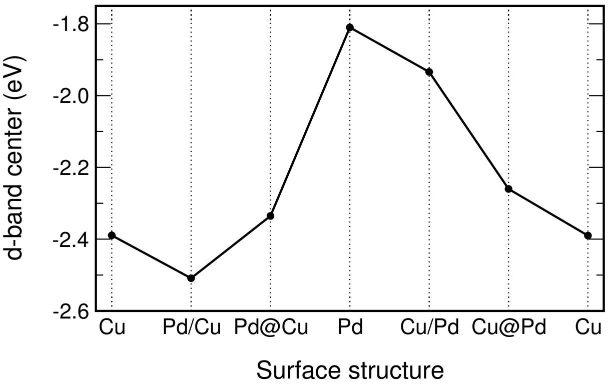

Figure 2.13: Position of the local d-band center of the topmost layer on bimetallic PdCu surfaces. The considered structures are the same as in Fig. 2.12.

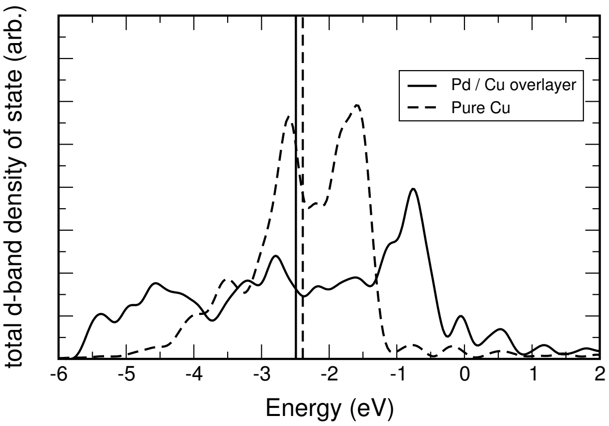

Figure 2.14: The local d-band density of state for Pd overlayer on Cu and pure Cu. The horizontal lines indicate the center of d-band position.

overlayer are very similar to the hydrogen adsorption energies on the pure Cu(111) substrate. A corresponding result has also been found for CO adsorption on a Pd/Cu(111) overlayer in DFT-GGA calculations [109]. Although Au and Cu are both noble metals, it is important to realize that the coupling of their d-bands to Pd is quite different. While the Au d-band center is 1.6 eV below the d-band center of Pd, the Cu d-band center is lower by only 0.6 eV (see Fig. 2.13). Due to the large energetic overlap between the Pd and Cu d-bands, there is a strong hybridization between both bands. The local d-band density of states for pure Cu and Pd overlayer on Cu is compared in Fig. 2.14. The local d-band density of states for Pd atoms is much broader than for pure Cu which indicates a strong hybridization between Cu and Pd d-bands. This hybridization is also reflected by the strong Pd-Cu interaction energies.

In order to round up the study of the CuPd overlayer system, we have also addressed the opposite stacking sequence, a pseudomorphic Cu overlayer on Pd(111). In contrast to the Pd/Cu(111) system, at room temperature Cu/Pd(111) has been found to grow in a layer-by-layer fashion for at least the first two layers [110]. Furthermore, underpotential deposition of Cu on Pd(111) in sulfuric acid solution has been observed [111, 112]. Calculated atomic hydrogen adsorption energies at the fcc hollow site of a pseudomorphic Cu overlayer on Pd(111) and on a pure Cu substrate with the lateral lattice constant of Pd(111) are included in Fig. 2.12. We first note that the geometric expansion of the Cu substrate has no influence on the hydrogen adsorption energies although the *d*-band center has moved upwards (see Fig. 2.13), as we have already found in a previous study [103]. The strong coupling between Cu and Pd for the Cu/Pd(111) overlayer system, on the other hand, causes a significant upshift of the Cu *d*-band center and larger hydrogen binding energies.

Chapter 3

Local reactivity of supported metal clusters: $\mathrm{Pd_n}$ on Au(111)

Fundamental knowledge and understanding of the physical and chemical properties of nanoscale metal particles is of considerable scientific interest as well as technological relevance. The properties of nanoparticles are of general importance in surface science, heterogeneous catalysis and electrochemistry. Nanoparticles have special properties which often differ very much from those of bulk material [113]. In particular, the properties often strongly depend on the size and geometry of the clusters. For instance elements that are usually chemical inert can become catalytically active [114]. In one experiment, Valden *et.al.* [115] prepared a gold clusters ranging in diameter form 1 to 6 nanometer on single crystalline surfaces of titania to investigate the unusual size dependence of the low-temperature catalytic oxidation of carbon monoxide. They found that islands with two layers of gold are most effective for catalyzing the oxidation of carbon monoxide. Another surprising property of systems with reduced dimensions is that some kinds of metals which are nonmagnetic in the bulk become magnetic in a cluster geometry. Wildbeger *et.al.* [113] performed an ab initio calculation for the electronic structure of $4d$ transition metals clusters at the (001) surface of Ag and determined a magnetic moment for both free and deposited clusters. Note that $4d$ bulk transition metals in general do not show any magnetic moment, therefore, there is a strong current interest in the study of supported metal clusters, because of their technological relevance in e.g. the design of nanoscale magnetic storage devices.

In experiments with nanoparticles, an accurate control of the particle size is of paramount importance in investigating physical and chemical properties of supported particles, especially if one is interested in particle size dependence. Typically, a large number of particles are deposited on an inert substrate in order to obtain sufficiently high signals. Although the variation in particle size achievable by different preparation methods (e.g. vapour deposition, electrochemical deposition and adsorption from colloidal solutions) is rather limited. A broader size distribution often results on the surface due to agglomeration of single particles [116–118].

On the other hand, it can be calculated that the diffusion limited current of electrodes covered with many particles is reduced compared to an electrode with only one particle. The surface concentration of reactants is proportional to r/r_0, with r being the distance between particles and r_0 the particle radius. Therefore a method to produce particles with a narrow size distribution is advantageous. Meier *et.al.* [119] performed a experiment in which they used the STM tip to deposit a cluster on the substrate. In this method which was developed first by Kolb *et.al.* [120, 121] the metal is first deposited on the tip of the STM, then the tip is brought into contact with the electrode surface, and on withdrawal a cluster is left behind [122]. The clusters are found to be larger and more stable if the tip is moved further towards the electrode surface in the generation process. The clusters generated in this study varied in height between 0.3 and 1.8 nm and their diameter was found to be between 5 and 20 nm. Despite much research in this area, neither the formation nor the properties of these clusters are well understood. We have therefore undertaken a theoretical study of palladium clusters with three different sizes on a Au(111) substrate. This particular system was chosen for two reasons: palladium is a good catalyst for many important reactions, and it forms stable alloys with gold [123]. The system Pd/Au is also of particular interest in the field of electrocatalysis because of its catalytic activities in the oxidation reactions of methanol, formic acid and carbon monoxide.

In this chapter we present periodic DFT calculations of Pd clusters with three different number of atoms n=3, 7, 10 supported by Au(111). We have used atomic hydrogen and CO adsorption energies as a local probe in order to determine the trend in the reactivity. Surprisingly, on the Pd_n/Au(111) cluster we find that most adsorption energies are smaller than those on Pd/Au pseudomorphic overlayers (see section 2.2). Thus, nano-size supported metal cluster are not necessarily more reactive than thin films. The reduced adsorption energies of the supported clusters are caused by their compressive relaxations together with the support interaction. Based on our results and previous kinetic modeling [124] we propose that flat Pd nano-islands instead of three-dimensional nano-crystals are responsible for the higher hydrogen evolution rate observed in recent STM experiments [119].

3.1 Computational setup

Self-consistent periodic DFT calculation have been performed using the Vienna ab initio simulation package (VASP).The exchange-correlation effects have been described within the generalized gradient approximation (GGA) using Perdew-Wang (PW-91) functional. The ionic cores are represented by ultrasoft pseudopotentials. The Kohn-Sham one-electron valance states are expanded in a basis of plane waves with cutoff energies of 200 eV for H adsorption and 400 eV for CO adsorption. The calculated equilibrium lattice constants have been taken from Table 2.1. The Au(111) substrate has been modeled by a four-layer slab separated by 14.5 Å and 17.2 Å of vacuum for H and CO adsorption, respectively. Since we were interested to simulate a Pd cluster on a Au substrate, the distance between Pd and the Pd in the next unit cell must be

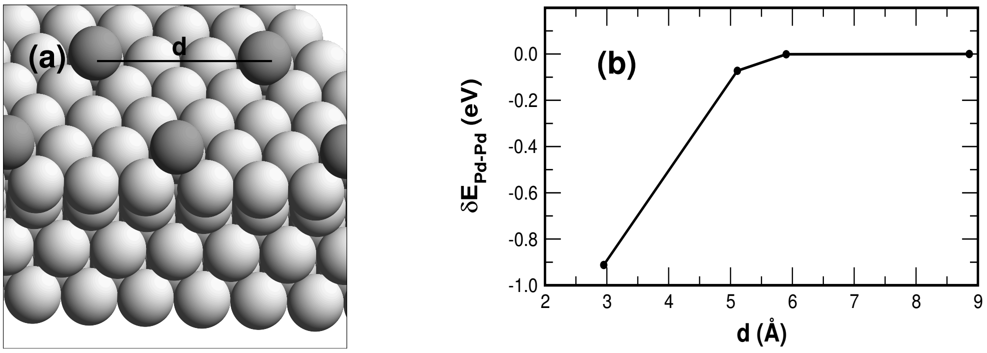

Figure 3.1: (a) adsorption of one Pd atom on (3×3) super cell of Au(111), d is the distance between Pd atoms in the neighboring super cells. (b) The variation of Pd-Pd interaction energy as a function of Pd-Pd distance d.

as far as possible. A sufficient Pd-Pd distance can be calculated by adsorption of one Pd atom on the Au substrate and varying the unit cell size (see Fig. 3.1a). In this case the Pd-Pd interaction energy is given by

$$\mathrm{E_{Pd-Pd} = E_{slab+Pd} - E_{slab} - E_{Pd} - \Delta E} \tag{3.1}$$

where $\mathrm{E_{slab}}$ is the energy of the substrate Au and $\mathrm{E_{Pd}}$ is the energy of one Pd atom in the gas phase. ΔE is the binding energy of Pd and Au substrate which we assume to be independent of the unit cell size. The variation of $\mathrm{E_{Pd-Pd}}$ with respect to unit cell size is giving by

$$\delta\mathrm{E_{Pd-Pd}} = \delta\mathrm{E_{slab+Pd}} - \delta\mathrm{E_{slab}} \tag{3.2}$$

where $\delta\mathrm{E_{Pd-Pd}}$ is the variation of the Pd-Pd interaction energy with respect to the Pd-Pd separation distance. We expect that this energy becomes converged for long Pd-Pd distances. Here we neglect the Pd-Pd interaction through the substrate Au which can be different for different unit cells. In Fig. 3.1b we have plotted the δE_{Pd-Pd} as a function of Pd-Pd distance d. It shows a convergence of E_{Pd-Pd} at about d=6 Å. Thus in order to satisfy the minimum Pd-Pd distance d=6 Å, a 3×3 surface unit cell and a 4×4 surface unit cell are sufficient for the supported triangular Pd$_3$ clusters and hexagonal Pd$_7$ clusters respectively. For 3×3 and 4×4 surface unit cells we used a Monkhorst-Pack set of 5×5×1 and 3×3×1 **k**-points, respectively. As it has been explained a magnetic moment has been obtained for 4*d* transition metals clusters at the (001) surface of Ag [113]. By performing spin-polarized calculations on Pd$_3$ cluster supported on Au(111) we checked whether the supported Pd$_n$ cluster show magnetic behavior, but we found no magnetic polarization which is in agreement with the previous calculation for metal-supported Pd clusters [113].

3.2 Pd$_3$ and Pd$_7$ planar clusters

In Table 3.1 we have summarized the results for the structural relaxation of the planar Pd$_3$ clusters. In order to understand the substrate effects we also compared them

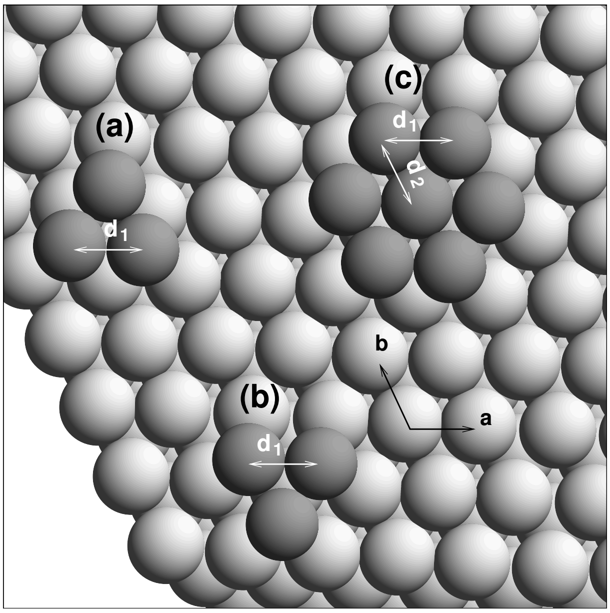

Figure 3.2: Schematic sketch of Pd planar clusters on Au substrate. (a) Pd_3 bounded by {111}, (b) Pd_7 bounded by {100}. (c) Pd_7

with structural relaxation of Pd cluster on Pd with the lateral lattice constant of Au (Pd/Pd@Au)and with pure Pd. The nearest-neighbor distances in the planar Pd_3 and Pd_7 cluster on Au(111) are 2.76-2.77 Å. This is even smaller than the nearest-neighbor distance in Pd bulk (d=2.80 Å) although the Au substrate has a 5% larger lattice constant than Pd. Note that there are two inequivalent triangular cluster on (111) surfaces bounded by {111} (Fig. 3.2a) and {100}-like microfacets (Fig. 3.2b), respectively. The (111) surfaces bounded by {111} and {100} microfacets were used for hydrogen and CO adsorption on fcc and hcp sites respectively.

Relaxation effects are in fact well-known for clusters; for example, significant compressions for Pd gas-phase cluster with up to 140 atoms have been found in DFT calculations [125]. Our calculation on Pd_3 and Pd_7 cluster in the gas phase show Pd-Pd distance of d=2.50 Å and d=2.64 Å respectively which are significantly shorter than those of a cluster supported by a substrate. The comparison between the Pd free clusters with those supported by a substrate in Table 3.1 indicates that the existence of a substrate plays a major role in the Pd-Pd separation. On the other hand in Table 3.1 the Pd-Pd distance for Pd_3 supported by Pd with the lateral lattice constant of Au and pure Pd are compared. Although the substrates differ in the lattice constants the supported clusters show almost the same distances. In addition our calculation on the electronic properties of Pd_3 supported by Pd@Au and pure Pd shows that the position of the *d*-band center of Pd atoms is modified only by up to 0.03 eV. These two effects confirm that the lattice constant mismatch between Pd and Au plays a minor effect on determining the electronic and structural properties of Pd_3 clusters.

For Pd_3 clusters supported by Au we found that the energy corresponding to the Pd_3 cluster bounded by {111} facets is ΔE=0.62 eV below the value for Pd_3 bounded

	Pd/Au(111)			Pd/Pd@Au(111)			Pd/Pd		
	Pd_3	Pd_7	Pd overlayer	Pd_3	Pd_7	Pd overlayer	Pd_3	Pd_7	Pd overlayer
d_1	2.76	2.76	2.96	2.76	2.76	2.96	2.72	2.76	2.80
d_2	—	2.77	2.96	—	2.77	2.96	—	2.74	2.80

Table 3.1: Calculated nearest-neighbor Pd-Pd distances in Å. d_1 and d_2 are the Pd-Pd nearest-neighbor along the two basis vectors **a** and **b** (see Fig. 3.2)

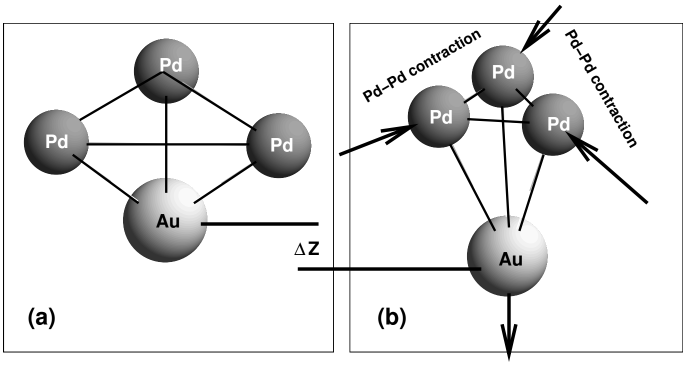

Figure 3.3: Relaxation process of the Au atom in the second layer of Pd_3 bounded by {100} due to the Pd relaxation. (a) before Pd relaxation, (b) after Pd relaxation

by {100} facets. In order to find out the reason for this significant change in the energy, it is constructive to analyze the position of the Au atom in the second layer just in the middle of the Pd triangle for Pd_3 bounded by {100} facet (Fig. 3.3(a)). Due to the Pd contraction, the distance between the Pd atoms and the Au atom whose position is just below the Pd atoms and in the middle of the triangle become shorter. Therefore the Au is repelled by Pd atoms and shifts along the surface normal down toward the bulk as it has been shown in Fig 3.3(b). The amount of this shift is Δz=0.24 Å. The Au atom will be then repelled by the Au atoms in the third layer. This shift causes the Pd_3 bounded by {100} facet to be energetically less favorite. Note that for Pd_3 bounded by {111} facet there is no such Au atom at the middle of the triangle, therefore such a mechanism is not valid for that case.

The H and CO adsorption energies on the planar supported clusters are calculated and compared to those on the overlayer in Fig. 3.4. The hydrogen and CO adsorption energies have been calculated by Eq. 1.82 and Eq. 1.78 respectively. The binding energies of hydrogen and CO in the gas phase were calculated to be 4.55 eV and 11.43 eV respectively. While on the Pd_3 cluster the binding energies are comparable or even stronger than on the Pd/Au(111) overlayer, on the Pd_7 cluster the binding energies are significantly smaller. Note that on the Pd/Au(111) overlayer the binding energies are already larger than on the Pd(111) surface (see section 2.2).

These results can all be understood within the *d*-band model. Tensile strain and

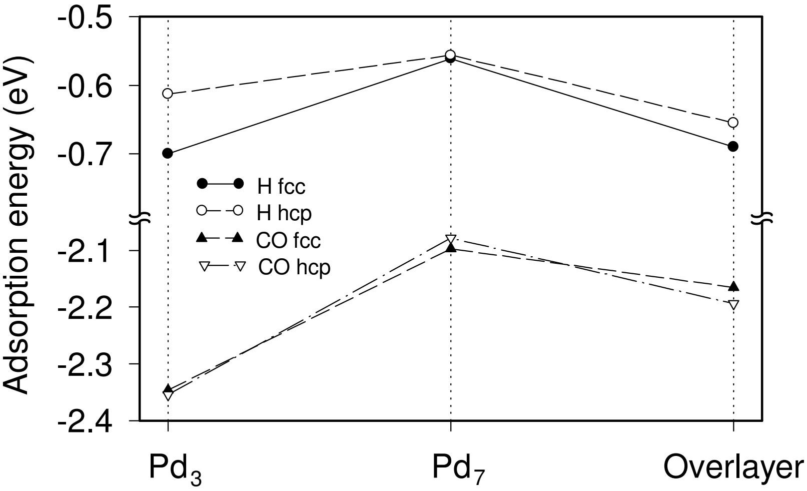

Figure 3.4: Calculated CO and hydrogen adsorption energies on planar $\mathrm{Pd_3}$ and $\mathrm{Pd_7}$ clusters deposited on Au(111) compared to the corresponding adsorption energies on the Pd/Au(111) overlayer.

substrate interaction effects lead to a upshift of the *d*-band center from $\epsilon_d = -1.64$ eV for Pd(111) to $\epsilon_d = -1.27$ eV for the Pd/Au(111) overlayer with respect to the Fermi energy (see section 2.3.1). For the supported clusters, there are two opposing effects. On the one hand, the lower coordination of the cluster atoms should lead to a further upshift of the *d*-band center. On the other hand, the reduction of the Pd-Pd distances has the opposite effect. As for the $\mathrm{Pd_3}$ clusters, both effects almost cancel each other. For $\mathrm{Pd_3}$ the d-band center is located at -1.21 eV close to the value for the overlayer (see Fig. 3.5) consequently, the adsorption energies are comparable to the Pd/Au(111) overlayer. The local *d*-band centers of the $\mathrm{Pd_7}$ cluster are at -1.26 eV and -1.48 eV at the corner and the center atoms, respectively. The low-lying *d*-band center of the center atom reflects the high coordination of this atom, $N = 9$, where N is the coordination number. At the three-fold hollow sites, the adsorbate binds to two corner atoms and the center atom. The higher coordination of the center atom in the $\mathrm{Pd_7}$ cluster together with its compression lead to the smaller binding energies.

We have analyzed the electronic structure in even more detail. In Fig. 3.6, we present the orbital resolved *d*-band local density of states (LDOS) for $\mathrm{Pd_3}$ clusters deposited on Au(111) and on Pd(111). In addition, we compared the LDOS of the supported clusters with those of the free $\mathrm{Pd_3}$ cluster. The free cluster exhibits a discrete structure of electronic levels, as is expected for a finite system. Interestingly, for the $\mathrm{Pd_3}$/Au(111) cluster the *d*-band orbitals that are confined within the cluster layer, i.e., within the *xy*-plane, namely the d_{xy} and the $d_{x^2-y^2}$ orbitals, also show a rather discrete structure. This means that these orbitals are indeed confined within the cluster. The other three orbitals, however, that have a component along the vertical *z*-direction are already rather broad, indicating the significant coupling to the Au(111) substrate.

The $\mathrm{Pd_3}$ cluster is even more strongly coupled to an underlying Pd(111) substrate with a lateral lattice constant of Au ($\mathrm{Pd_3}$/Pd@Au), as the LDOS in Fig. 3.6 demon-

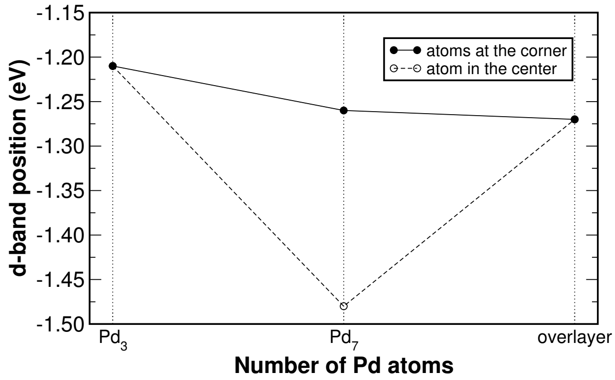

Figure 3.5: The position of d-band center of Pd_3 and Pd_7 are compared with Pd overlayer on Au(111). The hollow circle symbol in Pd_7 indicated the center of d-band of atom in the center of the cluster (see Fig: 3.2(c))

strates (see also section 2.3.3 for Pd overlayer on Au(111)). In this case, *all d* orbitals in the cluster are considerably broadened. The stronger coupling is also reflected by a deeper lying d-band center at $\varepsilon_d = -1.43$ eV for Pd_3/Pd@Au(111) compared to $\varepsilon_d = -1.21$ eV for the Pd_3/Au(111) cluster. This deeper lying d-band center also leads to smaller binding energies of the adsorbates. For example, the adsorption energies of atomic hydrogen are only -0.423 eV and -0.552 eV on the hcp and fcc sites, respectively, on the Pd_3 cluster supported by Pd@Au(111) compared to -0.61 eV and -0.70 eV at the corresponding sites of the cluster on the Au(111) support.

In 1991 Kolb *et al.* [120] performed an experiment in which small cluster of copper were arranged on gold surfaces by the tip of the scanning tunneling microscope (STM). Copper is first electrodiposited from solution onto the STM tip and then transferred from the tip to the substrate. The resulting metal bridge between the tip and sample breaks upon retraction of the tip, leaving a copper cluster on the surface. The height of the copper clusters can be controlled between two and five atomic layers by varying the tip approach. They turn out that the smaller copper clusters are electrochemically more stable. For such a small clusters the sample potential needs to be higher in order to Cu clusters being dissolved. They suggested that the unusually high stability of small copper clusters on Au(111) could be caused by quantum confinement effects [121] that would lead to a discrete electronic spectrum in the clusters. Our calculations show that already small supported Pd_3 clusters exhibit a continuous spectrum. The strong coupling to the substrate leads to the metallic nature of these clusters. For larger clusters quantum confinement effects are even less likely; hence our calculations do not support the speculation of Ref. [121].

3.3 Three-dimensional cluster Pd_{10}

The growth of single crystalline layers on a single crystalline substrate is a very important process in electrochemistry. This process is called epitaxial growth and can be used to control doping profiles as well as to form heterostructures. The growth of thin films

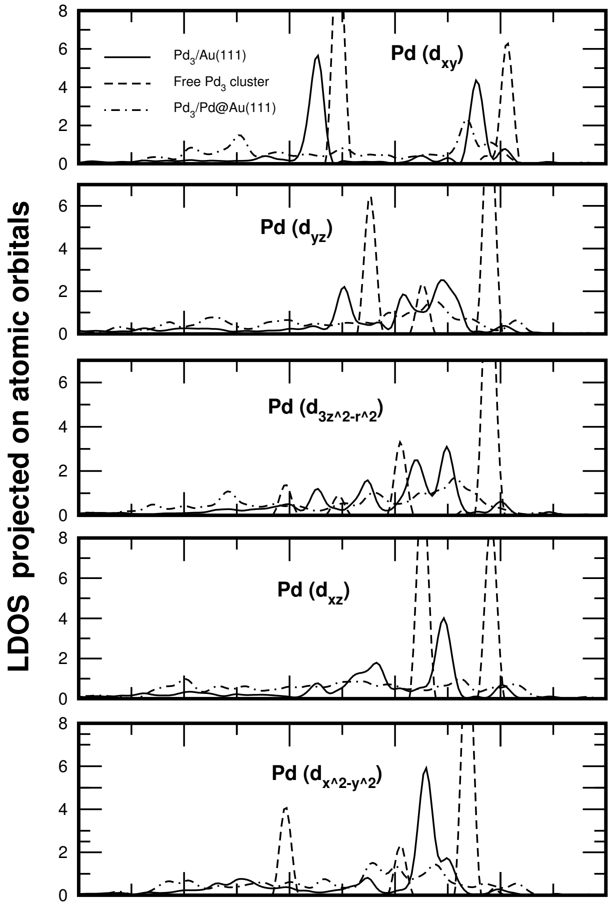

Figure 3.6: Orbital resolved *d*-band local density of states (LDOS) of the $\mathrm{Pd_3}$/Au(111), $\mathrm{Pd_3}$/Pd(111) and the free $\mathrm{Pd_3}$ clusters.

can be characterized into three modes: Frank-van der Merwe which is a two-dimension layer-by-layer growth, Volmer-Weber, where the deposited material forms 3-dimension islands on the surface and Stranski-Krastanow which is two-dimension growth followed by three-dimension growth (Fig. 3.8) [126]. In order to estimate which one of those modes occurs we considered the energy difference between the two epitaxial overlayer arrangement depicted in Fig. 3.8(a) and (c). The inputs to this calculation are three macroscopic surface tensions: γ_0, γ_i and γ_s are surface tension of overlayer-vacuum interface, the overlayer-substrate interface and the substrate-vacuum interface respectively. We may assume, without loss of generality, that the Volmer-Weber cluster occupies half of the available surface area (A). It follows immediately that

$$\Delta\mathrm{E} = \mathrm{E_{FV}} - \mathrm{E_{VW}} = (\gamma_0 + \gamma_\mathrm{i})\mathrm{A} - \frac{1}{2}(\gamma_0 + \gamma_\mathrm{i} + \gamma_\mathrm{s})\mathrm{A} \qquad (3.3)$$

Therefore we expect a complete FV growth for $\Delta\mathrm{E} > 0$ and a VW growth for $\Delta\mathrm{E} < 0$ and $\Delta\mathrm{E} = 0$ for SK growth. It is important to keep in mind that this estimate is only qualitatively useful because we have completely neglected any effects which might arise from the anisotropy of the surface tensions. Since we are interested on only

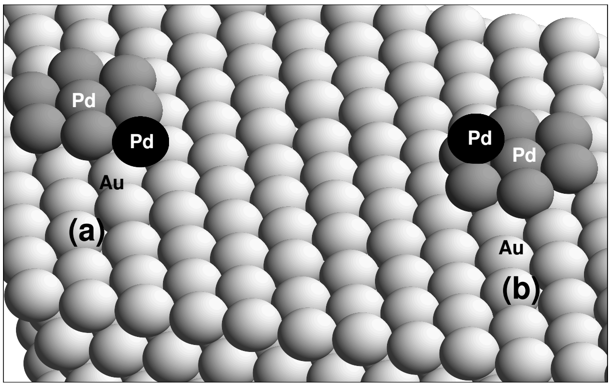

Figure 3.7: one additional Pd atom desorption (black sphere) on Au(111), (a) in one layer next to the Pd_7 cluster, (b) on top of the Pd_7 cluster.

growth modes therefore only the sign of the Eq. 3.3 is important for us. Hence we can neglect the factor A because it is multiplied by the whole Eq 3.3. Thus a simple equation for Eq. 3.3 is given by

$$\Delta \mathrm{E} = \gamma_0 + \gamma_\mathrm{i} - \gamma_\mathrm{s} \tag{3.4}$$

In the case of Pd/Au in order to estimate which kind of these mode can be occurred, we have calculated the surface energies γ_0, γ_i and γ_s for three Pd overlayer on Au, the interface region between Pd-Au and pure Au respectively. Note that due to the Pd-Au lattice mismatch and thus a Pd-Pd contraction, the surface energy γ_0 for VW and FM are different. Therefore the γ_0 is splited into γ_0^{FM} and γ_0^{VW} for Pd overlayer on Au and Pd cluster on Au respectively and hence Eq. 3.4 is simply modified by

$$\Delta \mathrm{E} = 2\gamma_0^{\mathrm{FM}} - \gamma_0^{\mathrm{VW}} + \gamma_\mathrm{i} - \gamma_\mathrm{s} \tag{3.5}$$

The values of the surface energies for pure Au, Pd overlayer on Au, Pd cluster on Au and Pd-Au interface have been calculated as γ_s=0.323, γ_o^{FM}=0.566, γ_0^{VW}=0.492 and γ_i=-0.287 eV/unit cell respectively. From these values the ΔE=-0.19 eV is calculated. The negative sign shows a preferably FM growth of Pd/Au which is in good agreement with the experiment [62].

In order to confirm our calculation we have also performed a DFT calculation of one additional Pd atom desorption next to the hexagonal Pd_7 cluster supported by Au (Fig. 3.7(a)) and on top of the hexagonal Pd_7 cluster supported by Au (Fig. 3.7(b)). The total energy of both structures have been compared. The one Pd atom next to the Pd_7 cluster shows a lower energy by δE=0.607 eV. Therefore layer by layer Pd desorption on Au is again preferable.

Although our calculations show that the first layer of Pd grows as a complete overlayer on Au(111), we have still determined the geometric structure and hydrogen and CO adsorption energies on this cluster since small domain of a two-layer Pd cluster on Au has also been prepared by Kolb *et.al.* [119]. In Fig. 3.9(a-d) we have summarized the geometry relaxation of Pd_{10} cluster supported by Au, Pd@Au, pure Pd and free

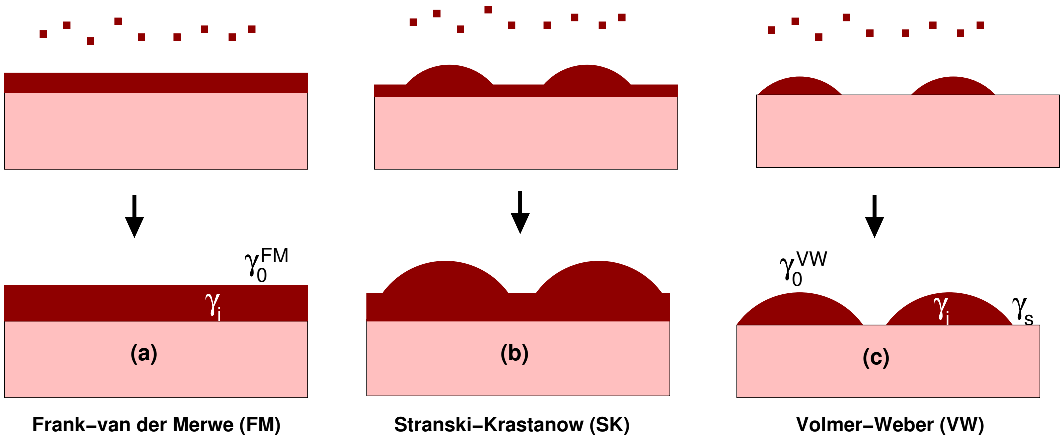

Figure 3.8: three different modes of thin film growing on a substrate. γ_0, γ_i and γ_s are surface tension of overlayer-vacuum interface, the overlayer-substrate interface and the substrate-vacuum interface respectively.

$\mathrm{Pd_{10}}$ cluster respectively. The Pd-Pd distance in the top layer of the three-dimensional $\mathrm{Pd_{10}}$ cluster supported by a substrate is even further reduced to 2.65-2.69 Å. The corresponding value for the free $\mathrm{Pd_{10}}$ cluster is 2.62 Å which is almost the same as for $\mathrm{Pd_{10}}$ cluster supported by Au and Pd. The Pd-Pd distance in the second layer are 2.72 to 2.76 Å for Au and Pd substrates. For the free $\mathrm{Pd_{10}}$ cluster the Pd-Pd distance in the second layer is 2.64 Å which is significantly shorter than for the $\mathrm{Pd_{10}}$ cluster on a substrate. The similarity between Pd-Pd distances in $\mathrm{Pd_{10}}$ cluster supported by Pd with lateral lattice constant of Au and pure Pd again indicates that the lattice constant mismatch plays a minor effect on structural relaxation of Pd cluster.

The H and CO adsorption positions and energies on the three-dimensional $\mathrm{Pd_{10}}$/Au(111) clusters are collected in Fig. 3.10. Surprisingly, we note that all calculated adsorption energies on the supported $\mathrm{Pd_{10}}$ clusters are smaller than those on the planar clusters and on the overlayers. There are three symmetrically distinct atomic positions, the center and the corner positions in the first or lower layer and the second or upper layer position. The local d-band centers at these three positions are located at -1.83 eV, -1.41 eV and -1.39 eV, respectively. Although the coordination of the corner atom in the first layer, $N = 7$, is larger than the one of the second layer atom, $N = 5$, still the local d band centers are almost at the same position. Again, this can be understood by the reduced distance of the topmost Pd atoms which increases their effective coordination. Consequently, the adsorption energies on top of the $\mathrm{Pd_{10}}$ clusters are rather similar to the ones at the sides.

Note that there are two different side facets of the $\mathrm{Pd_{10}}$ clusters corresponding to {111} and {100} microfacets. The different adsorption energies at these facets roughly reflect the ordering of H and CO adsorption on the hollow adsorption sites on Pd(111) and Pd(100) (see section 2.2). It is obvious that CO adsorbs in a configuration that is locally perpendicular to the microfacets. The adsorption sites labeled (a) in Fig. 3.10 correspond to the local minima that one finds if one tries to put H and CO into the fourfold hollow position made from two Pd and two Au atoms at the edge of the

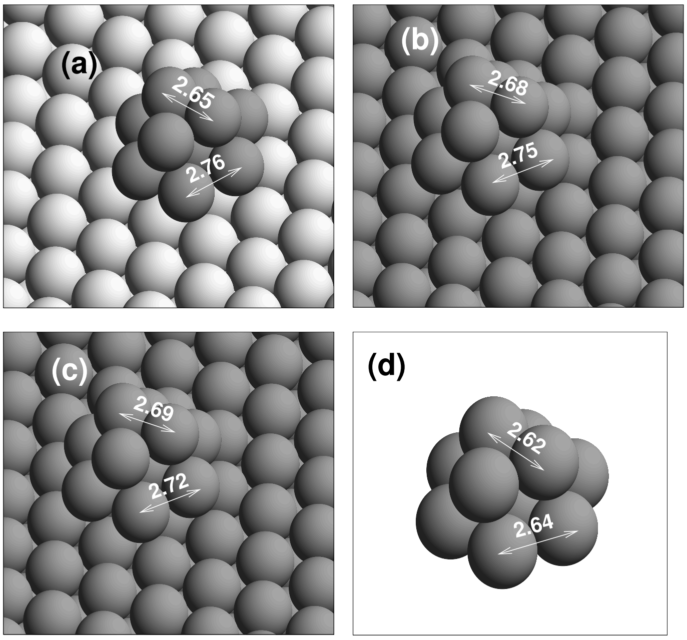

Figure 3.9: The structural relaxation of (a) Pd_{10} cluster supported by Au(111) substrate. (b) Pd_{10} cluster supported by Pd substrate with lateral lattice constant of Au (Pd_{10}/Pd@Au). (c) Pd_{10} cluster supported by Pd substrate. (d) free Pd_{10} cluster in gas phase.

cluster. The noble metal substrate Au is so inert that the adsorbates relax towards the Pd cluster atoms and end up in a quasi twofold bridge position.

In order to estimate the cluster-support interaction, in Fig. 3.10 we have also determined the adsorption energies on free Pd_{10} clusters in exactly the same geometry as the supported clusters (see the values in the parentheses). We labeled such clusters with free Pd_{10}^{*} cluster just in order to distinguish them from free relaxed geometry of Pd_{10} cluster. Hence the free Pd_{10}^{*} cluster is similar to free Pd_{10} cluster but with no relaxation. Note that the H and CO adsorption energy has been calculated with respect to a relaxed geometry of Pd_{10} cluster supported by Au, therefore the required energy to modify the position of the Pd atoms due to the adsorption has been taken into the account. The amount of this energy is considerable especially in the case of CO adsorption since the modification of atomic positions is large. In Fig 3.11 we have determined the adsorption energies on free Pd_{10}. As far as the adsorbates are concerned that mainly bind to the first layer Pd atoms, their binding energies on the free clusters are significantly larger, in particular for CO, than on the supported clusters and also on flat [99] and stepped Pd surfaces [90, 91]. This confirms that in spite of their compression free clusters are much more reactive than surfaces because of their low coordination. Thus it is the strong interaction of the three-dimensional Pd clusters with the Au support that contributes to the low adsorption energies on the metal-supported clusters. On oxide-supported clusters, on the other hand, the substrate-cluster interaction is much smaller so that the adsorption energies should be larger. Interestingly enough, at the top layer adsorption site the adsorbate binding energies on the free Pd_{10}^{*}

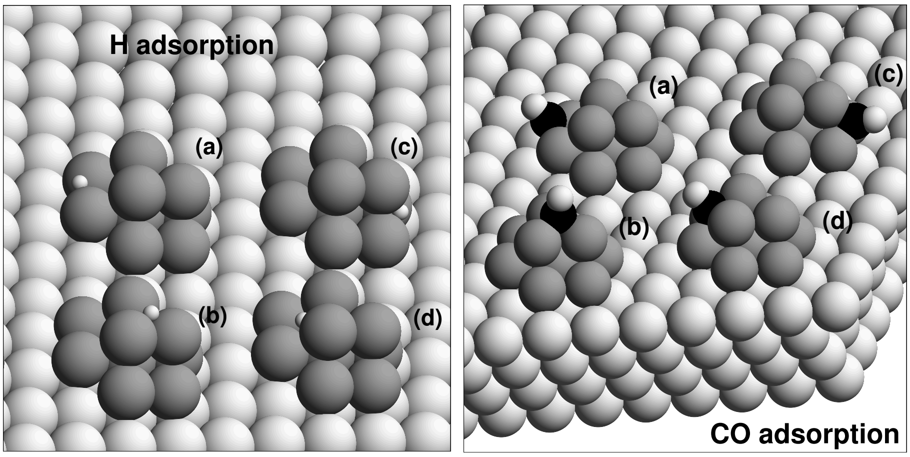

Structure	H adsorption energy (eV)	CO adsorption energy (eV)
a	-0.358 (-0.669)	-1.744 (-2.469)
b	-0.349 (-0.189)	-2.147 (-1.741)
c	-0.449 (-0.646)	-2.172 (-2.429)
d	-0.468 (-0.559)	-2.003 (-2.035)

Figure 3.10: Calculated H and CO adsorption energies on the $\mathrm{Pd_{10}}$/Au(111) cluster. The numbers in parentheses correspond to the adsorption energies on free $\mathrm{Pd_{10}}$ clusters in exactly the same configuration as the supported clusters.

and $\mathrm{Pd_{10}}$ clusters are smaller than on the supported cluster. This surprising result is caused by the reactivity of the unsaturated hexagonal bottom layer of the free $\mathrm{Pd_{10}}$ cluster. It binds the three topmost Pd atoms so strongly that the top layer becomes less reactive. An analysis of the the electronic structure of the free cluster shows that for $\mathrm{Pd_{10}}$/Au and free $\mathrm{Pd_{10}^*}$ the center of the *d*-band position are -1.37 eV and -1.43 eV respectively. The down-shift of the center of the *d*-band position due to higher interaction with the second layer causes a lower reactivity of the first layer of Pd. A very similar mechanism was obtained for $\mathrm{Pd_{10}}$/Pd@Au.

Just recently, a high hydrogen evolution rate has been found experimentally on Pd nanoparticles deposited on Au(111) using an electrochemical STM set-up [119]. The nanoparticles were, however, rather flat with a diameter to height ratio of about 5 - 10. The measurement of the reactivity is performed in four successive steps. After characterization of the Pd particle in the first step, in the second step the tip is positioned over the cluster. During the third step a potential pulse of typically 100 ms duration is applied to the electrode. The hydrogen oxidation current at the STM tip is measured using a digital storage oscilloscope. In the fourth step the current transient is recorded. The thinnest Pd particles with a height corresponding to two to three layers showed a hydrogen evolution rate that was about three orders of magnitude larger than the largest particles studied with a height of more than 10 monolayers. In a subsequent kinetic modeling the high hydrogen evolution rate could be explained under the assumption of a small desorption rate of hydrogen from the Pd particles [124]. Then the

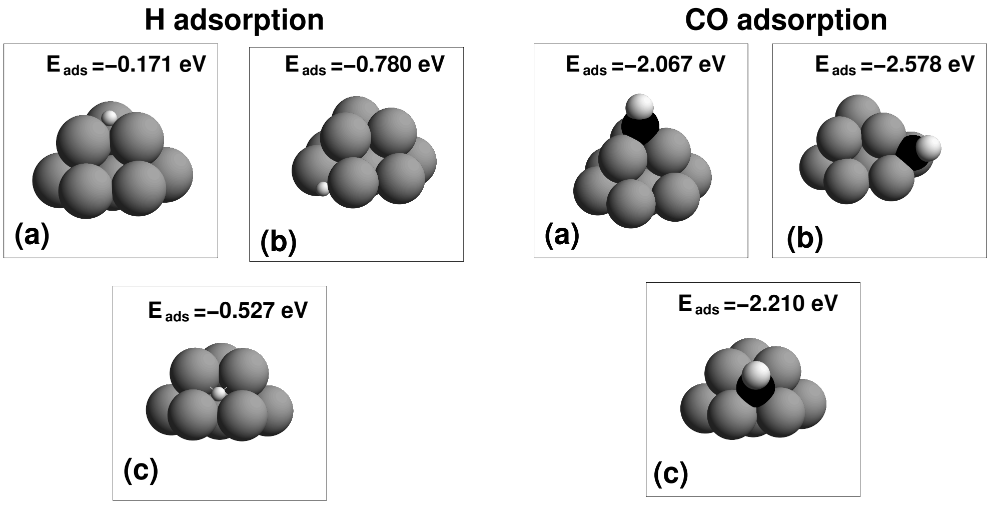

Figure 3.11: Calculated H and CO adsorption positions and energies on the free Pd_{10} cluster.

hydrogen atoms will spillover from the Pd particles to the Au substrate from where they will be released. The Pd particles thus represent an efficient hydrogen source.

We have found relatively small hydrogen binding energies on the three-dimensional Pd_{10} cluster. This would rather lead to a large desorption rate and therefore a low hydrogen evolution which can not describe the experiment. On the other hand, pseudomorphic Pd overlayer on Au(111) show a maximum hydrogen binding energy for two overlayers (see section 2.2) that is 0.2 eV larger than on flat Pd(111) and 0.3 eV larger than on the three-dimensional Pd_{10} clusters. At room temperature, these higher atomic binding energies lead to *associative* desorption rates that are reduced by at least six orders of magnitude. These findings suggest that the experiment has not probed properties of three-dimensional nanoparticles but rather of small islands that are locally pseudomorphic with the Au substrate, i.e. expanded by 5%.

We have checked that larger Pd islands will grow pseudomorphically on Au(111) by performing Pd/Au(111) overlayer calculations in a $\sqrt{7} \times \sqrt{7}$ surface unit cell. The calculation is simply classified as the following. A Pd/Au overlayer structure with $\sqrt{7} \times \sqrt{7}$ surface unit cell are modeled by a slab of five layers of Au. A displacement $\Delta l = 0.1$ Å have been applied on Pd atoms toward the center of the unit cell. In such a setup, contracted hexagonal Pd_7 cluster could form (see Fig. 3.12a). Regarding to our relaxation calculation we found however that they were not stable with respect to the pseudomorphic overlayer and the atomic positions return to their initial location (see Fig. 3.12b).

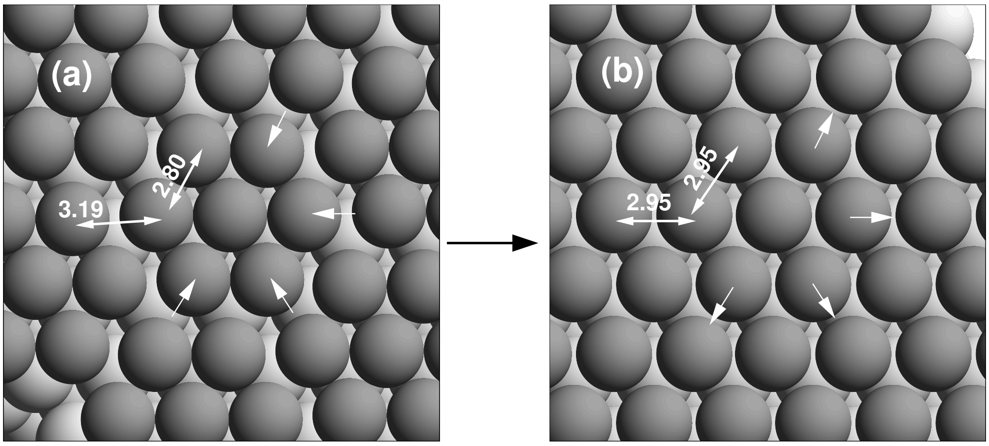

Figure 3.12: Pd overlayer on $(\sqrt{7} \times \sqrt{7})$ Au(111), (a) a $\Delta l = 0.1$ Å displacement has been applied on Pd atoms along the center of the unit cell. (b) relaxed structure geometry of Pd on $(\sqrt{7} \times \sqrt{7})$ Au(111).

Chapter 4

Local reactivity of a Pd/Au overlayer in the presence of water

Water is one of the most plentiful and essential compounds occurring in nature, which makes its interaction with metal surfaces of interest to various fields of science. Its particular relevance to heterogeneous catalysis, electrochemistry, and hydrogen production for fuel cells has prompted an enormous number of studies [127]. The ability of hydrogen to form an asymmetric pair of bonds to two neighboring atoms, an ordinary covalent bond with strength of several eV, and a weak hydrogen bond with strength of several tenth of an eV, plays a major role in determining the structure and room-temperature reactions of many substances, including water and biological molecules [128]. Nonetheless, our atomic level understanding of the structure and chemistry of water-metal interface remaines unclear.

Water adsorption on single crystalline surfaces of solids has been intensively investigated both experimentally and theoretically during the past few decades [129, 130]. On a number of metal surfaces, desorption of water usually leads to well-ordered structures such as one-dimensional (1D) chain [131], bilayer and islands and clusters [132]. Among these structures, the water bilayer with a $\sqrt{3} \times \sqrt{3}$ hexagonal pattern at 2/3 monolayer coverage is the mostly interesting one because it corresponds to the initial stage of the formation of 2D ice and the hydrogen bonded network [133]. The H_2O molecules on the metal surface arrange, as in ice I_h, in puckered hexagonal rings. The O atoms lie in two planes separated by about 1 Å. H atoms belonging to the lower-lying oxygens form H bonds with neighboring water molecules. The higher-lying O atoms contribute one H to the hexagonal H bonding network and one OH bond is oriented along the surface normal (see Fig. 4.1(a)). There is some evidence for bilayer formation on the noble metals and most of the late 3, 4, and 5d transition metals [129, 130].

One of the most intensively investigated system for adsorption of water on single-crystal surfaces is water on Ru{0001}. Until the low-energy electron refraction (LEED) study of Held and Menzel [134], water adsorption at low temperature (100-200K) on

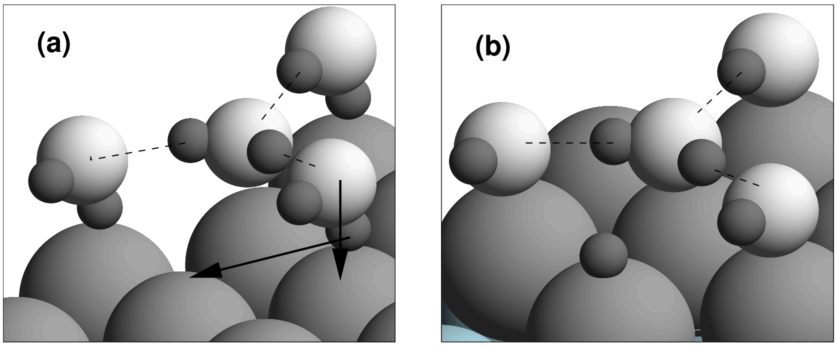

Figure 4.1: H_2O adsorption on Ru{0001} (a) before H dissociation, O atoms lie in two planes separated by 0.96 Å, dashed lines indicate the H bonds. (b) after H dissociation, the higher-lying O atoms move down and H shifted to on-top site.

Ru{0001} was thought to be relatively well understood. However, Held and Menzel's LEED structural analysis of D_2O adsorption revealed that, although the D_2O overlayers had $(\sqrt{3} \times \sqrt{3})$R30° periodicity, characteristic of an adsorbate bilayer, each plane of O atoms was not separated by 0.96 Å but instead by only 0.1 Å. Thus, it was proposed that a vertically compressed D_2O bilayer had been identified. D_2O was used in that study because slight bond length changes result in rather complicated long-range periodicity for H_2O overlayers [135]. However, similar LEED current versus voltage (I-V) curves were reported for H_2O and D_2O overlayers indicating that their local geometries are similar.

In 2002, Feibelman [136] performed a theoretical investigation of H_2O adsorption on Ru{0001} system and did not find a stable compressed H_2O bilayer with nearly coplanar oxygens. According to his density functional theory (DFT) calculations, O atoms lie in two planes separated by 0.96 Å. Both H atoms belonging to the lower-lying O atoms form H bonds to neighboring H_2O molecules, and the higher-lying H_2O molecules have one OH bond oriented along the surface normal and contribute one H atom to the H bonding network (see Fig. 4.1a). The higher-lying O atom do not bind directly to the metal at all, but only H bond to neighboring H_2O molecules. In the next step the H atom whose position is in between Ru and the higher-lying O atom is then dissociated from the O atom and located on-top site of Ru. Hence the water molecules in the bilayer are partially dissociated, with one OH bond broken (see Fig. 4.1b). This "partially dissociated" overlayer was about 0.2 eV/H_2O more stable than the buckled pure H_2O bilayer. Thus it was suggested that the wetting layer observed on Ru{0001} consisted of a half-dissociated hydroxyl-water overlayer. Feibelman's study provided compelling evidence for a partial dissociation model on Ru{0001}, and it has already inspired several experimental reinvestigation of this system. However, as pointed out by Menzel [137], difficulties with this new theoretical interpretation remain. A short time after Feibelman's article Meng *et al.* [133] performed a theoretical study of H_2O adsorption on Pt{111}. They also found a puckered hexagonal network as in the bulk ice on the Pt surface which was in agreement with Feibelman's study. But in this study both energies and vibrational dynamics indicate that on this surface intact H_2O

bilayers are stable compared to partially dissociated overlayers. The difference between H_2O on Ru and on Pt is due to the fact that Pt binds water much more weakly than Pt. They found that the most stable structure is related to the un-hydrogen-bonded H atom pointed either upward or to the surface. These two structures are nearly degenerate in energy. This foundation is in agreement with ultraviolet photoemission spectroscopy [138] and low energy electron diffraction (LEED) measurement [139, 140].

In low-temperature fuel cells where H_2 is used as a fuel for the reaction H_2 and O_2 to produce electrical energy, the presence of liquid water is a necessity for the membrane to function efficiently. This limits the temperature range in which it can be operated to 60-100°C [141]. The H_2 used as fuel is usually produced from natural gas or from methanol (CH_3OH) or other liquid fuels by stationary or on-board reformer systems. CO is a byproduct of such a process and it is very hard to avoid 10-100 ppm of CO in the feed gas. The low temperature of operation puts strong limits on the purity of the fuel. As little as approximately 20 ppm of CO in the H_2 severely poisons the catalyst surface, specially a pure Pt catalyst surface [141]. Various Pt-based alloys have been proposed to alleviate this problem. One of the current standard solution is to use a alloy catalyst. Several alloys have been proposed to be considerably more CO tolerant than pure Pt, i.e. PtRu, PtFe, PtNi, PtCo and PtMo alloys show good CO resistance [142, 143]. The surfaces of these alloys were shown to consist of a thin layer of Pt with an electronic structure different from pure Pt. There are two possible ways in which alloying could change the sensibility of H_2 oxidation [141]. One is that, i.e. Ru promotes CO oxidation, thus removing CO from the surface [142]. The other possibility is that alloying decreases the CO stability more than the stability of H on the surface.

In 2001 Chrisoffersen *et al.* [144] performed ab-initio DFT calculations to discuss why a few parts per million of CO in the H_2 fuel can poison Pt surfaces and how this problem can be alleviated by alloying. They initiated the discussion by introducing a simple model of the kinetics of proton formation at a metal surface in the presence of H_2 and CO in the gas phase. The main parameter controlling the effect of CO on the kinetics are the CO and H_2 adsorption energies. They show that in order to decrease the CO coverage on the surface, the coverage of adsorbed H atoms on the surface, θ_{H} must be increased. θ_{H} is given mainly by the difference in the H and CO adsorption energy. On the other hand in an electrochemical cell the presence of the electrolyte i.e. water as well as the cell voltage affects the H and CO adsorption energies [48]. The values of H and CO adsorption energies have been measured and calculated for several transition metals, i.e. Pt. However there is no theoretical study in which it is shown how the presence of a water adlayer will influence these values. Therefore in this chapter we present a computational study of submonolayer water on a substrate monolayer to find out the modification of the adsorption energy due to the presence of water. In order to be able to compare our results with the results in chapter 2 for the clean surface, we have chosen one Pd overlayer on an Au(111) surface. The outline of this chapter is the following. In order to use the right pseudopotential which can represent the true behaviour of H-bond, we have performed calculations for the water monomer, dimer and ice I_{h} with the ultrasoft pseudopotential (USP) and the Projector Augmented Wave (PAW) method. We have shown that although PAW turns out to be in better agreement with experimental values, USP is also good enough to be used in our system. In addition, since all calculations for the adsorption energies on clean surfaces have been performed with USP here we also used USP in order to have a identical computational setup for a fair comparison. In section 4.2.2 we will identify a 2/3 monolayer coverage of water as the most stable water coverage. For this coverage we have also calculated the most stable water configuration on the metal surface. Finally in section 4.3 we have determined the H and CO adsorption energies for a $\sqrt{3} \times \sqrt{3}$ unit cell and 2/3 monolayer coverage of water and compared them to the energy values of section 2.

4.1 Computational method

All calculation presented in this chapter were again performed using the Vienna *ab initio* simulation package (VASP) with the PW91 generalized gradient approximation. Choosing a right pseudopotential is very important to present the true hydrogen bonds in the water. While Feibelman [136] compared the experimental values of sublimation energy of ice I_h with both pseudopotentials and used the PAW pseudopotential with a cutoff energy of 700 eV for water adsorption on Ru{0001}, Meng *et al.* [133] used a USP with a cutoff energy of 300 eV with the PW91 functional for water adsorption on Pt(111). Here we have also tested both pseudopotentials for water monomer, dimer and ice I_h and compare them with experimental values to find out which type of these pseudopotentials will better represent the true properties of water. The valence states were expanded in a basis of plane waves with kinetic energies up to 400 eV and 700 eV for USP and PAW pseudopotentials respectively. The overlayer structure has been modeled by a slab of four layers of Au on which one Pd overlayer has been deposited. All layer structures are separated by at least 10.5 Å of vacuum. The three bottom layers of the slabs were kept fixed at their corresponding bulk positions, while all upper layers including the overlayers have been fully relaxed such that the forces on each atom were below 0.02 eV/Å. Geometrical relaxations were carried out using the Hellman-Feynman forces and a conjugate-gradient minimization scheme. The surface Brillouin zone of the Pd/Au system is sampled by a Monkhorst-Pack **k**-point set of 3×3×1, 7×7×1 and 9×9×1 for the 3×3, 2×2 and $\sqrt{3} \times \sqrt{3}$ unit cell, corresponding to 5, 25 and 41 **k**-points in the irreducible Brillouin zone respectively. A Methfessel-Paxton smearing of σ=0.2 eV has been used in order to get a faster convergence of the electronic structure calculation.

In Table 4.1 the structural properties of the water monomer and the dimer are summarized and compared to the experimental values. The geometrical structure of the water monomer and water dimer with both pseudopotentials is in good agreement with experiment. In Table 4.2 in order to check both pseudopotentials more carefully the structural properties of ice I_h as well as the ice-sublimation energy for both pseudopotentials are calculated and compared to the experimental values. The ice structure used in the calculations consist of 32 molecules of water which are arranged according to the Bernard-Fowler rule. Although the results from PAW indicates a better agreement with experimental values, there is no dramatic difference between PAW and USP

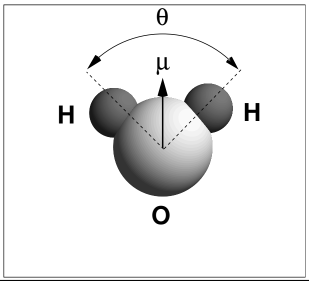

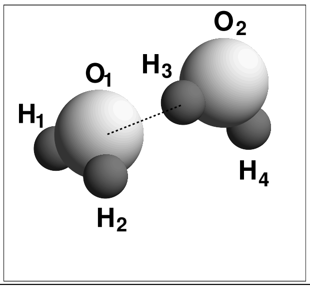

	monomer			dimer				
	d_{OH}	θ	μ (D)	d_{OO}	θ_a	θ_b	E_{H-bond}	μ (D)
USP	0.97	103.5	1.853	2.88	106.3	1.3	-0.246	2.200
PAW	0.97	104.1	1.835	2.90	105.3	1.8	-0.242	2.060
Exp	0.96	104.5	1.855	2.98	123±10	6±20	-0.236±0.03	2.600

Table 4.1: The structural properties of a water molecule and water dimer calculated with USP and PAW pseudopotential and a comparison with experimental values. θ_a and θ_b are angles $O_1 - O_2 - H_3$ and $H_1 - O_1 - H_2$ respectively (see the figure above)

	Vol ($Å^3$)/H_2O	E_{sub} (eV)	B_0 (GPa)
USP	30.14	-0.712	15.38
PAW	30.35	-0.666	14.46
Exp	32.05	-0.580	10.9

Table 4.2: The equilibrium volume, sublimation energy and bulk modulus of 32 molecule of water in ice I_h structure calculated with USP and PAW pseudopotentials

results. We are interested in the comparison of the H and CO adsorption energies in the presence of water with adsorption energies of clean surface. We have calculated the adsorption energies of H and CO on clean surface with USP pseudopotential (see section 2.2). In this chapter USP has been used to have an identical computational setup and an identical condition for comparing the adsorption energies in the two different cases.

4.2 Water adsorption on Pd/Au overlayer surface

4.2.1 Water monomer and dimmer

The optimized geometries for the water monomer and dimer on Pd/Au(111) are schematically shown in Fig 4.2 and further specified in Table 4.3. For the monomer the adsorption on top site is more favored than the bridge or hollow sites. The difference in the adsorption energies between on-top site and other sites is about 170 meV. Water lies nearly flat on the surface with the polar axis making a angle of 81° from the surface normal. The molecule can rotate freely in the azimuthal angle without any noticeable barrier. The H-O distance does not change upon adsorption, however the H-O-H angle changes only 2° with respect to the monomer in the gas phase.

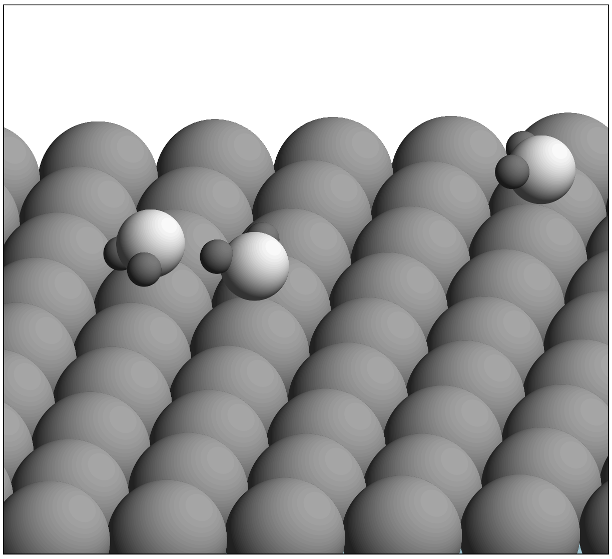

Figure 4.2: Relaxation geometry of water monomer (right) and water dimer (left) adsorption on Pd/Au overlayer surface.

For the dimer case, both molecules prefers to stay on-top sites. The structural form of the dimer is very close to the dimer in the gas phase except for the fact that the unhydrogen bonded of the donor molecule is lying down to the surface. The O-O distance gets shorter by 0.16 Å compared to the dimer in the gas phase. The adsorption energy of the dimer on the substrate given in Table 4.3 is obtained by the following formula,

$$\mathrm{E_{ads}} = \frac{1}{\mathrm{N}}(\mathrm{E_{slab+H_2O}} - \mathrm{E_{slab}} - \mathrm{NE_{H_2O}}) \tag{4.1}$$

where N is the number of water molecules and $\mathrm{E_{ads}}$ is the water adsorption energy per water molecule which consists of two parts: The first part is the energy of the hydrogen bond between two water molecules in the dimer and the second part is the energy gain due to the interaction with the metal surface. If we assume that the water-metal interaction energy gain in the case of the dimer is equal to the energy gain of water-metal in the monomer then we can derive the hydrogen bond energy after the adsorption on the metal surface case and compare it to the gas phase. The equation to calculate the H-bond energy is given by:

$$\begin{aligned}\mathrm{E_{H-bond}} &= (\mathrm{E_{ads}}[\mathrm{dimer}] - \mathrm{E_{ads}}[\mathrm{monomer}]) \times 2 \\ &= (-0.422 - 0.316) \times 2 = -0.212 \text{ eV}\end{aligned} \tag{4.2}$$

The hydrogen bond energy after adsorption shows a lower value than the hydrogen bond in gas phase ($\mathrm{E^{gas}_{dimer}}$=-0.246 eV). This shows a opposite trend to the water adsorption on Pt(111) [133].

	$Z_{\mathrm{O-O}}$	$Z_{\mathrm{O-Pd_1}}$	$Z_{\mathrm{O-Pd_2}}$	$E_{ads}(eV/\mathrm{H_2O})$	d_{O-H} (hydrogen bond)
Monomer	—	2.46	—	-0.316	—
Dimer	0.58	2.27	2.95	-0.427	1.72

Table 4.3: The geometries and energies for water monomer, dimer on Pd/Au(111) overlayer. Z_{OO}, $Z_{\mathrm{O-Pd_1}}$, and $Z_{\mathrm{O-Pd_2}}$ are the vertical distances between the top and bottom O atoms, the bottom O and Pd, and the top O and Pd respectively. d$_{O-H}$ is the O-H distance which represents a hydrogen bond

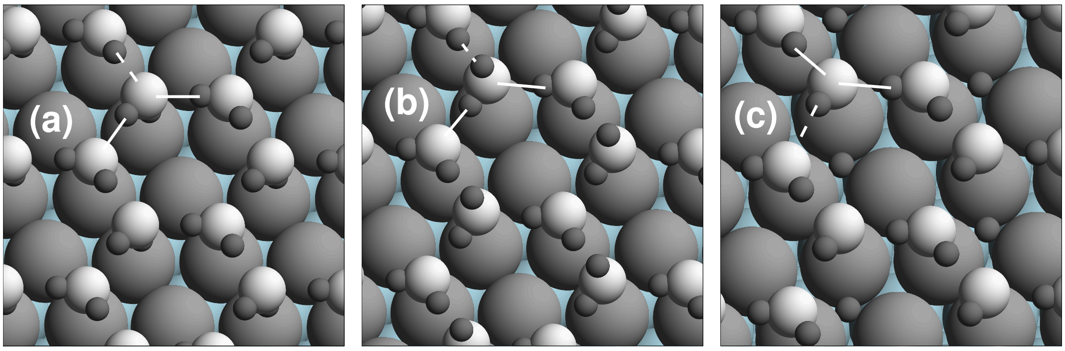

Figure 4.3: Different water structures for coverage θ=2/3 on a Pd/Au(111) overlayer. (a) H-down bilayer, (b) H-up bilayer, (c) half-dissociated bilayer. Solid lines indicate the H-bond with a shorter H-bond length while dash lines indicate the H-bond with a longer H-bond length.

4.2.2 Water adsorption energy for different water coverages

The calculated water adsorption energies as a function of water coverage are listed below in Table 4.4. For coverage θ =1/4, 1/2, 1, 3/4, a 2×2 unit cell was used. While for coverage θ = 1/3, 2/3, a $\sqrt{3} \times \sqrt{3}$ unit cell was chosen. According to the values in Table: 4.4, the coverage θ=2/3 structure corresponds to the higher absorption energy compared to the other coverages. For this coverage, the water molecules form a puckered hexagonal network as observed in the case of the bulk ice [145]. However, it was observed in our instance that the unhydrogen H-bond points either up-wards [H-up bilayer case, Fig. 4.3(a)] or toward the surface [H-down bilayer case, Fig. 4.3(b)] or hydrogen half-dissociated [half-dissociated bilayer case, Fig. 4.3(c)]. The solid and dash lines in Fig 4.3(a-c) indicate the H-bond with shorter and longer distances respectively.

Table 4.4 also indicates that, the H-down bilayer structure is the most stable than the half-dissociated bilayer by about 0.2 eV per water molecule. This determination

θ:	1/4	1/3	1/2	1	3/4	2/3(a)	2/3(b)	2/3(c)
E_{ads}:	-0.308	-0.295	-0.419	3.135	-0.465	-0.528	-0.499	-0.327

Table 4.4: H_2O adsorption energies in eV/H_2O as a function of H_2O coverages. The energies were obtained using ultrasoft pseudopotentials. For the notation of the structures at a water coverage of $\theta_{\mathrm{H_2O}} = 2/3$, see Fig. 4.3.

structure	E_{ads}(eV/H_2O)	H-bond length (Å)
Pd/Au	-0.536	1.95
Pd/Pd@Au	-0.520	1.95
Pd	-0.552	1.84

Table 4.5: Water adsorption energy values on Pd/Au, Pd with lateral lattice constant of Au (Pd@Au) and pure Pd for coverage θ=2/3 and H-down bilayer.

rules out the possibility that the that the partial dissociation of water on Pd/Au(111) is stable. However, it should be noted that the calculated sublimation energy of water in a "32-molecules per cell" model of ice-Ih, $E_{sub} = -0.712$ eV (USP) and $E_{sub} = -0.666$ eV (PAW), is more negative than all calculated water adsorption energies on Pd/Au(111) as represented in table 4.4 (see also Ref. [136]). This would mean that the considered water adlayers are not thermodynamically stable with respect to a three-dimensional ice cluster. The reason is that the lateral lattice constant of the pseudomorphic Pd/Au(111) overlayer is too large compared to the water-water distance in ice. In order to find a stable water adlayer structure, larger surface unit cells have to be considered such as $\sqrt{37} \times \sqrt{37}$ or $\sqrt{39} \times \sqrt{39}$, as observed in the case of water on Pt(111) [146, 147]. Since we are mainly concerned with the influence of water on the hydrogen adsorption energies, we did not pursue this issue in more detail.

Table 4.5 shows a comparison of the water adsorption energy for coverage θ=2/3, H-down bilayer on Pd/Au(111) with the pure Pd(111) and Pd with lateral lattice constant of Au. Our calculations show that the water adsorption energy for pure Pd is larger than that of Pd with lateral constant of Au. This confirms that the lateral lattice constant of the pseudomorphic Pd/Au(111) overlayer is too large. Therefore in spite of a reduction of the Pd lattice constant from Pd@Au (4.18 Å) to Pd (3.96 Å) leads to a shift on the d-band center (see section 2.3.1) and hence, we expect that the water-metal interaction energy decreases. On the other hand it also causes a reduction of the H-bond length and hence an increase of H-bond energy which over compensates the reduction of the interaction of water with Pd due to the shift of the d-band center.

4.3 Hydrogen and CO adsorption energies

The hydrogen and CO adsorption energies on Pd/Au(111) overlayer system for different high symmetry sites in the presence of water with both H-up and H-down bilayer are summarized in Table 4.6 and compared to that of a clean surface. The calculation with H-up and H-down bilayer are indicated by $E_{ads}[H_2O]_\uparrow$ and $E_{ads}[H_2O]_\downarrow$ respectively. Due to the presence of the water there is a symmetry breaking between fcc and hcp sites. The fcc and hcp sites split out to fcc(a), fcc(b) and hcp(a), hcp(b) respectively. (see Fig. 4.4(a-b)). The fcc(a) and hcp(a) sites show a higher binding energies compared to the fcc(b) and hcp(b) sites. This indicates that there is a interaction between the adsorbate and one of the hydrogen atoms in the H_2O hexagonal ring. However, the difference in the energy between the two different fcc (hcp) sites is only 28 (20) meV. For hydrogen adsorption the most stable structure is the three fold fcc(a) with the

	H adsorption energies		
	$E_{ads}[H_2O]_\downarrow$	$E_{ads}[H_2O]_\uparrow$	$E_{ads}[Clean]$
Fcc	-0.661	-0.660	-0.690
Hcp	-0.596	-0.595	-0.655
On-top	0.155	—	0.075
	CO adsorption energies		
Fcc	-1.831^{2D} -1.457^{3D}	-1.894	-2.023
Hcp	-1.866	-1.923	-2.043
On-top	-1.243	-1.317	-1.413

Table 4.6: Hydrogen and CO adsorption energy. $E_{ads}[H_2O]_\downarrow$ and $E_{ads}[H_2O]_\uparrow$ indicate the adsorption energy with H-down and H-up bilayer structure of water respectively. E_{ads}[Clean] indicates the adsorption energy of the clean surface. The superscript 2D and 3D indicate the CO adsorption energy on three fold fcc site in presence of a two-dimensions and three-dimensions bilayer respectively (see Fig. 4.5).

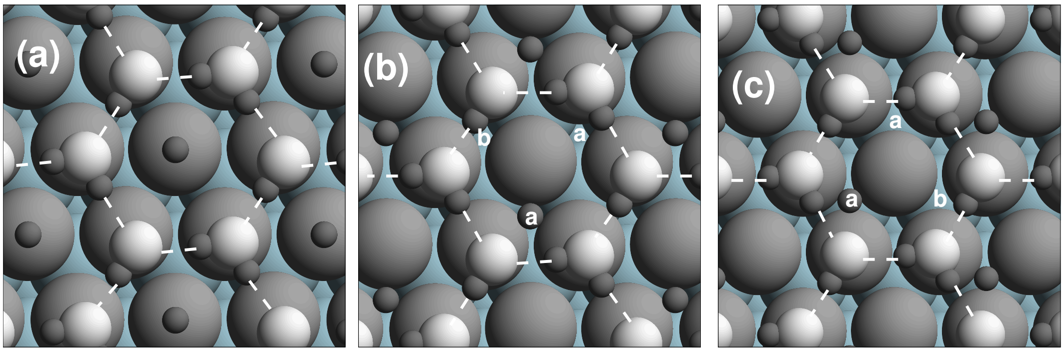

Figure 4.4: Top-view of the geometrical relaxation of the hydrogen adsorption on Pd/Au(111) overlayer in presence of a water bilayer for, (a) on-top site, (b) fcc(a) site, (c) hcp(a) site. Due to the presence of the water bilayer the fcc sites are energetically different. fcc(a) and hcp(a) are energetically more favorable compare to fcc(b) and hcp(b) respectively.

H-down bilayer as indicated in Table 4.6.

Water has two very polar covalent bonds between oxygen and hydrogen. Because water is bent (the oxygen atom is sp3 hybridized), the two bond dipole moments add up to give water a relatively large molecular dipole moment (see Table 4.1). Our calculation indicate that the only difference between H-down and H-up bilayers on a surface metal is a change of the direction of the water dipole moment. Hence a comparison between adsorption energies on the H-down and H-up bilayer represents the dipole-dipole interaction between the water molecules and adsorbate. Therefore we compared the hydrogen and CO adsorption energy for a H-down bilayer with a H-up bilayer in Table 4.1. The values of the energies were modified only by 0.001-0.005 meV and 0.057-0.075 eV for hydrogen and CO adsorption respectively. Thereby indicating that the dipole-dipole interactions are very small for the case of hydrogen

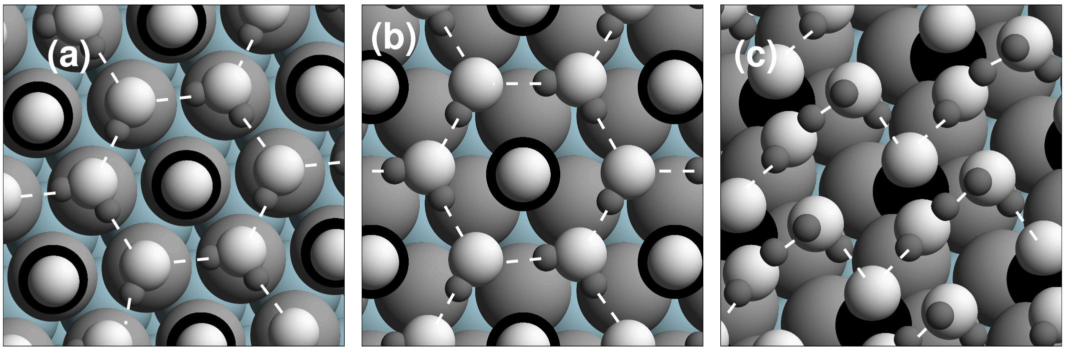

Figure 4.5: Top-view of CO adsorption on Pd/Au(111) overlayer in presence of a water bilayer for, (a) on-top site, (b) fcc hollow site with a shifted water bilayer, (c) fcc hollow site with a three-dimensions water bilayer. The carbon atoms are represented as black spheres

adsorption. The dipole-dipole interaction appears to be more significant for the case of CO adsorption due to the large CO dipole moment and the short CO-water distances.

Table 4.1 shows a comparison of the hydrogen adsorption energies at the threefold hollow sites of Pd/Au(111) in the presence of different water adlayer structures to that of the clean surface (E_{ads}[Clean]). The most important issue is that the change of the hydrogen adsorption energies for most water structure is observed to be below 100 meV. For the most stable water structure, the H-down bilayer, the changes are below 60 meV which is about 10% of the atomic hydrogen adsorption energy. This can be attributed to the relatively weak binding of water to Pd/Au(111) which does not significantly perturb the electronic structure of the substrate and thus does also not effect the hydrogen-substrate bond too much. The polar water molecules induce an additional electric field at the surface which have a small influence on the hydrogen bonding.

In Table 4.6 we have also summarized the CO adsorption energies at high-symmetry sites in the presence of water. Firstly the relaxed CO molecular height is relatively high above the metal surface. This relaxed CO adsorption height is almost at the same height as the height of the water molecules. Thereby indicating a strong interaction between CO and the water molecules. This is supported by the fact that the distances between the molecules are short. The ionic relaxation in this instance will be very difficult. However, CO adsorption on-top site in the presence of the water bilayer is an exceptional case because CO molecules are located in the center of the water hexagonal ring and hence the CO-H_2O distances become relatively large and ionic relaxation can be done with no difficulty. A top-view of the CO adsorption on the Pd/Au(111) overlayer for the on-top site in the presence of an H-down bilayer is shown in Fig. 4.5(a). For the other sites i.e. the fcc site the CO-metal interaction is strong. Therefore a relaxation calculation with CO and a coverage of θ=1/3 of water on the metal surface was performed. In the next step another water molecule was added to our system to calculate the final relaxed atomic positions. The result of such a relaxation is a three-dimensional water adsorption. The geometrical relaxation is shown in Fig 4.5(c). The CO adsorption energy in this case is -1.457 eV with respect to the most stable water structure. In another approach, we performed an ionic relaxation of the water adsorption in the absence of CO with a shift of all water molecules in the same direction so that the center of the hexagonal ring shifted on the site of interest for the calculate of the adsorption energy. The modification on the energy due to the shift on the center of the hexagonal water ring is calculated as 80 meV. The relaxed structure of CO adsorption in fcc site with H-down bilayer is shown in Fig 4.5(b). The value of the adsorption energy is -1.831 eV which shows a more stable structure compared to the last instance cited in Table 4.6.

For CO adsorption in the presence of water the most favorable site is the three fold hcp site with a H-down shifted bilayer. For the clean Pd/Au(111) surface it was seen that the three-fold hcp site is the most favorable site for CO adsorption. The modification of the CO adsorption energy due to the presence of the water adlayer is 170 - 200 meV which is about 10% of the CO adsorption energy. The reason for this relatively small change can be explained by the small water-metal interaction which does not significantly perturb the electronic structure of the substrate. The slight modification of the hydrogen and CO adsorption energies by the presence of a water adlayer suggests that theoretical studies of hydrogen and CO adsorption on clean metal surfaces are also qualitatively and semi-quantitatively meaningful for the specific hydrogen adsorption in electrochemistry.

Chapter 5

Conclusions

We have studied the adsorption of atomic hydrogen and molecular CO on structured surfaces. Our focus was on two different systems, namely the adsorption on Pd/Au overlayer in the presence and absence of water and Pd_n clusters supported by Au(111) with different Pd cluster size.

In chapter 2, we have presented DFT calculations for the adsorption of atomic hydrogen and CO at the high-symmetry positions of thin pseudomorphic Pd films deposited on Au(111) and Au(100). In general, we find that both the lattice expansion of the pseudomorphic Pd films by 5% as well as the interaction of the Pd films with the Au substrate lead to a higher reactivity of the overlayers. Most of our results can be rationalized by the *d*-band model, which means that there is a direct correlation between the center of the *d*-band and the reactivity. However, additionally bond length and second nearest neighbor interaction effects contribute to the reactivity. The indirect interaction of the adsorbates with the inert Au substrate leads to a maximum in the binding energies for two Pd overlayers on Au on all adsorption sites that we considered. Furthermore, we find that the *d*-band model is no longer fully appropriate in the case of a strong coupling between adsorbate and substrate.

Our results explain the dependence of the reactivity of flat Pd nanoparticles on Au(111) on the particle height found experimentally by using an electrochemical STM set-up [119]. The highest reactivity was obtained for the thinnest Pd particles studied which had a height corresponding to two to three layers. We conclude that their high electrochemical reactivity is a consequence of the combination of substrate interaction and lattice strain effects. Still it should be noted that we have treated perfectly flat surfaces in the absence of any electrolyte. Hence our results are only meaningful as far as general trends are concerned. For example, according to the DFT calculations, Pd is more strongly bound to a Pd(111) substrate by 0.1 eV compared to an Au(111) substrate. This is at variance with the experimentally well-established fact of an upd layer of Pd on Au(111). Our results therefore suggest that the Pd-Au interaction is modified by the presence of an electrolyte.

Furthermore we have calculated atomic hydrogen adsorption energies on Pd/Cu(111) and Cu/Pd(111) as another example in order to understand the lattice mismatch and substrate effects. Due to the strong interaction between Pd and Cu, both overlayer systems show intermediate properties between clean Pd(111) and Cu(111). Still, the modification of the Pd/Cu(111) overlayer with respect to pure Pd(111) is more pronounced since adsorption energies show a stronger strain dependence on Pd than on Cu.

In chapter 3, we have calculated the adsorption energies of hydrogen atoms and CO on small supported Pd_n/Au(111) clusters as a probe of the local reactivity. We find that the H and CO adsorption energies on the supported clusters are determined by a combination of coordination, relaxation and support interaction effects. Due to the reduced interatomic distances and the strong interaction with the Au substrate, the adsorption energies on the three-dimensional supported Pd cluster are less than on corresponding pseudomorphic Pd overlayers. However, an experimental study on Pd clusters on Au by STM to measure the hydrogen evolution from the Pd cluster, shows the highest hydrogen evolution for Pd cluster with two to three layers. The high hydrogen evolution could be explained under the assumption of a small desorption rate of hydrogen from the Pd particles. We have found relatively small hydrogen binding energies on the three-dimensional Pd_{10} cluster. This would rather lead to a large desorption rate. On the other hand, pseudomorphic Pd overlayer on Au(111) show a maximum hydrogen binding energy for two overlayers that is 0.2 eV larger than on flat Pd(111) and 0.3 eV larger than on the three-dimensional Pd_{10} clusters. At room temperature, these higher atomic binding energies lead to *associative* desorption rates that are reduced by at least six orders of magnitude. These findings suggest that the experiment has not probed properties of three-dimensional nanoparticles but rather of small islands that are locally pseudomorphic with the Au substrate, i.e. expanded by 5%. We have checked that larger Pd islands will grow pseudomorphically on Au(111) by performing Pd/Au(111) overlayer calculations in a $\sqrt{7} \times \sqrt{7}$ surface unit cell. In such a setup, contracted hexagonal Pd_7 cluster could form. However, we found that they were not stable with respect to the pseudomorphic overlayer.

In chapter 4, we have studied the influence of the presence of a water adlayer on the hydrogen adsorption energy on Pd/Au(111). We found that a two-dimension hexagonal ice-like structure with a converge at 2/3 monolayer of water is the most stable water structure on Pd/Au(111) surface. For coverage θ=2/3 we checked different water structures i.e. H-down, H-up and half dissociated bilayer. We found a H-down bilayer as the most stable water structure. Our calculation concerning H and CO adsorption on the surface in the presence of water shows that due to the relatively weak interaction of water with the Pd/Au(111) substrate, the binding energies of hydrogen and CO are reduced by less than 50 meV (5% of H adsorption) and 200 meV (10% of CO adsorption energy) respectively. This suggests that hydrogen and CO adsorption studies at the solid-vacuum interface are also relevant for the interpretation of specific hydrogen adsorption at the solid-liquid interface. In addition we found that the modification of H and CO adsorption energies due to the interaction between water molecules and adsorbates are less than 5 meV and 80 meV respectively.

Bibliography

[1] M. Born and K Huang. *Dynamical Theory of Crystal Lattices.* Clarendon Press, Oxford, 1954.

[2] W. Kohn and L.J. Sham. Self-consistent equations including exchange and correlation effects. *Phys. Rev.*, 140:A1133, 1965.

[3] P. Hohenberg and W. Kohn. Inhomogeneous electron gas. *Phys. Rev.*, 136:B864, 1964.

[4] W. E. Pickett. Pseudo potential methods in condensed matter applications. *Computer phys. reports*, 9:115, 1989.

[5] Reiner M. Dreizler and Eberhard K. U. Gross. *Density Functional Theory: An Approach to the Quantum Many-Body Problem.* Springer, 1990.

[6] S. Lundqvist and N. H. March. Plenum, New York, 1983.

[7] R. O. Jones and O. Gunnarsson. The density functional formalism, its applications and prospects. *Rev. Mod. Phys.*, 61:689, 1989.

[8] P. A. M. Dirac. Note on exchange phenomena in the thomas atom. *Proccedings of the Cambridge Philosophical Society*, 26:376, 1930.

[9] D. M. Ceperley and B. J. Alder. Ground state of the electron gas by a stochastic method. *Phys. Rev. Lett.*, 45:566, 1980.

[10] G. R. Parr and W. Yang. *ensity Functional Theory of Atoms and Molecules.* Oxford University Press, 1989.

[11] Kari Laasonen, Alfredo Pasquarello, Roberto Car, Changyol Lee, and David Vanderbilt. Car-Parrinello molecular dynamics with Vanderbilt ultrasoft pseudopotentials. *Phys. Rev. B*, 47:10142, 1993.

[12] C. S. Wang, B. M. Klein, and H. Krakauer. Theory of magnetic and structural ordering in iron. *Phys. Rev. Lett.*, 54:1852, 1985.

[13] L. J. Sham. Plenum, New York, 1971.

[14] E. K. U. Gross and R. M. Dreizler. Gradient expansion of the coulomb exchange energy. *Zeitschrift der Physik A*, 302:103, 1981.

[15] K. Bruke, J. P. Perdew, and M. Levy. *Nonlocal Density Functional for Exchange and Correlation: Theory and Application, in Density Functional Theory: A tool*

for Chemistry. Elsevier, Amesterdam, 1995.

[16] F. Herman, J. P. van Dyke, and I. B. Ortenburger. mproved statistical exchange approximation for inhomogeneous many-electron systems. *Phys. Rev. Lett.*, 22: 807, 1969.

[17] John P. Perdew, J. A. Chevary, S. H. Vosko, Koblar A. Jackson, Mark R. Pederson, D. J. Singh, and Carlos Fiolhais. Atoms, molecules, solids, and surfaces: Applications of the generalized gradient approximation for exchange and correlation. *Phys. Rev. B*, 46:6671, 1992.

[18] S. H. Vosko, L. Wilk, and M. Nusair. Accurate spin-dependent electron liquid correlation energies for local spin-density calculations - a critical analysis. *CANADIAN JOURNAL OF PHYSICS*, 58:1200, 1980.

[19] J. P. Perdew and A. Zunger. Self-interaction correction to density-functional approximations for many-electron systems. *Physical Review B*, 23:5048, 1981.

[20] M. Tinkham. *Group Theory and Quantum Mechanics.* McGraw-Hill, New York, 1964.

[21] Hendrik J. Monkhorst and James D. Pack. Special points for Brillouin-zone integrations. *Phys. Rev. B*, 13:5188, 1976.

[22] R. Car and M. Parrinello. Unified approach for molecular dynamics and density-functional theory. *Phys. Rev. Lett.*, 55:2471, 1985.

[23] D. K. Rembler and P. A. Madden. *Molecular Physics*, 70:921, 1990.

[24] P. Pulay. *Molecular Physics*, 197, 1969.

[25] D. R. Hamann, M. Schlüter, and C. Chiang. Norm-conserving pseudopotentials. *Phys. Rev. Lett.*, 43:1494, 1979.

[26] G. B. Bachelet, D. R. Hamann, M. Schlüter, and C. Chiang. Pseudopotentials that work: From h to pu. *Phys. Rev. B*, 26:4199, 1982.

[27] L. Kleinman and D. Bylander.

[28] G. P. Kerker. *Journal of Physics C*, 13:L189, 1980.

[29] David Vanderbilt. *Phys. Rev. B*, 32:8412, 1985.

[30] Andrew M. Rappe, Karin M. Rabe, Efthimios Kaxiras, and J. D. Joannopoulos. Optimized pseudopotentials. *Phys. Rev. B*, 41:1227, 1990.

[31] N. Troullier and J. L. Martins. Efficient pseudopotentials for plane-wave calculations. *Phys. Rev. B*, 43:1993, 1991.

[32] David Vanderbilt. Soft self-consistent pseudopotentials in a generalized eigenvalue formalism. *Phys. Rev. B*, 41:7892, 1990.

[33] Peter E. Blöchl, O. Jepsen, and O. K. Andersen. Improved tetrahedron method for Brillouin-zone integration. *Phys. Rev. B*, 49:16223, 1994.

[34] N. D. Mermin. *Phys. Rev.*, 137:A 1441, 1965.

[35] C.-L. Fu and K.-M. Ho. First-principles calculation of the equilibrium ground-state properties of transition metals: Applications to nb and mo. *Phys. Rev. B*, 28:5480, 1983.

[36] M. Weinert and J. W. Davenport. *Physical Review B*, 45:13709, 1992.

[37] R. M. Wentzcovitch, J. L. Martins, and P. B. Allen. *Physical Review B*, 45:11372, 1992.

[38] M. J. De Vita, Gillan. *Journal of Physics: Condensed matter*, 3:6225, 1991.

[39] M. Methfessel and A. T. Paxton. High-precision sampling for Brillouin-zone integration in metals. *Phys. Rev. B*, 40:3616, 1989.

[40] R. Hoffmann. A chemical and theoretical way to look at bonding on surfaces. *Rev. Mod. Phys.*, 60:601, 1988.

[41] M. Scheffler and C. Stampfl. Theory of adsorption on metal substrates. In K. Horn and M. Scheffler, editors, *Electronic Structure*, volume 2 of *Handbook of Surface Science*, pages 286–356. Elsevier, Amsterdam, 2000.

[42] B. Hammer and M. Scheffler. Local chemical reactivity of a metal alloy surface. *Phys. Rev. Lett.*, 74:3487, 1995.

[43] A. Eichler, J. Hafner, and G. Kresse. Hydrogen adsorption on the (100) surfaces of rhodium and palladium: the influence of non-local exchange-correlation interactions. *J. Phys.: Condens. Matter*, 8:7659, 1996.

[44] B. Hammer and J. K. Nørskov. Electronic factors determining the reactivity of metal surfaces. *Surf. Sci.*, 343:211, 1995.

[45] B. Hammer. Adsorption, diffusion, and dissociation of NO, N and O on flat and stepped Ru(0001). *Surf. Sci.*, 459:323–348, 2000.

[46] P. Nordlander, S. Holloway, and J.K. Nørskov. Hydrogen adsorption on metal surfaces. *Surf. Sci.*, 136:59, 1984.

[47] J.K. Nørskov. Covalent effects in the effective-medium theory of chemical binding: hydrogen heats of solution in the $3d$ metals. *Phys. Rev. B*, 26:2875, 1982.

[48] B. Hammer and J. K. Nørskov. Why gold is the noblest of all the metals. *Nature*, 376:238, 1995.

[49] V. Pallassana, M. Neurock, L. B. Hansen, B. Hammer, and J. K. Nørskov. Theoretical trends of hydrogen chemisorption on Pd(111), Re(0001) and $\mathrm{Pd_{ML}}$/Re(0001), $\mathrm{Re_{ML}}$/Pd(111) pseudomorphic overlayers. *Phys. Rev. B*, 60: 6146, 1999.

[50] G. Blyholder. Molecular orbital view of chemisorbed carbon monoxide. *J. Phys. Chem.*, 68:2772, 1964.

[51] J. A. Rodriguez. Physical and chemical properties of bimetallic surfaces. *Surf. Sci. Rep.*, 24:223, 1996.

[52] F. Zaera. The surface chemistry of catalysis: new challenges ahead. *Surf. Sci.*, 500:947, 2002.

[53] F. Maroun, F. Ozanam, O. M. Magnussen, and R. J. Behm. The role of atomic ensembles in the reactivity of bimetallic catalysts. *Science*, 293:1811, 2002.

[54] M. Takahasi, Y. Hayashi, J. Mizuki, K. Tamura, T. Kondo, H. Naohara, and K. Uosaki. Pseudomorphic growth of Pd monolyer on Au(111) electrode surface. *Surf. Sci.*, 461:213, 2000.

[55] M. E. Quayum, S. Ye, and K. Uosaki. Mechanism for nucleation and growth of electrochemical palladium deposition on an Au(111) electrode. *J. Electroanal.*

Chem., 520:126, 2002.

[56] A. M. El-Aziz and L. A. Kibler. Influence of steps on the electrochemical oxidation of CO adlayers on Pd(111) and on pd films electrodeposited onto Au(111). *J. Electroanal. Chem.*, 534:107, 2002.

[57] B. E. Koel, A. Sellidj, and M. T. Paffett. Ultrathin films of Pd on Au(111): Evidence for surface alloy formation. *Phys. Rev. B*, 46:7846, 1992.

[58] L. A. Kibler, M. Kleinert, and D. M. Kolb. Initial stages of Pd deposition on Au(*hkl*) Part II: Pd on Au(100). *Surf. Sci.*, 461:155, 2000.

[59] T. Kondo, K. Tamura, M. Takahasi, J. Mizuki, and K. Uosaki. A novel spectro-electrochemical cell for in situ surface X-ray scattering measurements of single crystal disk electrodes. *Electrochim. Acta*, 47:3075, 2002.

[60] C. J Baddeley, R. M Ormerod, A. W. Stephenson, and R. M. Lambert. Surface structure and reactivity in the cyclization of acetylene to benzene with pd overlayers and pd/au surface alloys on au(111). *J. Phys. Chem.*, 99:5146, 1995.

[61] R. R. Adžić, J. X. Wang, O. M. Magnussen, and B. M. Ocko. Structure of electrode surfaces in the course of electrocatalytic reactions: oxidation of CO, glucose, and formaldehyde on reconstructed and unreconstructed Au(100). *Langmuir*, 12: 513, 1996.

[62] L. A. Kibler, M. Kleinert, R. Randler, and D. M. Kolb. Initial stages of Pd deposition on Au(*hkl*) Part I: Pd on Au(111). *Surf. Sci.*, 443:19, 1999.

[63] C. Liu and S. D. Bader. Absence of ferromagnetism in epitaxial films of ultrathin Pd, Rh, Rh on Pd grown on Au(100). *Phys. Rev. B*, 44:12062, 1991.

[64] A. Sellidj and B. E. Koel. Electronic and co chemisorption properties of ultrathin pd films vapor deposited on au(111). *Phys. Rev. B*, 49:8367, 1994.

[65] M. Baldauf and D. M. Kolb. Formic acid oxidation on ultrathin Pd films on Au(*hkl*) Pt(*hkl*) electrodes. *J. Phys. Chem.*, 100:11375, 1996.

[66] H. Naohara, S. Ye, and K. Uosaki. Thickness dependent electrochemical reactivity of epitaxially electrodeposited thin layers on Au(111) and Au(100) surfaces. *J. Electroanal. Chem.*, 500:435, 2001.

[67] M. Gsell, P. Jakob, and D. Menzel. Effect of substrate strain on adsorption. *Science*, 280:717, 1998.

[68] P. Jakob, M. Gsell, and D. Menzel. Interactions of adsorbates with locally strained substrate lattices. *J. Chem. Phys.*, 114:10075, 2001.

[69] M. Mavrikakis, B. Hammer, and J. K. Nørskov. Effect of strain on the reactivity of metal surfaces. *Phys. Rev. Lett.*, 81:2819, 1998.

[70] T. E. Shubina and M. T. M. Koper. Quantum-chemical calculations of CO and OH interacting with bimetallic surfaces. *Electrochim. Acta*, 47:3621, 2002.

[71] D. M. Kolb. An atomistic view of electrochemistry. *Surf. Sci.*, 500:722, 2002.

[72] Axel Groß. Reactions at surfaces studied by ab initio dynamics calculations. *Surf. Sci. Rep.*, 32:291, 1998.

[73] Axel Groß. The virtual chemistry lab for reactions at surfaces: Is it possible? Will it be helpful? *Surf. Sci.*, 500:347, 2002.

[74] J. Greeley, J. K. Nørskov, and M. Mavrikakis. Electronic structure and catalysis on metal surfaces. *Annu. Rev. Phys. Chem.*, 53:319, 2002.

[75] A. Groß. *Theoretical surface science – A microscopic perspective.* Springer, Berlin, 2002.

[76] M. Baldauf and D. M. Kolb. A hydrogen adsorption and absorption study with ultrathin Pd overlayers on Au(111) and Au(100). *Electrochim. Acta*, 38:2145, 1993.

[77] M. T. M. Koper and R. A. van Santen. Interaction of halogens with Hg, Ag and Pt surfaces: a density functional study. *Surf. Sci.*, 422:118, 1999.

[78] A. Roudgar and A. Groß. subm. to Surf. Sci.

[79] S. K. Desai, V. Pallassana, and M. Neurock. A periodic density functional theory analysis of the effect of water molecules on deprotonation of acetic acid over Pd(111). *J. Phys. Chem. B*, 105:9171, 2001.

[80] W. Dong, G. Kresse, J. Furthmüller, and J. Hafner. Chemisorption of H on Pd(111): An ab initio approach with ultrasoft pseudopotentials. *Phys. Rev. B*, 54:2157, 1996.

[81] G. Kresse and J. Furthmüller. Efficiency of ab-initio total energy calculations for metals and semiconductors using a plane-wave basis set. *Comput. Mater. Sci.*, 6:15, 1996.

[82] G. Kresse and J. Hafner. Norm-conserving and ultrasoft pseudopotentials for the first-row and transition elements. *J. Phys.: Condens. Matter*, 6:8245, 1994.

[83] F. D. Murnaghan. The compressibility of media under extreme pressure. *Proc. Nat. Acad. Sci. USA*, 30:244–247, 1944.

[84] Francis Birch. Finite strain isotherm and velocities for single-crystal and polycrystalline NaCl at high pressure and 300 K. *J. Geophys. Res.*, 83:1257, 1978.

[85] Neil W. Ashcroft and N. David Mermin. *Solid State Physics.* Saunders College, 1976.

[86] J. K. Nørskov, T. Bligaard, A. Logadottir, S. Bahn, L. B. Hansen, M. Bollinger, H. Bengaard, B. Hammer, Z. Sljivancanin, M. Mavrikakis, Y. Xu, S. Dahl, and C. J. H. Jacobsen. Universality in heterogeneous catalysis. *J. Catal.*, 209:275, 2002.

[87] A. Ruban, B. Hammer, P. Stoltze, H. L. Skriver, and J. K. Nørskov. Surface electronic structure and reactivity of transition and noble metals. *J. Mol. Catal. A*, 115:421, 1997.

[88] B. Hammer, O. H. Nielsen, and J. K. Nørskov. Structure sensitivity in adsorption: CO interaction with stepped and reconstructed pt surfaces. *Catal. Lett.*, 46:31, 1997.

[89] B. Hammer. Reactivity of a stepped surface – NO dissociation on Pd(211). *Faraday Discuss.*, 110:323, 1998.

[90] Pia K. Schmidt, Klaus Christmann, Georg Kresse, Jürgen Hafner, Markus Lischka, and Axel Groß. Coexistence of atomic and molecular chemisorption states: H_2/Pd(210). *Phys. Rev. Lett.*, 87:096103, 2001.

[91] M. Lischka and A. Groß. Hydrogen adsorption on an open metal surface: H_2/Pd(210). *Phys. Rev. B*, 65:075420, 2002.

[92] K. D. Rendulic, G. Anger, and A. Winkler. Wide range nozzle beam adsorption data for the systems H_2/nickel and H_2/Pd(100). *Surf. Sci.*, 208:404, 1989.

[93] M. Gostein and G. O. Sitz. Rotational state-resolved sticking coefficients for H_2 on Pd(111): testing dynamical steering in dissociative adsorption. *J. Chem. Phys.*, 106:7378, 1997.

[94] Axel Groß, Steffen Wilke, and Matthias Scheffler. Six-dimensional quantum dynamics of adsorption and desorption of H_2 at Pd(100): steering and steric effects. *Phys. Rev. Lett.*, 75:2718, 1995.

[95] Axel Groß and Matthias Scheffler. Ab initio quantum and molecular dynamics of the dissociative adsorption of hydrogen on Pd(100). *Phys. Rev. B*, 57:2493, 1998.

[96] Axel Groß and Matthias Scheffler. Dynamics of hydrogen dissociation at the sulfur-covered Pd(100) surface. *Phys. Rev. B*, 61:8425, 2000.

[97] S. Wilke, D. Hennig, and R. Löber. Ab initio calculations of hydrogen adsorption on (100) surfaces of palladium and rhodium. *Phys. Rev. B*, 50:2548, 1994.

[98] S. Wilke and M. Scheffler. Poisoning of Pd(100) for the dissociation of H_2: a theoretical study of co-adsorption of hydrogen and sulfur. *Surf. Sci.*, 329:L605, 1995.

[99] W. Dong, V. Ledentu, Ph. Sautet, A. Eichler, and J. Hafner. Hydrogen adsorption on palladium: a comparative theoretical study of different surfaces. *Surf. Sci.*, 411:123, 1998.

[100] Andreas Eichler and Jürgen Hafner. Adsorption of CO on Pd(100): Steering into less favored adsorption sites. *Phys. Rev. B*, 57:10110, 1998.

[101] B. Hammer. The NO+CO reaction catalyzed by flat, stepped, and edged Pd surfaces. *J. Catal.*, 199:171, 2001.

[102] B. Hammer, Y. Morikawa, and J. K. Nørskov. CO chemisorption at metal surfaces and overlayers. *Phys. Rev. Lett.*, 76:2141, 1996.

[103] S. Sakong and A. Groß. Dissociative adsorption of hydrogen on strained cu surfaces. *Surf. Sci.*, 525:107, 2003.

[104] A. Schlapka, U. Käsberger, D. Menzel, and P. Jakob. Vibrational spectroscopy of CO used as a local probe to study the surface morphology of Pt on Ru(001) in the submonolayer regime. *Surf. Sci.*, 502:129, 2002.

[105] A. Schlapka, M. Lischka, A. Groß, U. Käsberger, and P. Jakob. Surface strain versus substrate interaction in heteroepitaxial metal layers: Pt on Ru(001). *Phys. Rev. Lett.*, 91:016101, 2003.

[106] S. Wilke, D. Hennig, R. Löber, M. Methfessel, and M. Scheffler. Ab initio study of hydrogen adsorption on Pd(100). *Surf. Sci.*, 307:76, 1994.

[107] A. B. Aaen, E. Lægsgaard, A. V. Ruban, and I. Stensgaard. Submonolayer growth of Pd on Cu(111) studied by tunneling microscopy. *Surf. Sci.*, 408:43, 1998.

[108] A. de Siervo, E. A. Soares, R. Landers, T. A. Fazan, J. Morais, and G. G. Kleiman. Pd on Cu(111) studied by photoelectron diffraction. *Surf. Sci.*, 504: 215, 2002.

[109] N. Lopez and J. K. Nørskov. Synergetic effects in CO adsorption on Cu-Pd(111) alloys. *Surf. Sci.*, 477:59, 2001.

[110] G. Liu, T. P. St. Clair, and D. W. Goodman. An XPS study of the interaction of ultrathin Cu films with Pd(111). *J. Phys. Chem. B*, 103:8578, 1999.

[111] A. Cuesta, L. A. Kibler, and D. M. Kolb. A method to prepare single crystal electrodes of reactive metals: application to Pd(hkl). *J. Electroanal. Chem.*, 466: 165, 1999.

[112] J. Okada, J. Inukai, and K. Itaya. Underpotential and bulk deposition of copper on Pd(111) in sulfuric acid solution studied by in situ scanning tunneling microscopy. *Phys. Chem. Chem. Phys.*, 3:3297, 2001.

[113] K. Wildberger, V. S. Stepanyuk, P. Lang, R. Zeller, and Dederichs P. H. Magnetic nanostructures: 4 d clusters on Ag(001). *Phys. Rev. Lett.*, 75:509, 1995.

[114] A. Sanchez, S. Abbet, U. Heiz, W.-D. Schneider, H. Häkkinen, R. N. Barnett, and Uzi Landman. When gold is not noble: nanoscale gold catalysts. *J. Phys. Chem. A*, 103:9573, 1999.

[115] M. Valden, X. Lai, and D. W. Goodman. Onset of catalytic activity of gold clusters on titania with the appearance of nonmetallic properties. *Science*, 281: 1647, 1998.

[116] K. Kinoshita. Particle size sffects for oxygen reduction on highly dispersed platinum in acid electrolytes. *J. Electrochem Soc.*, 137:845, 1990.

[117] Andolfatto F. Durand R. Kabbabi A., Gloaguen F. Particle size effect for oxygen reduction and methanol oxidation on pt/c inside a proton exchange membrane. *J. Electroanal Chem.*, 373:251, 1994.

[118] Tanaka T. Miyake M. Taranishi T., Hosoe M. Size control of monodispersed pt nanoparticles and their 2d organization by electrophoretic deposition. *J. Phys. Chem. B*, 103:3818, 1999.

[119] J. A. Meier, K. A. Friedrich, and U. Stimming. Novel method for the investigation of single particle reactivity. *Faraday Discuss.*, 121:365, 2002.

[120] D. M. Kolb, R. Ullmann, and T. Will. Nanofabrication of small copper clusters on gold(111) electrodes by a scanning tunneling microscope. *Science*, 275:1097, 1997.

[121] D. M. Kolb, G. E. Engelmann, and J. C. Ziegler. On the unusual electrochemical stability of nanofabricated copper clusters. *Angew. Chemie, Int. Ed.*, 39:1123, 2000.

[122] Kleine H. Meier J. Stimming U. Mariscal M. Schmickler W. Del Popolo M., Leiva E. Generation of palladium clusters on au(111) electrodes: Experiments and simulations.

[123] Schmickler W. Del Popolo M., Leiva E. On the stability of electrochemically generated nanoclusters - a computer simulation. *Angew. Chem. Int.*, 40:4674,

2001.

[124] M. Eikerling, J. Meier, and U. Stimming. Hydrogen evoluation at a single supported nanoparticle: a kinetic model. *Z. Phys. Chem.*, 217:395, 2003.

[125] D. R. Jennison, P. A. Schultz, and M. P. Sears. *Ab initio* calculations of Ru, Pd, and Ag cluster structure with 55, 135, and 140 atoms. *J. Chem. Phys.*, 106:1856, 1997.

[126] Andrew Zangwill. *Physics at Surfaces.* Cambridge University Press, Cambridge, 1988.

[127] A. Alavi, P. Hu, T. Deutsch, P. L. Silvestrelli, and J. Hutter. CO oxidation on Pt(111): An ab initio density functional theory study. *Phys. Rev. Lett.*, 80:3650, 1998.

[128] D. R. Hamann. H_2O hydrogen bonding in density-functional theory. *Phys. Rev. B*, 55:R10157, 1997.

[129] P. A. Thiel and T. E. Madey. The interaction of water with solid surfaces: Fundamental aspects. *Surf. Sci. Rep.*, 7:211, 1987.

[130] M. A. Henderson. The interaction of water with solid surfaces: fundamental aspects revisited. *Surf. Sci. Rep.*, 46:1, 2002.

[131] G. Comsa M. Morgenstern, T. Michely. Anisotropy in the adsorption of h_2o at low coordination sites on pt(111). *Phys. Rev. Lett.*, 77:703, 1996.

[132] et al A. Glebov. Orientational ordering of two-dimensional ice on pt(111). *J. Chem. Phys.*, 106:9382, 1997.

[133] S. Meng, L. F. Xu, E. G. Wang, and S. W. Gao. Vibrational recognition of hydrogen-bonded water networks on a metal surface. *Phys. Rev. Lett.*, 89:176104, 2002.

[134] D. Menzel G. Held. The structure of the $p(\sqrt{3}\times\sqrt{3})r30^\circ$ bilayer of d_2o on ru(001). *Surf. Sci.*, 316:92, 1994.

[135] D. Menzel G. Held. Structural isotope effect in water bilayers adsorbed on ru(001). *Phys. Rev. Lett.*, 74:4221, 1994.

[136] P. J. Feibelman. Partial dissociation of water on Ru(0001). *Science*, 295:99, 2002.

[137] D. Menzel. Water on a metal surface. *Science*, 295:58, 2002.

[138] J. L. Gland G. B. Fisher. The interaction of water with the pt(111) surface. *Surf. Sci.*, 94:446, 1980.

[139] M. Morgenstern et al. *Z. Phys. Chem.*, 198:43, 1997.

[140] K. Jacobi et al. From monomers to ice - new vibrational characteristics of h_2o adsorbed on pt(111). *Surf. Sci.*, 472:9, 2001.

[141] D. Thompsett G. Hoogers. *Catttech*, 6:106, 2000.

[142] T. Fujino M. Watanabe, H. Igarashi. *Electrochemistry*, 67:1194, 1999.

[143] U. Stimming F. Trila H. F. Oetjen, V. M. Schmidt. *J. Electrochem Soc*, 143: 3838, 1996.

[144] E. Christoffersen, P. Liu, A. Ruban, H. L. Skriver, and J. K. Nørskov. Anode materials for low-temperature fuel cells: A density functional theory study. *J.*

Catal., 199:123, 2001.

[145] T. E. Madey D. L. Doering. The adsorption of water on clean and oxygen-dosed ru(011). *Surf. Sci.*, 123:305, 1982.

[146] P. J. Feibelman. Comment on "vibrational recognition of hydrogen-bonded water networks on a metal surface". *Phys. Rev. Lett.*, 91:059601, 2003.

[147] S. Meng, L. F. Xu, E. G. Wang, and S. W. Gao. Meng *et al.* reply:. *Phys. Rev. Lett.*, 91:059602, 2003.

List of Publications

1. Ata Roudgar and Axel Groß. Local reactivity of metal overlayers: Density functional theory calculations of Pd on Au. *Phys. Rev. B*, 67:033409, 2003.
2. Ata Roudgar and Axel Groß. Local reactivity of thin Pd overlayers on Au single crystals. *J. Electroanal. Chem.*, 548:121, 2003.
3. Ata Roudgar and Axel Groß. Hydrogen adsorption energies on bimetallic overlayer systems at the solid-vacuum and the solid-liquid interface. To appear in *Surf. Sci.*
4. Ata Roudgar and Axel Groß. Local reactivity of supported metal clusters: Pd_n on Au(111). To appear in *Surf. Sci. Lett.*